

**ASSESSING EXTRATROPICAL INFLUENCE ON TROPICAL CLIMATOLOGY
AND VARIABILITY WITH REGIONAL COUPLED DATA ASSIMILATION**

by

Feiyu Lu

A dissertation submitted in partial fulfillment of
the requirements for the degree of

Doctor of Philosophy

(Atmospheric and Oceanic Sciences)

at the

UNIVERSITY OF WISCONSIN–MADISON

2017

Date of final oral examination: 05/03/2017

The dissertation is approved by the following members of the Final Oral Committee:

Zhengyu Liu, Professor, Atmospheric and Oceanic Sciences
Dan Vimont, Professor, Atmospheric and Oceanic Sciences
Greg Tripoli, Professor, Atmospheric and Oceanic Sciences
Jon Martin, Professor, Atmospheric and Oceanic Sciences
Sam Stechmann, Associate Professor, Mathematics

©Copyright by Feiyu Lu 2017

All Rights Reserved

For my wife.

With no one else do I want to bring Max to the world more.

Acknowledgements

I want to thank my parents for all their support, although I have been moving farther and farther away from home over the years. They have traveled a great deal to visit me throughout my school years. I want to thank my wife. I would be lying if I say that I imagined having a lifelong relationship with you when we first knew each other at the age of 13, but I would also be lying if I say that I prefer to spend my life with anyone else now. I want to thank our dog for all the laughter and cuddling he brought on the dull days.

I want to thank my advisor, Zhengyu Liu, who gave me a chance to pursue my PhD here at UW-Madison and provided consistent guidance as I ventured through my pursuit. I want to thank all my other committee members—Dan, Greg, Sam, Jon and Peter—for taking the time to help me achieve my goal, especially Dan, who helped tremendously when my research veered into his field. I want to thank all the faculty and staff in AOS for their support for academic career.

I also want to thank all my colleagues and friends in the beautiful city of Madison, Wisconsin. Thank you for all the academic discussion, chit-chats, get-togethers, and basketball games.

Last but potentially the most long lasting, I want to thank my newborn son, who came to the world as I was finishing my PhD. Thank you for giving me more purpose in life.

Abstract

ASSESSING EXTRATROPICAL INFLUENCE ON TROPICAL CLIMATOLOGY AND VARIABILITY WITH REGIONAL COUPLED DATA ASSIMILATION

Feiyu Lu

Under the supervision of Professor Zhengyu Liu

At the University of Wisconsin-Madison

Tropical variability (e.g. El Niño-Southern Oscillation or ENSO) and climatology (e.g. asymmetric Inter-Tropical Convergence Zone or ITCZ) were initially thought to be determined mostly by local forcing and ocean-atmosphere interaction in the tropics. Since late 20th century, numerous studies have showed that extratropical forcing could affect, or even largely determine some aspects of the tropical climate. Due to the coupled nature of the climate system, the challenge of determining and further quantifying the causality of extratropical forcing on the tropical climate remains to be further explored. This dissertation studies the extratropical influence on the tropical climate, including both variability and climatology, using the Regional Coupled Data Assimilation (RCDA) method in a coupled general circulation model (CGCM). The RCDA method limits the data assimilation to the desired model components (e.g. atmosphere) and regions (e.g. the extratropics) and studies the ensemble-mean model response (e.g. tropical response to “observed” extratropical atmospheric variability).

First, perfect-model RCDA experiments demonstrate significant control of extratropical atmospheric forcing on ENSO variability in the CGCM. When atmospheric “observations” are assimilated only poleward of 20° in both hemispheres, most ENSO events in the “observation” are reproduced. Experiments with single-hemisphere

assimilation show that the forced ENSO variability is contributed roughly equally and independently by the Southern and Northern Hemisphere extratropical atmosphere. Robust precursors are found in both the extratropical atmosphere over southeastern Pacific and equatorial Pacific thermocline, consistent with previous studies. However, neither precursor alone is sufficient to trigger ENSO onset, therefore neither alone could serve as a reliable predictor.

Then, RCDA experiments with real world reanalysis data show extratropical impact on both tropical climatology and variability in the CGCM. The model's double-ITCZ bias is improved systematically when SST, air temperature and wind are corrected toward real world data from the extratropics into the tropics progressively. Coupled dynamics, as well as atmospheric and oceanic processes, play important roles in this extratropical-to-tropical teleconnection. Certain historical ENSO events are also reproduced by assimilating extratropical atmospheric observations. Analysis of the real world RCDA experiments confirms the effects of the precursors found in the perfect-model experiments, while also points to the impact of model bias on ENSO variability.

Table of Contents

Acknowledgements	ii
Abstract	iii
Table of Contents	v
List of Tables.....	vii
List of Figures	viii
1. Introduction	1
1.1. Extratropical Influence on tropical climatology	1
1.2. Extratropical Impact on El Niño-Southern Oscillation (ENSO)	4
1.3. Coupled Data Assimilation (CDA)	6
2. Model and Methods	8
2.1. Fast Ocean Atmosphere Model (FOAM).....	8
2.2. CDA System in FOAM	8
2.3. Strongly Coupled Data Assimilation (SCDA).....	9
2.4. Regional Coupled Data Assimilation (RCDA)	16
3. Extratropical Influence on Tropical Climatology	19
3.1. Methods	19
3.1.1. <i>Datasets</i>	19
3.1.2. <i>Experiment Design</i>	19
3.1.3. <i>Assimilating Reanalysis Data</i>	20
3.2. Tropical Asymmetry Bias of Precipitation	21
3.3. Equatorial Deficiency Bias of Precipitation	34
3.4. Energetic Analysis	35
3.5. Summary and Discussion of Chapter 3.....	37
4. Extratropical Influence on Tropical Variability: Perfect-model Study	40

4.1.	Model and Methods.....	40
4.1.1.	<i>ENSO in FOAM</i>	40
4.1.2.	<i>Experiment Design</i>	43
4.1.3.	<i>Performance of RCDA</i>	46
4.2.	Overview of Results	48
4.2.1.	<i>General Assessment</i>	48
4.2.2.	<i>Extratropical Control on ENSO</i>	52
4.3.	ENSO Precursors	55
4.3.1.	<i>ENSO Composites and Potential Precursors</i>	55
4.3.2.	<i>Equatorial Oceanic Precursor</i>	61
4.3.3.	<i>Extratropical Atmospheric Precursor</i>	66
4.3.4.	<i>The Precursors Combined</i>	70
4.4.	Summary and Discussion of Chapter 4.....	74
5.	Extratropical Influence on Tropical Variability: Applications with Real-world Observations.....	78
5.1.	Datasets and Experiment Design	78
5.2.	Overview of Results	79
5.2.1.	<i>ENSO Variability</i>	79
5.2.2.	<i>Annual Cycle and ENSO Phase-locking</i>	84
5.2.3.	<i>Equatorial Pacific Heat Content</i>	89
5.3.	Case Studies	91
5.3.1.	<i>1972-73 El Niño (Successful)</i>	91
5.3.2.	<i>1997-98 El Niño (Unsuccessful)</i>	101
5.3.3.	<i>Comparison of 1972-73 El Niño and 1997-98 El Niño</i>	103
5.4.	Summary and Discussion of Chapter 5.....	106
6.	Summary.....	108
6.1.	Summary.....	108
6.2.	Possibilities for Future Research.....	110
	References	112

List of Tables

Table 3.1 Table of all RCDA experiments in Chapter 3. (from [Lu et al., 2017a])	21
Table 3.2 Correlation of anomalous monthly SST, surface air temperature and surface zonal wind between the model and the observation for <i>CTRL</i> , <i>CDA_ALL</i> , <i>CDA_28</i> , <i>ADA_28</i> and <i>ODA_28</i> averaged over 28°S-28°N and poleward of 28°S/28°N. (from [Lu et al., 2017a])	32
Table 4.1 A summary of all experiments in [Lu et al., 2017b].....	43
Table 5.1 Table of all RCDA experiments in Chapter 5.....	79
Table 5.2 List of the short experiments used in Chapter 5. The modified aspects of the experiments that are different from the original RCDA experiments are bold. ...	97

List of Figures

- Figure 2.1 Zonal-mean RMSE (Root Mean Square Error) of monthly SST from the SimCC experiment and the LACC experiments with different averaging lengths, normalized by the WCDA experiment. (from [Lu *et al.*, 2015b]) 13
- Figure 2.2 Spatial distribution of the RMSE of monthly SST from a) the SimCC experiment (normalized by the WCDA), b) the “Ave7” experiment (normalized by the WCDA), and c) the “Ave7” experiment (normalized by the SimCC). (from [Lu *et al.*, 2015b])..... 16
- Figure 3.1 Zonal-mean climatological precipitation and surface air temperature of selected CDA experiments, along with observation and CTRL. (a) Total precipitation. (b) Surface air temperature bias from observation. Filled circles indicate the data assimilation boundaries when applicable. (from [Lu *et al.*, 2017a]) 22
- Figure 3.2 Climatological SST (shadings), precipitation (contours with 2 mm/day interval) and surface wind (arrows). (a) Observation. (b) CTRL. (c) Difference of CTRL minus observation. (from [Lu *et al.*, 2017a])..... 23
- Figure 3.3 Differences in climatological SST (shadings), precipitation (contours with 2 mm/day interval) and surface wind (arrows). (a) Between CDA_ALL and observation. (b) Between CDA_ALL and CTRL. (c) Between CDA_24 and CTRL. The horizontal dotted lines indicate the data assimilation boundaries of CDA_24. (from [Lu *et al.*, 2017a]) 24

- Figure 3.4 A summary of annual-mean climatological indices from observation (pentagon), FOAM control (asterisk), *CDA* (blue circle), *ADA* (red square), and *ODA* (green diamond) experiments. (a) Tropical precipitation asymmetry index PA. (b) Tropical surface temperature asymmetry TA. (c) Equatorial precipitation index PEq. (from [Lu et al., 2017a])..... 25
- Figure 3.5 Correlation of monthly SST anomaly between *CDA_24* and observation. The dotted points indicate that significance level of the correlation is over 99% based on a Student-t test. The horizontal dotted lines indicate the data assimilation boundaries of *CDA_24*. (from [Lu et al., 2017a]) 27
- Figure 3.6 Zonal-mean climatological 0-400m average temperature change from CTRL for *CDA_28*, *CDA_42*, *ADA_28*, *ADA_42*, *ODA_28* and *ODA_42* experiments. Filled circles indicate the data assimilation boundaries where applicable. (from [Lu et al., 2017a]) 29
- Figure 3.7 Changes in meridional energy transport by the (a) atmosphere and (b) ocean from CTRL to *ADA_ALL*, *ADA_15*, *ADA_24*, *ADA_33* and *ADA_42* experiments. Filled circles indicate the data assimilation boundaries where applicable..... 29
- Figure 3.8 Same as Figure 3.5, but for *ADA_24*..... 31
- Figure 3.9 Same as Figure 3.5, but for *ODA_24*..... 31
- Figure 3.10 A summary of seasonal-mean climatological indices from observation (pentagon), FOAM control (asterisk), *CDA* (other markers) experiments. (a) Tropical precipitation asymmetry index PA. (b) Tropical surface temperature asymmetry TA. (c) Equatorial precipitation index PEq. (from [Lu et al., 2017a]) 33

Figure 3.11 Scatterplots between indices for observation (pentagon), *CTRL* (asterisk), *CDA* (blue), *ADA* (red) and *ODA* experiments (green). (a) Tropical precipitation asymmetry PA against tropical surface temperature asymmetry TA. (b) PA against cross-equatorial atmospheric energy transport AETEq. (c) PA against equatorial precipitation index PEq. (d) PEq against equatorial net energy input NEIEq. (from [Lu et al., 2017a]) 36

Figure 4.1 Annual-mean tropical SST climatology from a 500-year FOAM control simulation. (b) The power spectrum of the Nino3.4 index from the same 500-year FOAM control simulation. (from [Lu et al., 2017b]) 41

Figure 4.2 Regression of equatorial upper ocean temperature (3°S-3°N meridional average) on normalized Nino3.4 index from the 500-year FOAM control simulation. The relative times between ocean temperature and Nino3.4 index are -12, -9, -6, -3, 0, 3, 6, 9 and 12 months (positive when Nino3.4 index leads) from left to right and top to bottom. (from [Lu et al., 2017b]) 42

Figure 4.3 Pacific (120°E-80°W) zonal-mean RMSE (normalized by *CTRL*) of ensemble-mean atmospheric temperature (shadings), zonal wind (dashed lines) and SST (lower panel) for (a) *ada_all*, (b) *ada_20*, (c) *ada_north20*, and (d) *ada_south20*. The thick dash-dot lines indicate the boundaries of data assimilation where necessary. (from [Lu et al., 2017b]) 47

Figure 4.4 The time series of Nino3.4 index from (a) *CTRL*, (b) *ada_all*, (c) *ada_20*, (d) *ada_north20*, (e) *ada_north20A*, (f) *ada_south20*, and (g) *ada_south20A*. Red lines indicate the “truth” (same for all panels), black lines the ensemble mean, and grey lines all 16 ensemble members. (from [Lu et al., 2017b]) 48

- Figure 4.5 Scatter plots with linear regression slope coefficient and adjusted R^2 for the Nino3.4 indices of (a) *ada_north20* (blue) and *ada_south20* (red) vs. truth, (b) *ada_south20* vs. *ada_north20*. (from [Lu et al., 2017b]) 52
- Figure 4.6 Standard deviations of the Nino3.4 index by calendar month from the *truth*, *ada_20*, *ada_north20* and *ada_south20*. (from [Lu et al., 2017b]) 54
- Figure 4.7 For *ada_south20*: (a) Composite of Nino3.4 index of 29 ENSO events exceeding 0.5°C . La Nina events are included with reversed sign. Dashed lines indicate CTRL_SD, the standard deviations of the ensemble-mean anomalies from CTRL. (b) Composite of 5°S - 5°N averaged Pacific SST based on the Nino3.4 peaks (shadings) and its ratio to the corresponding CTRL_SD (contours). (c) Same as Figure 4.7a but for WS_SE. (d) Same as Figure 4.7a but for HC_EW. (from [Lu et al., 2017b])..... 56
- Figure 4.8 Composites of anomalous SST (shadings, K), LHF (contours, 4 W/m^2 intervals and zero line omitted) and wind (arrows) for the 5 months prior to the peak of the Nino3.4 composite in *ada_south20*. Blue (red) contours indicate more (less) upward LHF. Black dotted lines indicate the boundary of data assimilation. SST and wind anomalies are only shown where the composite exceed CTRL_SD. (from [Lu et al., 2017b]) 57
- Figure 4.9 Composite of anomalous 3°S - 3°N averaged Pacific upper ocean temperature (a) 8 months and (b) 4 months prior to the peak of the Nino3.4 composite in *ada_south20*. The contours indicate the ratios of the composite anomalies to CTRL_SD. (from [Lu et al., 2017b]) 59

Figure 4.10 (a) Composite of HC_EW series for the 24 strongest HC_EW events. Negative anomalies are included with reversed sign. The HC_EW events that are followed by ENSO events of the same sign within 16 months are marked red, and the rest are marked blue. The blue (red) solid line is the average of all blue (red) dashed lines. (b) Composite of Nino3.4 index in *ada_south20* for the same events as (a); (c) Same as (b), but of WS_SE. (from [Lu et al., 2017b]) 62

Figure 4.11 Same as Figure 4.9, but for the “red” (left column, a-c) and “blue” (right column, d-f) HC_EW events from Figure 4.10, respectively. The composites are at the same time as the peak of HC_EW composite (a, d), 3 months after (b, e), and 6 months after (c, f). (from [Lu et al., 2017b]) 64

Figure 4.12 Same as Figure 4.8, but for the “red” (left column, a-c) and “blue” (right column, d-f) HC_EW events from Figure 4.10, respectively. The composites are at 3 months (a, d), 6 months (b, e) and 9 months (c, f) after the peak of HC_EW composite. (from [Lu et al., 2017b]) 65

Figure 4.13 (a) Composite of WS_SE anomalies for the 24 strongest WS_SE events. Positive anomalies are included with reversed sign. The WS_SE events that are followed by ENSO events of opposite sign within 6 months are marked red, and the rest are marked blue. The blue (red) solid line is the average of all blue (red) dashed lines. (b) Same as Figure 4.8, but for all the WS_SE events at the peak. (c) Composite of Nino3.4 index in *ada_south20* for the same events as (a); (d) Same as (c), but of HC_EW. (from [Lu et al., 2017b]) 67

Figure 4.14 Same as Figure 4.13b, but for (a) “red” and (b) “blue” events, respectively. (from [Lu et al., 2017b]) 69

Figure 4.15 Same as Figure 4.9, but for the “red” (left column, a-c) and “blue” (right column, d-f) WS_SE events from Figure 4.13a, respectively. The composites are 8 months (a, d), 4 months (b, e) prior to, and at the same month (c, f) as the peak of the WS_SE composite. (from [Lu et al., 2017b]) 70

Figure 4.16 Scatterplot of all 29 ENSO events in *ada_south20* based on the minimum opposite-sign value of 3-5 months leading WS_SE (y-direction) and maximum same-sign value of 6-18 months leading HC_EW (x-direction). The color and size of the markers together indicate the peak Nino3.4 values. The dashed lines indicate the corresponding CTRL_SD. (from [Lu et al., 2017b])71

Figure 4.17 (a) Scatterplot of the April-July averaged WS_SE with August-October averaged Nino3.4 index of the same year, plotted for the years when the averaged WS_SE has the opposite sign as the June (previous year)-May (same year) averaged HC_EW. (b) Same as (a), but for the years when the averaged WS_SE has the same sign as the averaged HC_EW. (c) Scatterplot of the June (previous year)-May (same year) averaged HC_EW with August-October averaged Nino3.4 index, plotted for the years when the April-July averaged WS_SE has the opposite sign as the averaged HC_EW. (d) Same as (c), but for the years when the averaged WS_SE has the same sign as the averaged HC_EW. (from [Lu et al., 2017b]).... 72

Figure 5.1 The time series of Nino3.4 index from (a) *ctrl*, (b) *cda_all*, (c) *ada_all* and (d) *oda_all*. Grey lines indicate the observed Nino3.4 index (same for all panels), red lines the ensemble mean, and pink lines all 16 ensemble members.....80

Figure 5.2 Same as Figure 5.1, but for (a) *ada_10*, (b) *ada_20*, (c) *ada_28* and (d) *ada_37*.
.....82

- Figure 5.3 The power spectrum of the Nino3.4 index from observation, *CTRL*, *ada_all*, *ada_20* and *ada_28*. 83
- Figure 5.4 A summary of ENSO variability statistics from *CTRL* (asterisk), *CDA* (blue diamond), *ADA* (red circle), and *ODA* (green square) experiments. (a) Correlation of Nino3.4 index with the observation. (b) RMSE of Nino3.4 index compared to observation. 84
- Figure 5.5 Equatorial (5°S-5°N average) Pacific SST and wind annual cycle for (a) *CTRL*, (b) observation, (c) *ada_all*, (d) *ada_10*, (e) *ada_20*, (f) *ada_28*, (g) *ada_N20* and (h) *ada_S20*. 86
- Figure 5.6 Eastern (80°W-120°W average) Pacific SST and wind annual cycle for (a) *CTRL*, (b) observation, (c) *ada_all*, (d) *ada_10*, (e) *ada_20*, (f) *ada_28*, (g) *ada_N20* and (h) *ada_S20*. 87
- Figure 5.7 Standard deviations of Nino3.4 index by calendar month in observation, *CTRL*, *ada_all*, *ada_10*, *ada_20* and *ada_28*. 88
- Figure 5.8 Equatorial Pacific (5°S-5°N, 120°E-80°W) zonal-mean 0-300m average temperature (*t300*) time series of (a) *ctrl*, (b) *cda_all*, (c) *ada_all* and (d) *oda_all*, red in each panel. The green, grey and blue lines are *t300* of *cda_all*, SODA and GODAS respectively. Linear trends are removed from all *t300* time series. 90
- Figure 5.9 Same as Figure 5.8, but for (a) *ada_10*, (b) *ada_20*, (c) *ada_28* and (d) *ada_37*. 91
- Figure 5.10 For *ada_all* in the period 1971-1973: (a) Nino3.4 index of ensemble mean (red) and all ensemble members (pink) of *ada_all*, along with observation (grey) and

ctrl (black); (b) W_SEPac (blue), W_NEPac (Purple) and $t300$ (orange) of ada_all (solid) and observation (dashed); (c) evolution of equatorial ($5^{\circ}S-5^{\circ}N$) Pacific SST in ada_all ; (d) evolution of equatorial ($5^{\circ}S-5^{\circ}N$) Pacific 0-300m average ocean temperature.	92
Figure 5.11 Same as Figure 5.10, but for ada_20 in the period 1971-1973.	94
Figure 5.12 Same as Figure 5.10, but for ada_28 in the period 1971-1973.	95
Figure 5.13 Composites of anomalous monthly SST (shadings) and wind (arrows) from March 1972 to November 1972 in ada_20 . Black dotted lines indicate the boundary of data assimilation. SST and wind anomalies are only shown where the composite exceed twice the standard deviation of $ctrl$ (CTRL_SD as described in Section 4.2.1).	96
Figure 5.14 Same as Figure 5.11a, with the addition of the Nino3.4 index from short experiment No.1 (blue). The grey, black, red and pink lines are observation, $ctrl$, original ensemble mean and ensemble members, respectively.	97
Figure 5.15 Same as Figure 5.14, but for W_NEPac , W_SEPac and $t300$ instead of Nino3.4 index, and without individual ensemble members.	98
Figure 5.16 Observed daily (asterisk with dotted line), weekly (solid line) and monthly (dashed line) W_SEPac anomalies in 1972.	99
Figure 5.17 Same as Figure 5.11a, with the addition of the Nino3.4 index from short experiment No.2 (blue).	100
Figure 5.18 Same as Figure 5.11a, with the addition of the Nino3.4 index from short experiment No.3 (blue).	100

Figure 5.19 Same as Figure 5.10, but for <i>ada_all</i> in the period 1996-1998.	101
Figure 5.20 Same as Figure 5.10, but for <i>ada_20</i> in the period 1996-1998.	102
Figure 5.21 Same as Figure 5.10, but for <i>ada_28</i> in the period 1996-1998.	103
Figure 5.22 Same as Figure 5.11a, with the addition of the Nino3.4 index from short experiment No.4 (blue).	104
Figure 5.23 Same as Figure 5.20a, with the addition of the Nino3.4 index from short experiment No.5 (blue).	104
Figure 5.24 Same as Figure 5.12a, with the addition of the Nino3.4 index from short experiment No.6 (blue).	105
Figure 5.25 Same as Figure 5.21a, with the addition of the Nino3.4 index from short experiment No.7 (blue).	105

Chapter 1

1. Introduction

The tropical climate serves as the driver of the global climate by providing energy and moisture to the extratropics and exerting some of the most dominant climate variability from subseasonal (e.g. the Madden-Julian Oscillation or tropical cyclones) to interannual timescales (e.g. ENSO). The climatology and variability of the tropical climate have been the subject of numerous research fields, including climate dynamics, tropical meteorology, climate modeling, etc. The mechanisms that determine the tropical climatology and variability have long been thought to be dominated by tropical processes. However, in the past 20 years or so, the extratropical influence on the tropics has drawn a lot of attention from researchers, as the evidence of extratropical control on tropical climatology [*Liu and Yang, 2003; Chiang and Bitz, 2005; Kang et al., 2008*] and variability [*Vimont et al., 2001, 2003a, 2003b*] surfaced from observational and modeling studies.

1.1. Extratropical Influence on tropical climatology

The asymmetric features of the tropical climate, specifically those in the eastern Pacific Ocean, has been investigated for decades [*Mitchell and Wallace, 1992; Philander et al., 1996; Xie, 2004*]. The displacement of the Inter-Tropical Convergence Zone (ITCZ), despite the hemispherical symmetry of solar radiation, is one of the primary asymmetric features. Numerous theories have been formulated to explain the ITCZ asymmetry. The strong asymmetry in land mass distribution and continental topography could provide the necessary disturbances to break the asymmetry and displace the maximum SST and ITCZ to the north of the equator [*Philander et al., 1996; Xie, 2004; Takahashi and*

Battisti, 2007; Maroon et al., 2015], while several ocean-atmosphere feedback mechanisms, such as the Wind-Evaporation-SST (WES) feedback, stratus cloud-SST feedback and upwelling-SST feedback [*Klein and Hartmann, 1993; Xie and Philander, 1994; Philander et al., 1996*], could amplify such disturbances and form the current asymmetric tropical climatology. These theories mostly focused on local processes and mechanisms inside the tropics, and they are often interconnected through the strong SST (sea surface temperature) control over precipitation, especially in the eastern Pacific and the Atlantic [*Mitchell and Wallace, 1992; Waliser and Graham, 1993*].

Recently, an energetic perspective on the ITCZ asymmetry has emerged [*Broccoli et al., 2006; Kang et al., 2008, 2009; Frierson and Hwang, 2012; Donohoe et al., 2013; Frierson et al., 2013; Schneider et al., 2014*]. This energetic perspective considers the global atmosphere energy budget instead of the detailed dynamic processes. It has been widely and convincingly shown that the ITCZ tends to shift toward the warmer hemisphere in climate models. For example, when the northern high-latitude is cooled in general circulation models (GCMs), the northward cross-equator atmospheric energy transport (AET) strengthens and the ITCZ shifts southward [*Kang et al., 2008; Cvijanovic and Chiang, 2013; Donohoe et al., 2013*]. The change in northern high-latitude energy budget could increase the meridional temperature gradient in the Northern Hemisphere and transport more energy from the north Tropics poleward via intensified eddy energy flux in the extratropics [*Chiang and Bitz, 2005; Kang et al., 2008, 2009; Frierson et al., 2013*]. Given the strong correlation between cross-equator AET and the ITCZ position, researchers have argued that any perturbations to the interhemispheric atmospheric energy budget could equally affect the cross-equator AET,

and naturally, the ITCZ position [*Chiang and Bitz, 2005; Kang et al., 2008, 2009; Frierson and Hwang, 2012; Donohoe et al., 2013*].

The double ITCZ bias is also a persistent problem even for the state-of-the-art coupled general circulation models (CGCMs). Analysis of CMIP5 (Coupled Model Intercomparison Project, phase 5) CGCMs shows clear double ITCZ bias in most models [*Li and Xie, 2014*], which could be attributed to the SST biases, and to a lesser extent, problematic precipitation-dynamics relationships [*Oueslati and Bellon, 2015*]. The double ITCZ problem in CMIP5 models has also been analyzed from an energetic perspective. Confirming the sensitivity experiments in a single GCM (e.g. Donohoe et al. 2013), the severity of the double ITCZ bias is positively correlated with the bias in cross-equator AET [*Hwang and Frierson, 2013; Adam et al., 2016*]. This has led to the conclusion that the double-ITCZ bias in current climate models can be attributed to the model deficiency in the extratropical energy balance over the Southern Ocean [*Hwang and Frierson, 2013*] and the NH extratropics [*Adam et al., 2016*]. However, the nature of these modeling studies has remained qualitative. Indeed, recent modeling studies have shown that reducing the Southern Ocean energy budget bias in fully coupled climate models does not lead to significant change in the ITCZ position because of the dominant role of oceanic energy transport in the interhemispheric energy balance [*Hawcroft et al., 2016; Kay et al., 2016*], and the exact magnitude of extratropical impact on tropical bias depends on the specific coupled and oceanic dynamics in the models [*Deser et al., 2015; Mechoso et al., 2016*]. As such, it remains unclear if and how the extratropics can impact tropical bias in climate models.

Another aspect of the double-ITCZ bias is the deficiency in precipitation close to the equator compared to the whole tropics, which contributes to the shape of two

precipitation peaks straddling the equator in GCMs. It has been found that the equatorial precipitation is directly related to the net energy input into the equatorial atmosphere, more than any extratropical sources [Adam *et al.*, 2016].

1.2. Extratropical Impact on El Niño-Southern Oscillation

(ENSO)

ENSO dominates the interannual variability of tropical climate and has significant global impacts. The dynamics of the El Niño-Southern Oscillation (ENSO) phenomenon has been studied extensively in the past 50 years. It has been recognized that the genesis of ENSO events depends critically on coupled ocean-atmosphere dynamic processes in the tropical Pacific [Philander, 1990; Neelin *et al.*, 1998]. In the meantime, more recent studies suggest that ENSO could also be triggered by extratropical atmospheric variability from the North Pacific through the “seasonal footprinting mechanism” (SFM) [Vimont *et al.*, 2001, 2003a, 2003b] or the North Pacific Meridional Model (NPMM) [Chiang and Vimont, 2004; Chang *et al.*, 2007], and from the South Pacific through the South Pacific Meridional Model (SPMM) [Zhang *et al.*, 2014], with the extratropical influence on the equatorial Pacific accomplished by the equatorward penetration of coupled ocean-atmosphere disturbances via the WES feedback [Liu and Xie, 1994; Liu, 1996; Vimont, 2010]. As such, extratropical climate variability and the associated tropical Pacific climate variability, such as NPMM, has also been suggested as a precursor for the onset of ENSO events [Anderson, 2007; Chang *et al.*, 2007; Larson and Kirtman, 2013, 2014].

The assessment of ENSO predictability relies upon the identification of such precursors that can act as triggers of ENSO events. Several precursors have been proposed in the literature. They include tropical precursors such as equatorial Pacific heat content

[*Jin, 1997*] and high-frequency wind variations in the form of wind bursts [*Hu et al., 2014; Fedorov et al., 2015*], as well as the aforementioned extratropical precursors like NPMM and SPMM. However, the interplay and relative importance of these different precursors is unclear. Correlations can be found between some precursors and ENSO events [*Chang et al., 2007*], but the limited sample size makes it difficult to analyze the relationship between precursors and ENSO events. Besides the short duration, observations are a mix of climate variability at all spatial and temporal scales, which makes it even harder to find causal relationships. Since ENSO is well known to exert a strong impact on extratropical climate over the Pacific [*Alexander et al., 2002; Liu and Alexander, 2007*] and therefore can be closely coupled with extratropical climate variability, the study of the extratropical impact on ENSO requires first to separate the triggering extratropical variability from the tropical ENSO variability itself before the extratropical impact on ENSO could be studied. The impact of extratropical climate variability on ENSO has been studied mainly in two approaches. In the first approach, the extratropical climate variability and its equatorial impact is statistically extracted from observations or a control simulation in a fully coupled general circulation model (CGCM) using linear statistical methods [*Vimont et al., 2001, 2003a, 2003b; Anderson, 2007; Yu et al., 2010; Larson and Kirtman, 2013, 2014*]. However, ENSO is known to exert a significant impact on extratropical climate variability, and its impact may not be filtered cleanly in the observation statistically [*Compo and Sardeshmukh, 2010*]. For example, the common practice of simple linear removal of an ENSO index from wind observations doesn't necessarily generate ENSO-independent wind data due to nonlinearity or non-simultaneous correlations. Therefore, the extratropical impact on ENSO may not be fully represented in this approach. In the second approach, the extratropical variability is simulated dynamically or specific

extratropical forcing is prescribed in a coupled model that filters out ENSO by employing a slab ocean [Vimont *et al.*, 2009; Newman *et al.*, 2011; Zhang *et al.*, 2014], and then its impact on ENSO can be studied using either statistical methods or another coupled model that incorporates ENSO dynamics. This approach can isolate the extratropical impact from ENSO variability, but the dynamics of the impact may not be well represented because of the use of different models. In either approach, the extratropical impact on ENSO is studied more from a statistical perspective, which makes it difficult to assess the role of extratropical impact for any specific ENSO event.

1.3. Coupled Data Assimilation (CDA)

As mentioned before, there are generally two approaches to studying extratropical control on tropical climate, namely observational analysis and model simulations. Each approach has its limits. For observational analysis, it is difficult to obtain causal relations from statistical inference, and it is almost impossible to isolate specific signals from observations of the real world. For model simulations, there is a dilemma between retaining coupled dynamics and using real world observations. One can either prescribe real world observations to force single-component GCMs and regional climate models, or use a fully coupled GCM but work within the limits of the model dynamics without direct implication for the real world.

As a complementary approach to the previous work, we attempt to study the extratropical impact on tropical climate explicitly using an approach derived from coupled data assimilation (CDA). We will prescribe the extratropical variability and climatology using an ensemble CDA scheme in a CGCM and then study the tropical responses, particularly ENSO and precipitation responses, of the coupled model to the extratropical forcing. The CDA, especially the ensemble Kalman filter (EnKF) and its

variations, has been used as a comprehensive strategy for generating climate reanalysis and initial conditions for prediction in the coupled climate system [*Zhang et al.*, 2007; *Saha et al.*, 2010; *Raeder et al.*, 2012; *Karspeck et al.*, 2013]. Here, we will use the CDA as a tool for the understanding of climate dynamics, specifically the extratropical impact on tropical climate in a GCCM. Ensemble-based data assimilation has been used in the study of atmospheric dynamics [*Hakim and Torn*, 2008; *Liu and Kalnay*, 2008; *Torn and Hakim*, 2008; *Kalnay et al.*, 2012; *Kunii et al.*, 2012], but seems to have not been used to investigate the coupled dynamics in a CGCM. An ensemble approach has been adopted in some previous studies mainly to reduce the atmospheric noises [*Kirtman and Shukla*, 2002; *Vimont et al.*, 2009].

Chapter 2

2. Model and Methods

2.1. Fast Ocean Atmosphere Model (FOAM)

The CGCM is the Fast Ocean Atmospheric Model (FOAM, version 1.5). FOAM is a fully coupled global atmosphere-ocean model with parallel implementation [Jacob, 1997]. The atmosphere component (PCC M3-UW) [Drake *et al.*, 1995]) is a spectral model with a R15 horizontal resolution (equivalent to $7.5^\circ \times 4.5^\circ$) and 18 vertical levels. The ocean component (OM3) is based on the Modular Ocean Model (MOM) [Cox, 1984] created by the Geophysical Fluid Dynamics Laboratory (GFDL). It has a horizontal resolution of $2.8^\circ \times 1.4^\circ$ and a z-coordinate with 24 vertical levels. The land surface and sea ice models are based on those of Community Climate Model 2 (CCM2) [Hack *et al.*, 1993]. Without flux adjustment, a 6000-model-year simulation of FOAM shows no apparent drift in tropical climate [Liu *et al.*, 2007b]. FOAM can capture most major features of the observed global climatology as in some more advanced CGCMs. It also shows reasonable climate variability in regions such as the tropics [Liu *et al.*, 2000, 2004], the North Pacific [Wu *et al.*, 2003; Liu *et al.*, 2007a], and the North Atlantic [Wu and Liu, 2005].

2.2. CDA System in FOAM

Ensemble-based analysis techniques such as EnKF [Evensen, 1994; Houtekamer and Mitchell, 1998] and Ensemble Adjustment Kalman Filter (EAKF) [Anderson, 2001, 2003] have emerged as viable options for CDA systems in complex systems such as a CGCM. EAKF, in particular, was used to develop the first ensemble-based CDA system in a fully coupled general circulation model [Zhang *et al.*, 2007].

The CDA system in FOAM [Liu *et al.*, 2014a, 2014b; Lu *et al.*, 2015b] uses EAKF and includes both atmosphere data assimilation (ADA) and ocean data assimilation (ODA). All experiments in this study use an ensemble size of 16, similar to previous studies [Liu *et al.*, 2014b; Lu *et al.*, 2015b]. We applied several filtering techniques to improve and stabilize this CDA system, including covariance inflation, covariance localization and incremental analysis update. Considering the moderate ensemble size and the model bias when assimilating real world observations, covariance inflation is needed to stabilize the assimilation. Because of its superior stability when dealing with drastically variable observation density, a relax-to-prior scheme [Zhang *et al.*, 2004] is used for both atmospheric and oceanic updates over a multiplicative covariance inflation scheme [Hamill and Whitaker, 2005]. The relaxation factor is set at 0.5 for all experiments. Covariance localization scheme [Houtekamer and Mitchell, 1998; Hamill *et al.*, 2001] is also adopted in this system to reduce the impact of remote observations. Incremental analysis updates [Bloom *et al.*, 1996] is a method to reduce the initial shock introduced by assimilating observations.

The CDA system can assimilate temperature and salinity observations in the ocean and temperature and wind observations in the atmosphere. The update algorithm also uses the covariance between model variables, both within a single model component and across different model components. The latter capability, also called the Strongly Coupled Data Assimilation (SCDA) will be further described in section 2.3

2.3. Strongly Coupled Data Assimilation (SCDA)

There are two levels of coupling in regards to the exchange of information in the analysis stage of a CDA system [Han *et al.*, 2013; Liu *et al.*, 2013]. In the weakly coupled data assimilation (WCDA), the analysis increments are calculated and applied separately

in each model component such that the coupling between different components is accomplished only dynamically through cross-component fluxes in the forecast stage. ADA and ODA are the two most common components of a WCDA system. In contrast, the SCDA applies the analysis increments using the fully coupled error covariance, especially the coupled covariance between variables from different model components (hereafter cross covariance). As a result, the coupling between different components is accomplished not only dynamically in the forecast stage, but also statistically through the coupled covariance in the analysis stage. In an SCDA system, the observed information in one model component can be directly projected onto another, resulting in instantaneous adjustment and balanced analysis increments. The WCDA has been adopted in some state-of-the-art CDA systems [*Zhang et al., 2007; Sugiura et al., 2008; Saha et al., 2010*], however, the use of SCDA has remained in the exploration stage.

In principle, the use of cross covariance should add additional information and improve the analysis. This has been recognized, for example, in a simple coupled model study (Liu et al. 2013). However, the implementation of the SCDA in CDA systems faces many challenges, such as time-scale differences, different analysis schemes among components, cost of computation, etc. The mismatch of time scales of variability between different components causes the coupled covariance to be dominated by noise of the variables from the fast component. Therefore, in an ensemble-based filter with a finite sample size, it is difficult to estimate the coupled covariance accurately, and sampling the coupled covariance may introduce more noise than signal and deteriorate the analysis. For instance, a recent study [*Han et al., 2013*] using a biased-model framework and a simple coupled model found that the SCDA does not improve the analysis quality compared to the WCDA unless a very large ensemble size on the scale of 10000 is used.

In addition, it is more difficult to improve the quality of analysis in the fast component through cross update, since observations from the slow component do not contain enough information about the high-frequency variability.

The physical characteristics of a coupled climate system could provide ways to improve the accuracy of sampling the cross covariance. In a typical midlatitude ocean–atmosphere coupled system, the ocean–atmosphere interaction is dominated by the stochastic forcing of the atmospheric internal variability on the slow ocean, such that the ocean–atmosphere lead–lag correlation shows a strong asymmetry. More specifically, the cross correlation is small at the zero lag and reaches maximum when the atmosphere leads the ocean by about the decorrelation time of the atmosphere [*Hasselmann, 1976; Barsugli and Battisti, 1998*]. This asymmetry could potentially benefit the cross update if the high correlation between the ocean and the preceding atmosphere could be used to enhance the signal-to-noise ratio when calculating the corresponding cross covariance. To further boost the accuracy of sampling the covariance, the leading correlations could be combined with the use of time-averaged observations [*Huntley and Hakim, 2010*], which leads to even higher correlation with the oceanic state. Some recent studies [*Tardif et al., 2014a, 2014b*] utilized the high correlations between time-averaged atmospheric and oceanic variables. In their cases, the slow meridional overturning circulation (MOC) benefits from the cross update using time-averaged atmospheric observations.

In a two-part paper, we proposed the Leading Averaged Coupled Covariance (LACC) method to improve the effectiveness and efficiency of cross update in an SCDA system. In Part 1 [*Lu et al., 2015a*], we proposed the LACC method and tested it in a simple coupled model. The LACC method utilizes the asymmetric ocean–atmosphere coupling dynamics by using the leading forecasts and observations of the fast atmospheric variables. This

leads to increased cross correlation and enhanced signal-to-noise ratio during cross update. To further reduce the sampling error, the leading atmospheric states are averaged over time to produce even higher correlations [Dirren and Hakim, 2005; Huntley and Hakim, 2010; Tardif et al., 2014a]. In the simple coupled model of Part 1, the LACC method significantly increases the cross correlation for the cross update and reduces the analysis error of the slow model variable compared to both the WCDA and the regular SCDA without LACC [Lu et al., 2015a].

The LACC method was then used to setup an SCDA system in FOAM. To our knowledge, this was the first successful application of an SCDA scheme in a CGCM. In a perfect-model framework, the SCDA system implements cross update from the atmosphere component (low-level air temperature) to the ocean component (SST), utilizing the coupled covariance between atmosphere temperature and SST. The details of the SCDA system and LACC method in FOAM can be found in [Lu et al., 2015b].

We showed that, although the direct SCDA using simultaneous cross covariance (SimCC) fails to improve upon the WCDA, the SCDA with the LACC method can indeed improve upon the WCDA significantly. The WCDA system refers to the CDA system described in Chapter 2.2. Figure 2.1 shows the zonal mean RMSE of monthly SST analysis of the SimCC and the LACC method with different averaging lengths, normalized by the WCDA. “AveX” means that cross update is done every X days with the X-day-averaged leading T_s (surface air temperature). The SimCC method performs poorly across all latitudes except for the deep tropics between $10^\circ S$ and $10^\circ N$, where the simultaneous correlations are the largest and the SimCC can indeed reduce the RMSE of monthly SST by up to 10%. Nevertheless, the SCDA using SimCC is far from an acceptable scheme because of its much poorer analysis outside the equatorial region. The RMSE increases by

up to 70% over WCDA in the mid-latitude in both hemispheres. As the averaging length becomes longer, the cross update with the LACC method begins to have a consistently positive impact on the system. The optimal case, the “Ave7” experiment, notably outperforms the benchmark WCDA experiment: its RMSE of SST is reduced by 10% to 20% between 24°S and 33°N, and remains smaller than the WCDA across the entire domain, except for the very northern part ($> 40^{\circ}N$).

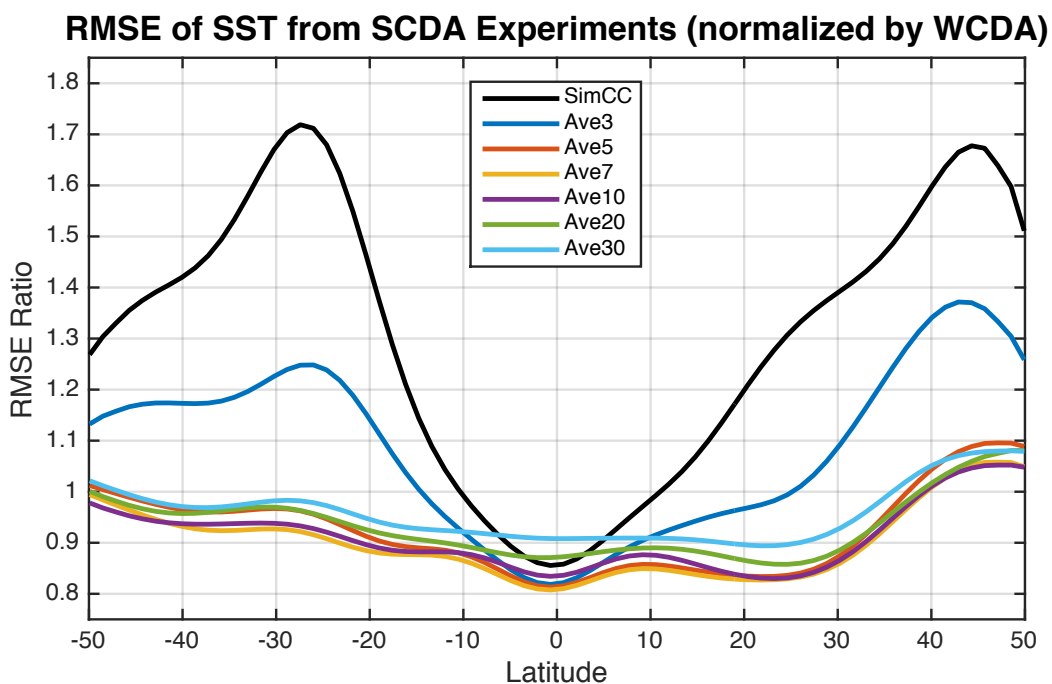


Figure 2.1 Zonal-mean RMSE (Root Mean Square Error) of monthly SST from the SimCC experiment and the LACC experiments with different averaging lengths, normalized by the WCDA experiment. (from [Lu *et al.*, 2015b])

A detailed comparison is made between the under-performing SimCC and the optimal “Ave7”. Figure 2.2 shows the spatial distribution of the RMSE of SST from the SimCC experiment normalized by the WCDA, the “Ave7” experiment normalized by the WCDA, and the “Ave7” experiment normalized by the SimCC. The zonal average of Figure 2.2a and b will produce the curves of SimCC and Ave7 in Figure 2.1, respectively. Aside from the zonal-mean features already demonstrated in Figure 2.1, Figure 2.2a shows that

the improved SST in the SimCC experiment expands into higher latitudes in the Atlantic and the eastern Pacific where the simultaneous correlations are relatively large (not shown). Figure 2.2b shows that the inferior analysis quality of “Ave7” north of $40^{\circ}N$ is the result of larger RMSE in the northwestern Pacific and northwestern Atlantic than the WCDA. These inferior analyses, we speculate, are caused by two reasons. First, they could be attributed to the small ensemble correlations north of $40^{\circ}N$ as well as the small correlations in those specific areas. Second, they could also be caused by the large analysis errors of air temperature over land and their westward extension. Since the observation innovations for the cross update are calculated from the observation and forecast of air temperature, the poor quality of air temperature analysis leads to less accurate observation innovations and less effective cross update. Directly comparing “Ave7” to SimCC (Figure 2.2c), the RMSE ratio in the tropics is very close to 1, while the analysis quality is improved across most of the extra-tropics.

As shown in Figure 2.1, the averaging length is a critical parameter governing the performance of the LACC method [*Tardif et al.*, 2014a; *Lu et al.*, 2015a]. In each SCDA system with fixed observations, ensemble size, ADA/ODA frequencies and analysis schemes, there are two competing factors that determine the optimal averaging length. The first is the magnitude of the leading averaged cross correlation, which controls the signal-to-noise ratio when estimating the sample covariance for cross update. This correlation usually increases rapidly with the averaging length starting from 1, peaks at a certain length and eventually declines. The other is the frequency of cross update, since a longer averaging length implies less frequent assimilation through coupled covariance and therefore less constraint by atmospheric observations on the ocean. The competing effects of these two factors usually result in an optimal length, which tends to be longer in

the case of a system with larger noise [Lu *et al.*, 2015a]. In a CGCM like FOAM, these factors are not spatially homogeneous, yet, the length of 7 days, which is close to the decorrelation time of the atmosphere surface temperature, seems to be the optimal choice for most latitudes. A longer 10 days is slightly better for higher latitudes south of 40°S and north of 40°N , which also agrees with [Lu *et al.*, 2015a], since the higher latitudes have smaller correlations. Changes in the observations, ensemble size, configuration of ADA/ODA and analysis schemes could all lead to different optimal averaging lengths. The sensitivity of the optimal average length in a complex CGCM like FOAM, however, remains to be studied in the future.

Compared to SimCC, the improvement from the LACC method mainly comes from the increased cross correlations compared to the simultaneous correlations, due to the use of leading averaged atmosphere temperature, which enhances the signal-to-noise ratio in calculating the coupled covariance for the cross update. The success of the LACC method indicates the potential to combine coupling dynamics with proper statistical techniques to improve coupled data assimilation systems.

The success of [Lu *et al.*, 2015b] demonstrates the potential to apply the SCDA in state-of-the-art CGCMs. With an SCDA system, currently assimilated observations can be used more effectively, and information from a well-observed component like the atmosphere can be directly projected to a less-observed or unobserved component such as the ocean or the land. Compared with the WCDA systems that are currently being established for some major reanalysis projects, SCDA systems, in principle, would produce a more accurate and balanced analysis of the coupled state and provide better initialization for predictions.

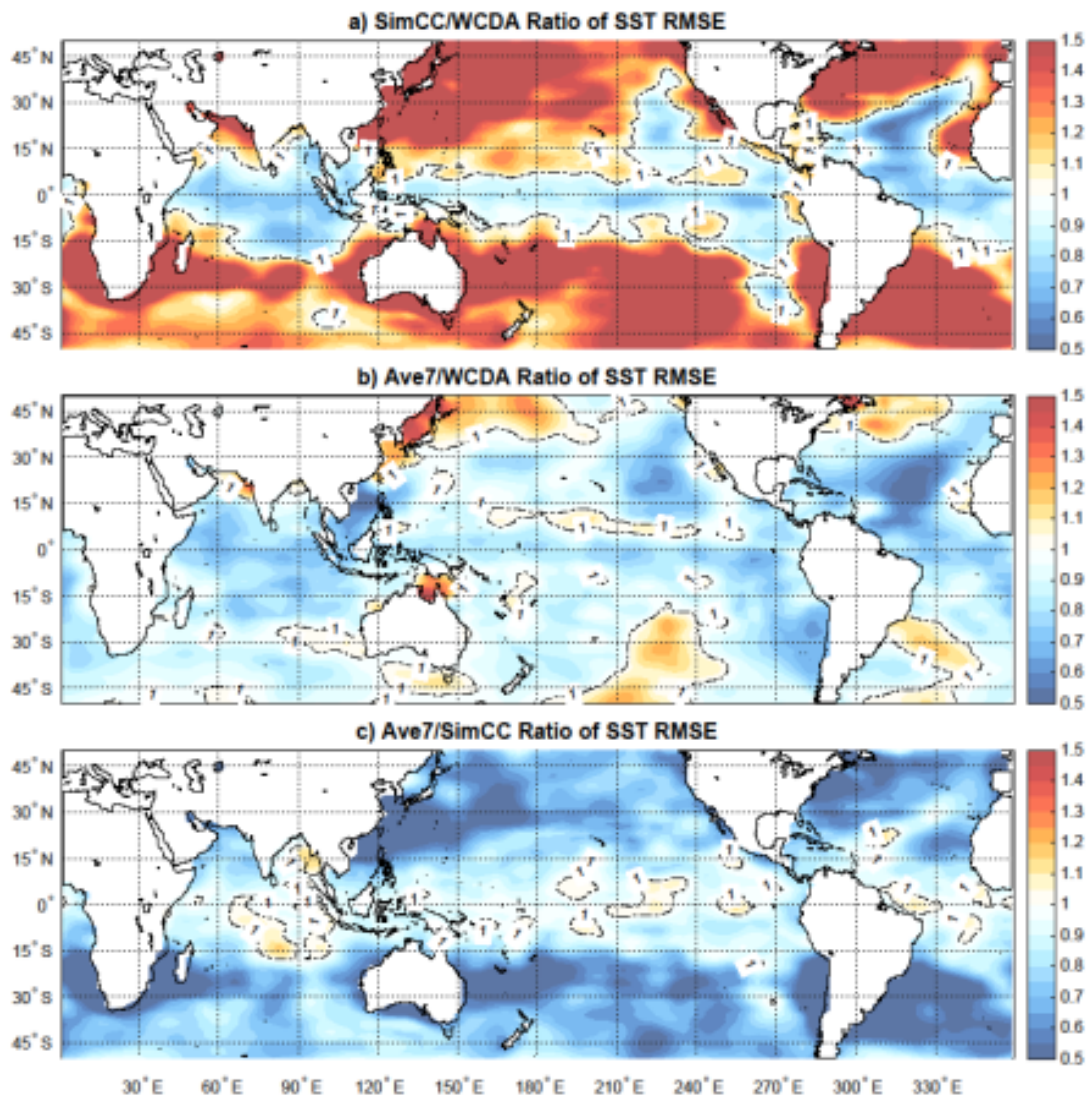


Figure 2.2 Spatial distribution of the RMSE of monthly SST from a) the SimCC experiment (normalized by the WCDA), b) the “Ave7” experiment (normalized by the WCDA), and c) the “Ave7” experiment (normalized by the SimCC). (from [Lu *et al.*, 2015b])

2.4. Regional Coupled Data Assimilation (RCDA)

Based on the CDA system in FOAM, the RCDA method limits the assimilation to the desired model variables and domain, then analyzes the ensemble-mean model responses in regions without the assimilation of observation. Because of the flexibility of the ensemble-based Kalman filter, the data assimilation can be selectively activated for any model variable in any region. In other words, the system could proceed with only a subset

of the global observations. If both ADA and ODA are active over the entire globe, the end result is like a “reanalysis” product and the model is closely constrained by the observations everywhere [Zhang *et al.*, 2007; Lu *et al.*, 2015b]. If the data assimilation is active only in a limited region, the product shows the impact of the observations in the chosen region on the evolution of the coupled model outside the assimilation region, similar to the observation sensitivity experiments (e.g. Kunii *et al.* 2012).

In Chapter 3, the RCDA method is used to study the extratropical influence on the tropical bias in FOAM dynamically, systematically and quantitatively [Lu *et al.*, 2017a]. RCDA experiments show that the model’s double-ITCZ bias is improved systematically when SST, air temperature and wind are corrected toward real world data from the extratropics into the tropics progressively. More quantitatively, the tropical asymmetry bias in precipitation and surface temperature is reduced by 40% due to extratropical impact from outside of $\sim 25^\circ$. Coupled dynamics, as well as atmospheric and oceanic processes, play important roles in this extratropical-to-tropical teleconnection. Energetic analysis of cross-equatorial atmospheric energy transport and equatorial net energy input are used to explain the changes in the precipitation bias. We also discuss the implications of our RCDA method and experiments for diagnosing the sources of the tropical bias in climate models.

In Chapter 4 and Chapter 5, the RCDA method is used to study the extratropical control on the El Niño-Southern Oscillation (ENSO) variability in FOAM. Extratropical observations are assimilated, both in a perfect-model framework [Lu *et al.*, 2017b] and with real world observations, and the ensemble-mean ENSO response is analyzed to study the dynamics, precursors and predictability of ENSO variability in FOAM and the real world.

The perfect-model experiments demonstrate significant control of extratropical atmospheric forcing on ENSO variability in FOAM. When atmospheric “observations” are assimilated only poleward of 20° in both hemispheres, most ENSO events in the “observation” are reproduced and the error of the Nino3.4 index is reduced by over 40% compared to the ensemble control experiment that does not assimilate any observations. Further experiments with the assimilation in each hemisphere show that the forced ENSO variability is contributed roughly equally and independently by the Southern and Northern Hemisphere extratropical atmosphere. Further analyses of the ENSO events in the southern hemisphere forcing experiment reveal robust precursors in both the extratropical atmosphere over southeastern Pacific and equatorial Pacific thermocline, consistent with previous studies of the South Pacific Meridional Mode and the discharge-recharge paradigm, respectively. However, composite analyses based on each precursor show that neither precursor alone is sufficient to trigger ENSO onset by itself and therefore neither alone could serve as a reliable predictor.

RCDA experiments with real world reanalysis data demonstrate extratropical control on certain historical ENSO events. The effectiveness of several common ENSO precursors in triggering strong historical ENSO events (equatorial heat content, westerly wind bursts, NPMM and SPMM) is compared and discussed. Additional forecast and forced experiments identify the relative importance of each precursor for a few extreme ENSO events.

Chapter 3

3. Extratropical Influence on Tropical Climatology

The RCDA method is first used to study the extratropical influence on the tropical bias in FOAM dynamically, systematically and quantitatively [Lu *et al.*, 2017a]. The essence of the RCDA method here is to quantify, when allowing the full ocean-atmosphere coupling, the degree by which accurately improving large-scale model variability and climatology in the extratropics could reduce the tropical bias in a CGCM. The combination of observational constraint, coupled dynamics and ensemble approach gives the RCDA method unique advantages when investigating teleconnections of inherently coupled problems such as ENSO and double-ITCZ bias.

3.1. Methods

3.1.1. Datasets

The assimilated datasets include daily-mean air temperature and wind components from the NCEP/NCAR Reanalysis 1 [Kalnay *et al.*, 1996] and monthly-mean SST from NOAA ERSST [Huang *et al.*, 2015, 2016; Liu *et al.*, 2015]. We use 68 years of data from 1948/01, start of the NCEP/NCAR Reanalysis 1, to 2015/12, end of the most recent year at the time of this study. Monthly CMAP data from 1979 to 2015 are used as precipitation observation [Xie and Arkin, 1997]. All data are interpolated to FOAM grids before assimilation or comparison.

3.1.2. Experiment Design

All RCDA experiments use the same ensemble of initial conditions, which are the restart files after a 10-year ensemble control present-day FOAM simulation that started

with the same ocean initial conditions and slightly different atmosphere initial conditions. The RCDA experiments run for 68 years (1948-2015). Since the CMAP data are only available since 1979, the last 37 years (1979-2015) of the output are used to match the precipitation record. The same 37-year period from NCAR/NCEP Reanalysis 1 and ERSST is used for all model-data comparison. The analysis is repeated using all 68 years from RCDA experiments, NCAR/NCEP Reanalysis 1 and ERSST, and the effects on the results and conclusions are minimal.

3.1.3. Assimilating Reanalysis Data

Reanalysis datasets instead of actual observational data (satellite, radiosonde, ocean floats, etc.) are assimilated to facilitate this study. Given our limited resources, it is unrealistic to develop and operate a coupled data assimilation system that assimilates huge amounts of raw observations, which are irregular in space and time, and sometimes indirect measurements of the target variables. Such comprehensive assimilation systems are only available at a few of the most advanced institutions around the globe, such as NCAR, GFDL and ECMWF. The advantages and caveats of assimilating reanalysis data instead of actual observations are investigated by [Liu *et al.*, 2016]. Through sensitivity experiments in a simple coupled model, it is found that assimilating reanalysis-like data resulted in a 5-20% increase, depending on assimilation schemes and experiment setup, of error in the synoptic variability of the final assimilation products. Considering the small sacrifice in assimilation quality and the significant relief in required resources, we chose to assimilate reanalysis data in this study.

One challenge of assimilating reanalysis datasets is to determine their uncertainties. The uncertainties or errors of reanalysis data are not readily available, and understandably difficult to quantify considering that reanalysis datasets are the

combination of state-of-the-art climate models and millions of observations of various types. Therefore, we use the typical observational uncertainties as in previous studies of similar systems [*Zhang et al.*, 2007; *Liu et al.*, 2014b; *Lu et al.*, 2015b, 2017b]: 0.5 K for monthly-mean SST; 1 K for daily-mean atmosphere temperature; and 1 m/s for daily-mean wind components. Key experiments are repeated with smaller observational uncertainties (0.2 K/0.5 K/0.5 m/s, respectively) and the impacts on the results and conclusions are minimal.

3.2. Tropical Asymmetry Bias of Precipitation

Assimilated Variables & Latitudes	None	Atm T/U/V & SST (coupled)	Atm T/U/V	SST
None	<i>CTRL</i>			
All		<i>CDA_ALL</i>	<i>ADA_ALL</i>	<i>ODA_ALL</i>
>10°N & <10°S		<i>CDA_10</i>	<i>ADA_10</i>	<i>ODA_10</i>
>15°N & <15°S		<i>CDA_15</i>	<i>ADA_15</i>	<i>ODA_15</i>
>20°N & <20°S		<i>CDA_20</i>	<i>ADA_20</i>	<i>ODA_20</i>
>24°N & <24°S		<i>CDA_24</i>	<i>ADA_24</i>	<i>ODA_24</i>
>28°N & <28°S		<i>CDA_28</i>	<i>ADA_28</i>	<i>ODA_28</i>
>33°N & <33°S		<i>CDA_33</i>	<i>ADA_33</i>	<i>ODA_33</i>
>37°N & <37°S		<i>CDA_37</i>	<i>ADA_37</i>	<i>ODA_37</i>
>42°N & <42°S		<i>CDA_42</i>	<i>ADA_42</i>	<i>ODA_42</i>

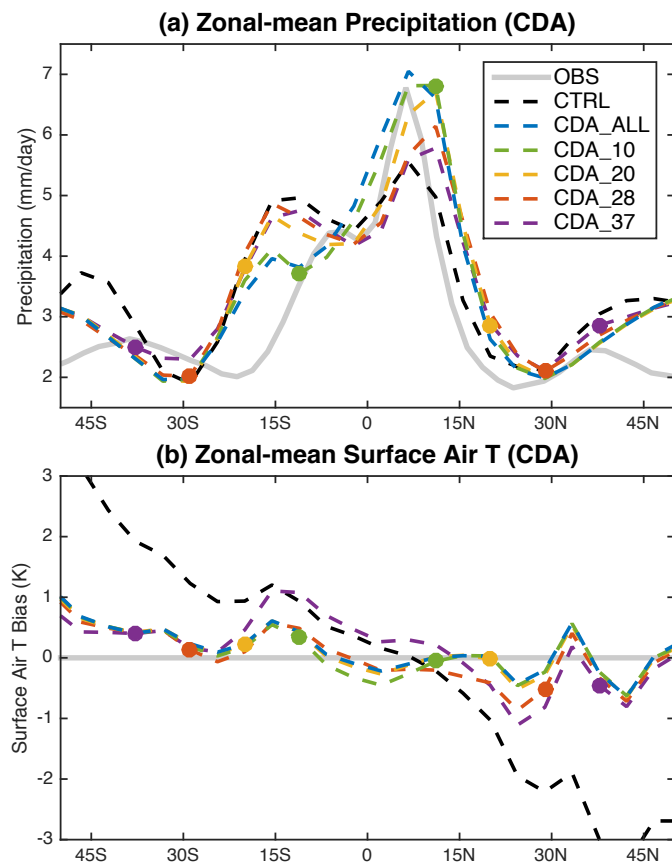
Table 3.1 Table of all RCDA experiments in Chapter 3. (from [*Lu et al.*, 2017a])

The extratropical impact on tropical bias in FOAM is quantified using a series of RCDA experiments in which the coupled climate is corrected towards real world

observations progressively from the extratropics to the equator (see Table 3.1 for a complete list of the RCDA experiments). The ensemble control simulation without assimilation (*CTRL* hereafter) shows significant tropical bias in precipitation, SST and wind (Figure 3.1 and Figure 3.2) in the model. The zonal- and annual-mean precipitation shows two peaks of comparable magnitude straddling the equator, while in sharp contrast, the northern peak is twice as large as the southern peak in the observation (Figure 3.1a). Coupled with the double-ITCZ bias, the surface air temperature exhibits a significant warm (cold) bias in the SH (NH) extratropics (black dashed line in Figure 3.1b). The southern tropical rainfall peak results partly from excessive precipitation in southern tropical Pacific and Atlantic, which is closely coupled with the biases of warm SST and weak trade wind there (Figure 3.2c).

FOAM is also wetter overall in the tropics by 14%, averaging to 4.56 mm/day of precipitation between 20°S and 20°N compared to 4.00 mm/day in observation.

Figure 3.1 Zonal-mean climatological precipitation and surface air temperature of selected CDA experiments, along with observation and CTRL. (a) Total precipitation. (b) Surface air temperature bias from observation. Filled circles indicate the data assimilation boundaries when applicable. (from [Lu et al., 2017a])



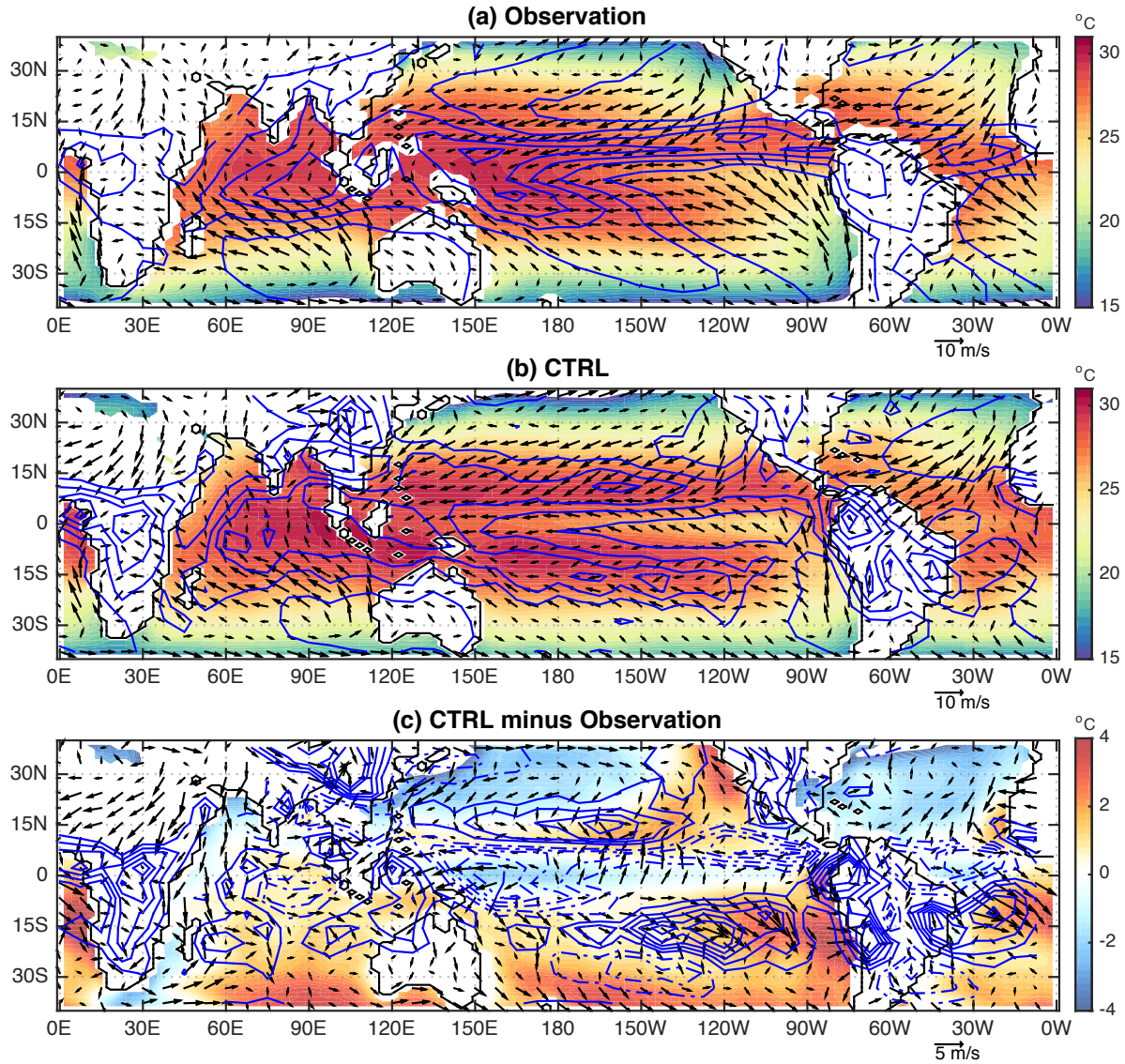


Figure 3.2 Climatological SST (shadings), precipitation (contours with 2 mm/day interval) and surface wind (arrows). (a) Observation. (b) CTRL. (c) Difference of CTRL minus observation. (from [Lu et al., 2017a])

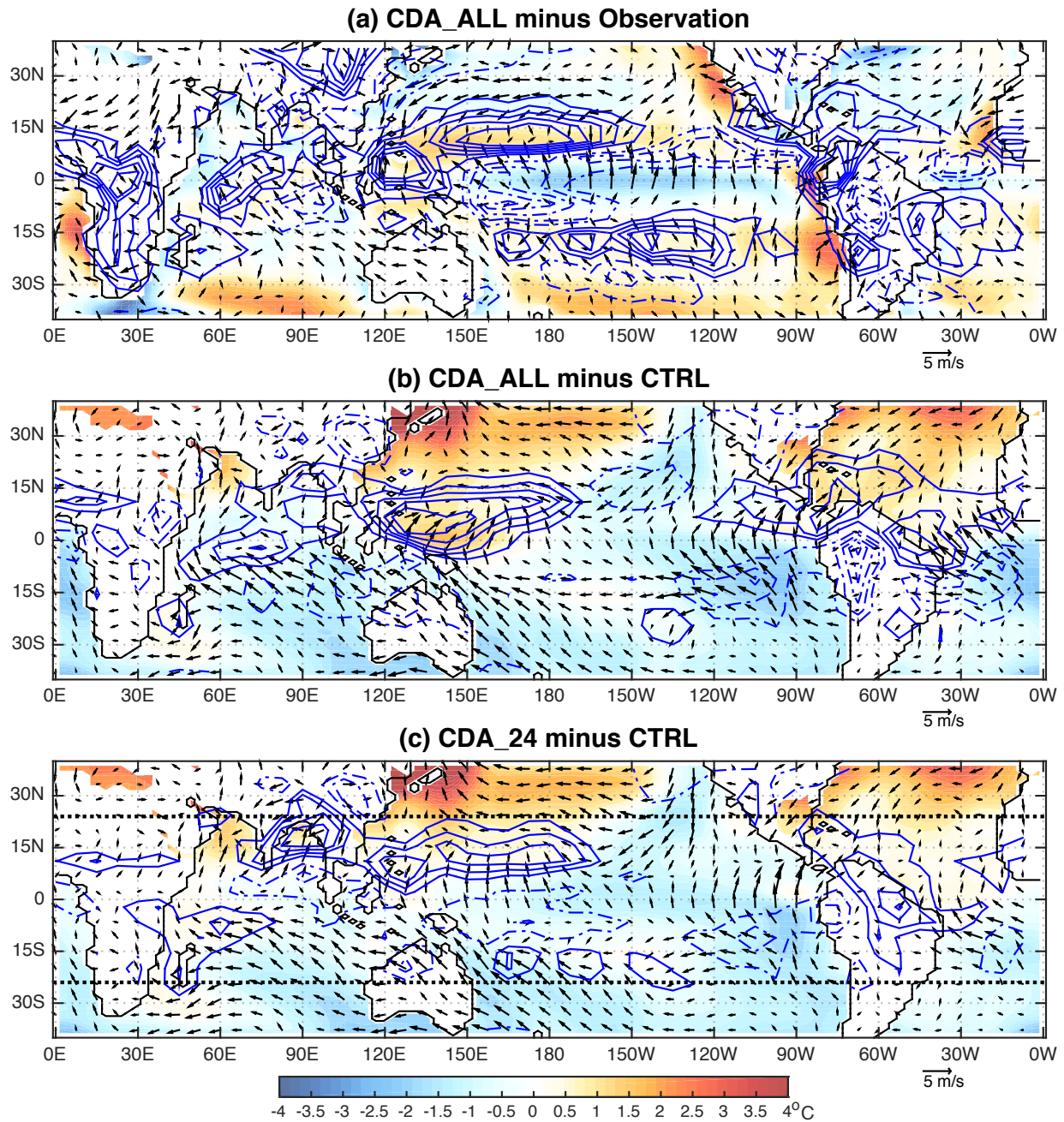
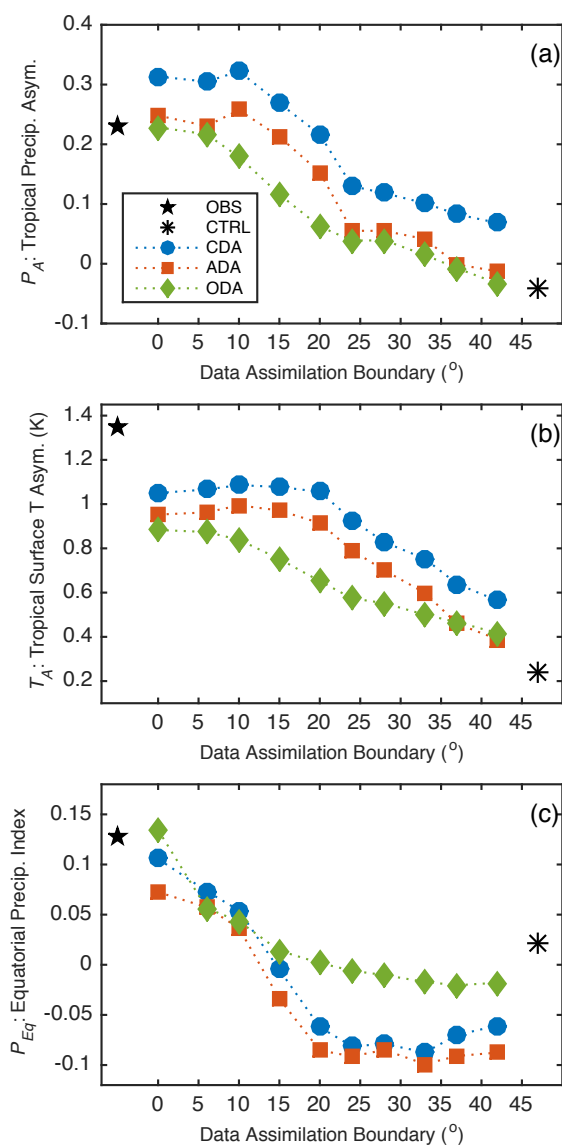


Figure 3.3 Differences in climatological SST (shadings), precipitation (contours with 2 mm/day interval) and surface wind (arrows). (a) Between *CDA_ALL* and observation. (b) Between *CDA_ALL* and *CTRL*. (c) Between *CDA_24* and *CTRL*. The horizontal dotted lines indicate the data assimilation boundaries of *CDA_24*. (from [Lu et al., 2017a])

As the coupled model climate is corrected towards the observation progressively from poleward of 37° to all latitudes (*CDA_37* to *CDA_ALL*), the NH tropical precipitation

peak is enhanced while the SH peak is reduced, reducing the tropical bias systematically (Figure 3.1a). Accompanying the precipitation change is the reduced bias in tropical surface temperature that is not directly updated by data assimilation (say between 20°N and 20°S in *CDA_28*). The reduction of precipitation bias from *CTRL* to *CDA_ALL* is contributed primarily by reduced precipitation over the southeastern tropical Pacific, southeastern tropical Indian and southern tropical Atlantic Oceans, and enhanced precipitation over oceans north of the equator (Figure 3.3b). It is notable that, even with observations assimilated all the way to the equator, *CDA_ALL* still suffers from precipitation bias, such as excessive precipitation in the tropics. This implies deficiencies in the model's land component and precipitation-dynamics relationship, which could not be improved by the current assimilation. The tropical climatology in *CDA_ALL*, despite its biases, will thus serve as the optimal achievable scenario in FOAM against which other experiments will be measured.

Figure 3.4 A summary of annual-mean climatological indices from observation (pentagon), FOAM control (asterisk), *CDA* (blue circle), *ADA* (red square), and *ODA* (green diamond) experiments. (a) Tropical precipitation asymmetry index P_A . (b) Tropical surface temperature asymmetry T_A . (c) Equatorial precipitation index P_{Eq} . (from [Lu et al., 2017a])



The tropical asymmetry bias is reduced systematically when the assimilation domain expands towards the equator. This is seen more clearly from the tropical precipitation asymmetry index P_A (Figure 3.4a). P_A is defined as the area-averaged precipitation in the NH tropics (0° - 20° N) minus that in the SH tropics (0° - 20° S) normalized by that in the whole tropics (20° S- 20° N) [Hwang and Frierson, 2013; Adam et al., 2016]. With no assimilation, *CTRL* has a slightly negative P_A of -0.04, indicating more precipitation in the SH tropics than in the NH tropics, while in sharp contrast, the observation has significantly more precipitation in the NH tropics with a P_A over 0.2. When the extratropical assimilation domain expands equatorward, P_A gradually increases, eventually exceeding the observation. The increase of P_A is caused by the observations assimilated in the extratropics (*CDA_28* relative to *CTRL*) and subtropics (*CDA_20* relative to *CDA_28*), but not in the deep tropics (*CDA_ALL* relative to *CDA_10*). The assimilation in the deep tropics, however, will later be shown to affect equatorial precipitation, another aspect of the tropical bias. The higher-than-observed P_A when the assimilation expands inside 20° is a result of excessive precipitation in the northern tropics. Similar response to extratropical forcing is also seen in the tropical surface temperature asymmetry index T_A (Figure 3.4b), defined as the difference between area-averaged bottom-level air temperature in the northern tropics (0° - 20° N) and that in the southern tropics (0° - 20° S), consistent with the strong correlation between P_A and T_A as in previous studies [Donohoe et al., 2013; Hwang and Frierson, 2013; Adam et al., 2016]. T_A saturates below the observed value due to the still biased land model. We should note that the jump of P_A from *CDA_24* to *CDA_20* is not an artifact of the domain (20° S- 20° N) we choose to calculate P_A . A different domain (15° S- 15° N) results in the same jump in P_A .

Instead, it is rather a dynamical response to the fact that the additional assimilation from *CDA_24* to *CDA_20* starts to directly alter the trade winds, thus affecting the tropical precipitation more strongly.

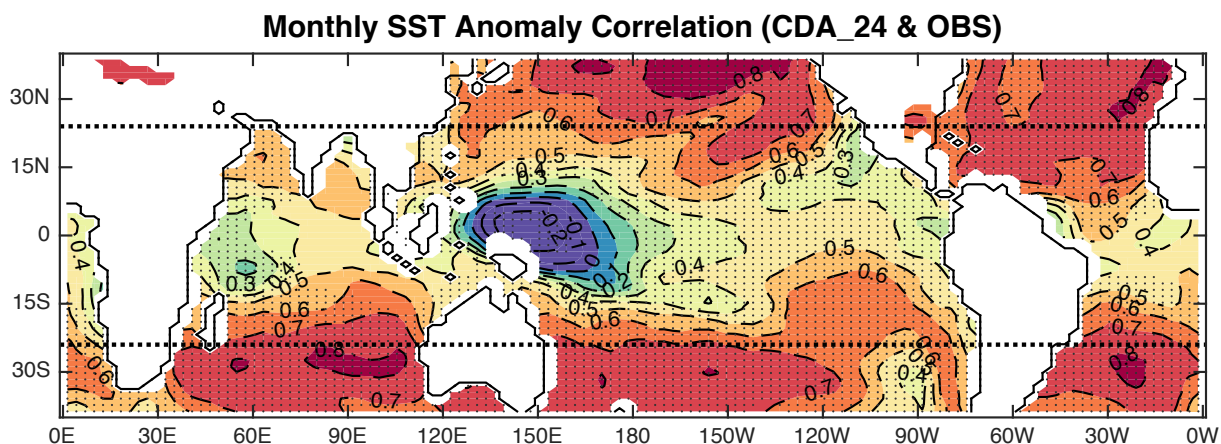


Figure 3.5 Correlation of monthly SST anomaly between *CDA_24* and observation. The dotted points indicate that significance level of the correlation is over 99% based on a Student-t test. The horizontal dotted lines indicate the data assimilation boundaries of *CDA_24*. (from [Lu *et al.*, 2017a])

The reduced biases in the tropical precipitation and temperature asymmetries when the observation is assimilated poleward of 30° or even 40° are clear evidence of significant extratropical influence on tropical climatology in FOAM. More quantitatively, the tropical asymmetry bias in precipitation and surface temperature is reduced by about 40% from extratropical impact outside of 25° (Figure 3.4a and b). The extratropical influence could be communicated to the tropics by atmospheric dynamics through the transient eddy energy fluxes [Kang *et al.*, 2008, 2009]. The extratropical influence can also be accomplished by surface ocean-atmosphere coupling through the WES feedback [Liu and Xie, 1994]. This can be seen, for example from *CDA_24*, in the tongues of high correlation of SST anomalies between the observation and model, which penetrate the tropics primarily in the eastern parts of the oceans (Figure 3.5). Similar pathways have been

found to support the extratropical control on ENSO variability in FOAM [Vimont *et al.*, 2009; Lu *et al.*, 2017b]. These high SST correlation tongues correspond approximately to the regions with large bias reduction in SST and precipitation, indicating the consistency between improved variability and climatology due to extratropical impact. Furthermore, extratropics may also influence the tropical climatology through equatorward ventilation and equatorial upwelling in the ocean [Liu *et al.*, 1994; Yang and Liu, 2005]. This oceanic process is on the decadal timescale and therefore fully effective for climatological influence. This process could also be effective when only mid- and high-latitude oceans have assimilation. For example, when comparing *CDA_42* to *CTRL*, the 0-400m ocean temperature in the tropics is significantly different (Figure 3.6), and the change in oceanic energy transport accounts for a majority of the total change in meridional energy transport at most latitudes (Figure 3.7). This important role of ocean dynamics in the extratropical climatological impact on the ITCZ is consistent with recent fully coupled model studies [Hawcroft *et al.*, 2016; Kay *et al.*, 2016].

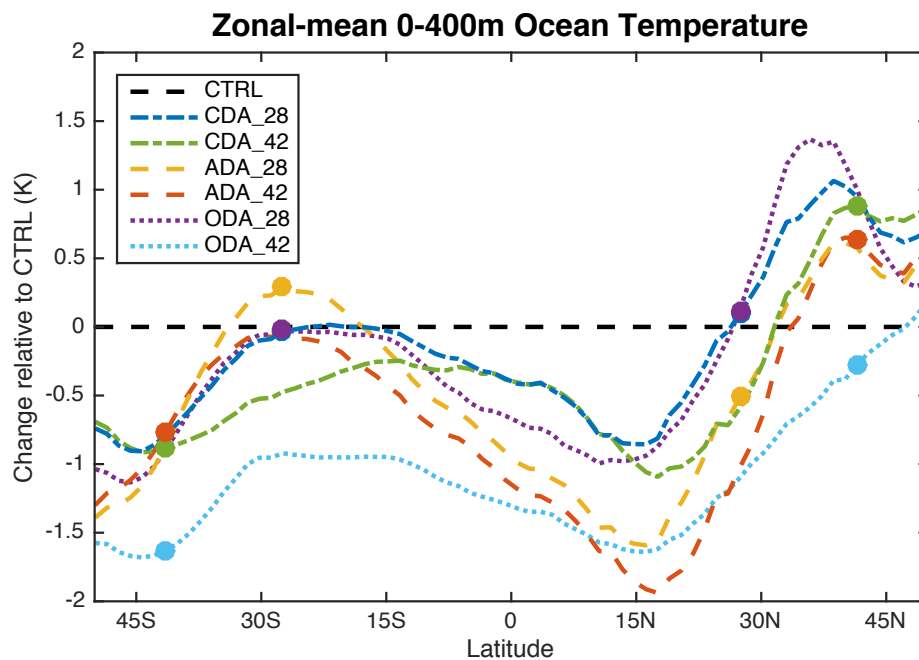


Figure 3.6 Zonal-mean climatological 0-400m average temperature change from CTRL for *CDA_28*, *CDA_42*, *ADA_28*, *ADA_42*, *ODA_28* and *ODA_42* experiments. Filled circles indicate the data assimilation boundaries where applicable. (from [Lu et al., 2017a])

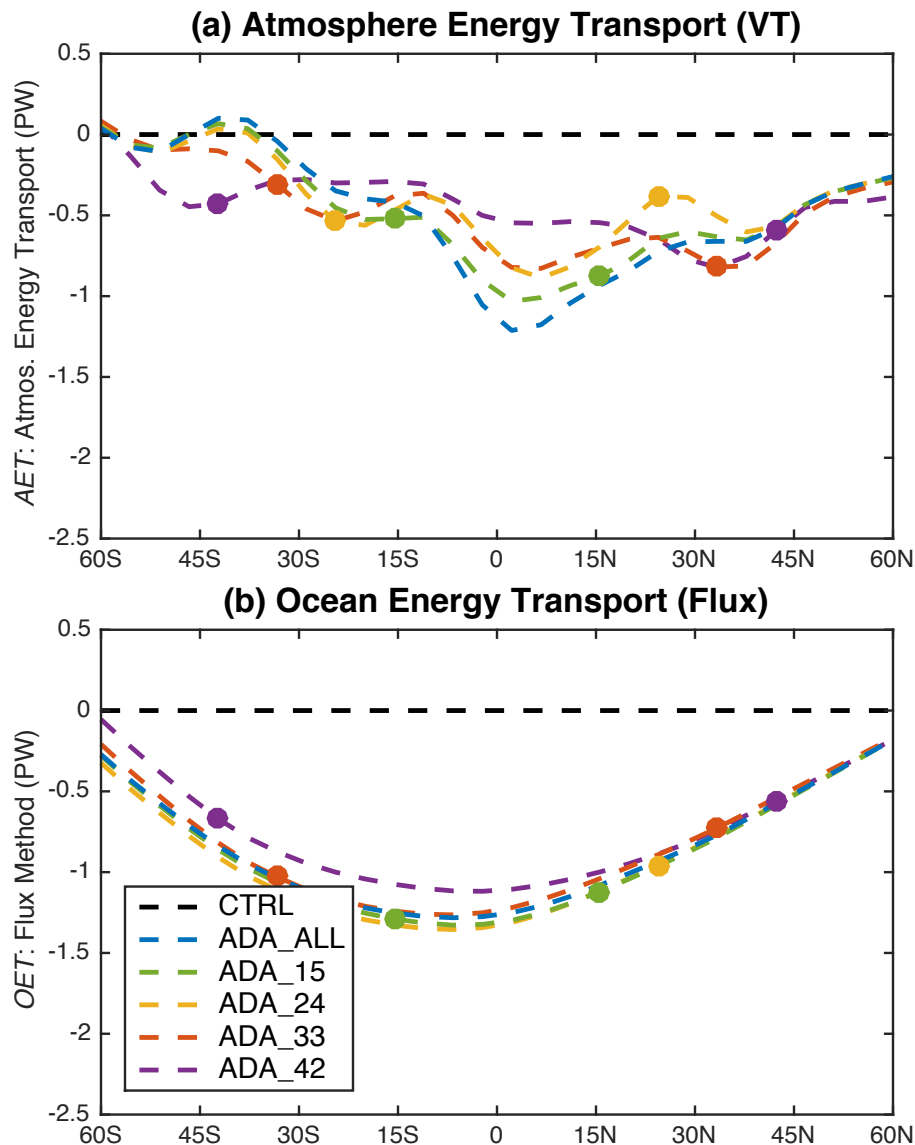


Figure 3.7 Changes in meridional energy transport by the (a) atmosphere and (b) ocean from CTRL to *ADA_ALL*, *ADA_15*, *ADA_24*, *ADA_33* and *ADA_42* experiments. Filled circles indicate the data assimilation boundaries where applicable.

The extratropical impact on tropical bias is also tested in two parallel sets of *ADA* and *ODA* experiments (Table 3.1), which are the same as the *CDA* experiments except that only observations of atmospheric temperature and wind (*ADA*) or SST (*ODA*) are

assimilated. Indeed, P_A and T_A from *ADA* and *ODA* experiments show similar dependence on the data assimilation boundary, albeit with slightly smaller changes than from *CDA* experiments (Figure 3.4a and b). The agreement between *ADA* and *CDA* experiments is expected. In *ADA*, the assimilation in the atmosphere component enables the atmosphere to force a realistic ocean even for short term climate variability: the correlation of monthly SST anomalies between model and the observation averaged in the region of data assimilation is 0.473 for *ADA_28*, similar to 0.507 as in *CDA_28* (Table 3.2). Besides, the atmosphere dynamics is directly responsible for producing precipitation in the model. Therefore, an *ADA* experiment should behave similarly to its *CDA* counterpart. On the other hand, the comparable extratropical impact of *ODA* and *ADA* experiments is surprising, because the extratropical ocean has little control on tropical interannual variability in the same model [Lu *et al.*, 2017b]. Physically, atmospheric variability in the extratropics is generated predominantly internally, rather than being forced by extratropical SST [Kushnir *et al.*, 2002]. In fact, *ODA* experiments poorly reproduce the observational atmospheric variability in the extratropics (Table 3.2). For example, the monthly surface zonal wind anomalies of *ODA_28* and observation have an average correlation of 0.002 in the assimilation region, compared to 0.750 in *CDA_28* and 0.752 in *ADA_28*. We speculate that the strong control of extratropical SST on tropical climatology could be caused by two reasons. The first reason is the surface ocean-atmosphere coupling through WES feedback as discussed before, which could be effective when the subtropical ocean is constrained by assimilation. The WES feedback process from SST assimilation in the *ODA* experiments may not be as strong or as fast as that from wind and air temperature assimilation in the *ADA* experiments to impact interannual variability like ENSO [Lu *et al.*, 2017b], but its long-term impact on tropical climatology

is significant. The second reason is the important role of ocean dynamics in the extratropical influence on tropical climatology. Because of the decadal or longer timescale for the ventilation through the subtropical cell [Liu *et al.*, 1994], the impact of extratropical oceans on the tropics is effective for climatological influence, but not for interannual variability. Indeed, *ODA_28* shows significant changes in the climatological subsurface temperature (Figure 3.6) and meridional oceanic energy transport in the tropics compared to *CTRL* (not shown), despite minimal impact on extratropical or tropical atmospheric variability.

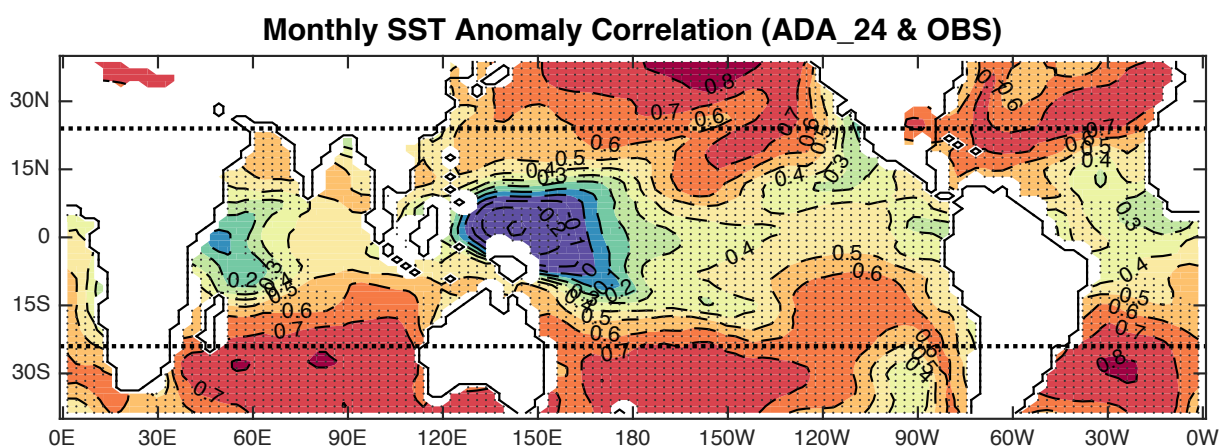


Figure 3.8 Same as Figure 3.5, but for *ADA_24*.

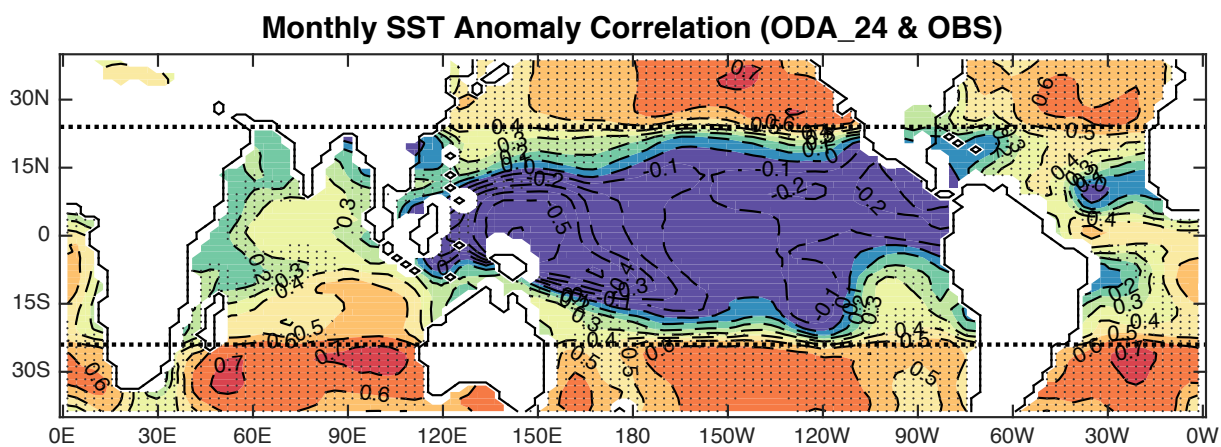


Figure 3.9 Same as Figure 3.5, but for *ODA_24*.

VARIABLE	SST	ATM T		ATM U		
REGION	28°S- 28°N	>28°N & <28°S	28°S- 28°N	>28°N & <28°S	28°S- 28°N	>28°N & <28°S
CTRL	0.127	-0.01	0.102	0.006	-0.007	-0.002
CDA_ALL	0.638	0.511	0.644	0.738	0.604	0.778
CDA_28	0.457	0.507	0.401	0.731	0.278	0.750
ADA_28	0.424	0.473	0.378	0.735	0.275	0.752
ODA_28	0.006	0.404	-0.038	0.136	0.024	0.002

Table 3.2 Correlation of anomalous monthly SST, surface air temperature and surface zonal wind between the model and the observation for *CTRL*, *CDA_ALL*, *CDA_28*, *ADA_28* and *ODA_28* averaged over 28°S-28°N and poleward of 28°S/28°N. (from [Lu *et al.*, 2017a])

Tropical bias in FOAM has a strong seasonal variance, leading to a seasonal extratropical impact (Figure 3.10). Both P_A and T_A of *CTRL* have the largest negative bias in boreal spring (March-April-May), followed by winter (December-January-February), indicating particularly warm and wet southern tropics in those seasons. Fittingly, boreal spring and winter are also the seasons when the biases of P_A and T_A are reduced the most by extratropical impact. In the boreal summer and fall, P_A and T_A of *CTRL* are much closer to observation, and the extratropical impact is not significant on P_A and T_A . The seasonal breakdown of P_A and T_A biases suggests that the improvement of tropical annual-mean climatology by extratropical data assimilation is achieved through the proper seasons.

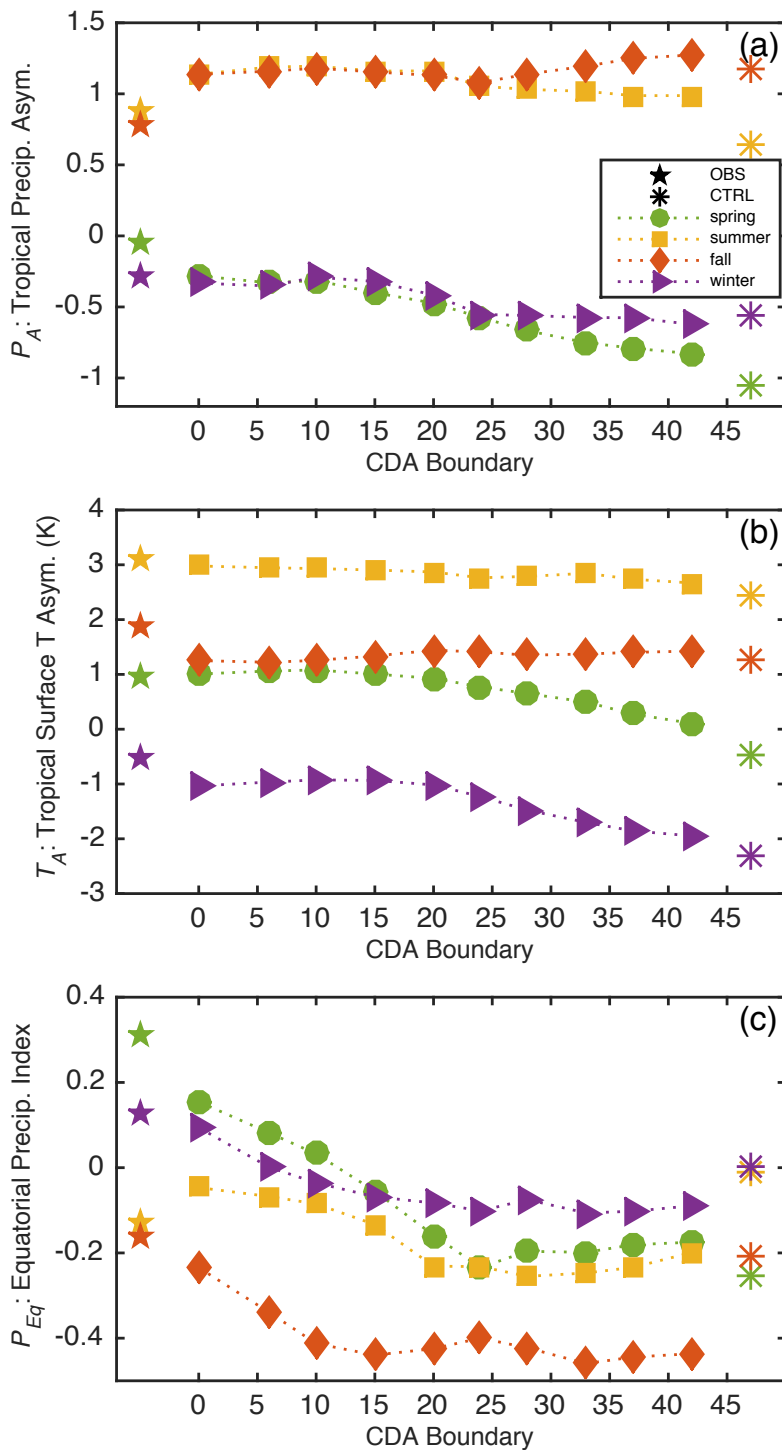


Figure 3.10 A summary of seasonal-mean climatological indices from observation (pentagon), FOAM control (asterisk), CDA (other markers) experiments. (a) Tropical precipitation asymmetry index P_A . (b) Tropical surface temperature asymmetry T_A . (c) Equatorial precipitation index P_{Eq} . (from [Lu et al., 2017a])

3.3. Equatorial Deficiency Bias of Precipitation

Besides excessive precipitation in the southern tropics, insufficient equatorial precipitation also contributes to the tropical bias of a double-ITCZ. The equatorial precipitation index P_{Eq} is used to evaluate the relative amount of tropical precipitation that falls within close proximity of the equator. P_{Eq} is defined as the area-averaged precipitation between 3°S and 3°N divided by that between 20°S and 20°N, then minus 1. Similar to most CMIP5 models [Adam et al., 2016], FOAM has insufficient equatorial precipitation ($P_{Eq} = 0.02$) compared to observation ($P_{Eq} = 0.13$). This equatorial insufficiency bias in P_{Eq} is again caused mainly by the spring season (Figure 3.10c) as in P_A .

In contrast to the tropical asymmetry bias, the equatorial insufficiency bias is improved primarily by local processes in the deep tropics instead of remote processes from the subtropics or extratropics. This can be seen in P_{Eq} across the RCDA experiments (Figure 3.4c). In CDA experiments, the deficient equatorial precipitation deteriorates, rather than improves, from CTRL to CDA_40 through CDA_15. The same deterioration also occurs in the ADA experiments, but much less severe in ODA experiments, reflecting the bias in the atmospheric dynamics-precipitation relationship in FOAM. P_{Eq} increases towards the observation only when the deep tropics is constrained by assimilation in CDA_10 through CDA_ALL. The different responses of P_A and P_{Eq} to the change in data assimilation domain suggest that the two aspects of the double-ITCZ bias could be caused by different model deficiencies. Remote extratropical forcing seems to have substantial impact on the tropical asymmetry bias (P_A) via extratropical-to-tropical teleconnections, while local tropical processes seem to control the equatorial insufficiency bias (P_{Eq}).

3.4. Energetic Analysis

The improvement of the tropical asymmetry bias and equatorial insufficiency bias in the RCDA experiments can be understood from the perspective of atmospheric energetics, as suggested by previous studies [Donohoe *et al.*, 2013; Hwang and Frierson, 2013; Bischoff and Schneider, 2014; Schneider *et al.*, 2014; Adam *et al.*, 2016]. As expected from the control of tropical SST on precipitation, the asymmetry indices P_A and T_A have a strong positive correlation across all RCDA experiments ($R = 0.912$, Figure 3.11a). Meanwhile, P_A is strongly and negatively correlated with the cross-equatorial atmospheric energy transport AET_{Eq} ($R = -0.913$, Figure 3.11b), which calculates the zonally- and vertically-integrated transport of moist static energy by the atmosphere model. The observed AET_{Eq} ranges from 0.1 PW to 0.2 PW southward in previous studies of observational data [Donohoe *et al.*, 2013; Hwang and Frierson, 2013; Adam *et al.*, 2016], and the value of 0.15 PW southward is used here [Adam *et al.*, 2016]. The implicit negative correlation between AET_{Eq} and T_A is easily deduced since the anomalous AET goes from the warming hemisphere into the cooling one. The correlation between P_A and AET_{Eq} here is stronger than previous studies [Hwang and Frierson, 2013; Adam *et al.*, 2016] since it is calculated for the same CGCM instead of across multiple models. In general, the more equatorward the data assimilation boundary is, the less biased P_A , T_A and AET_{Eq} are compared to *CTRL*.

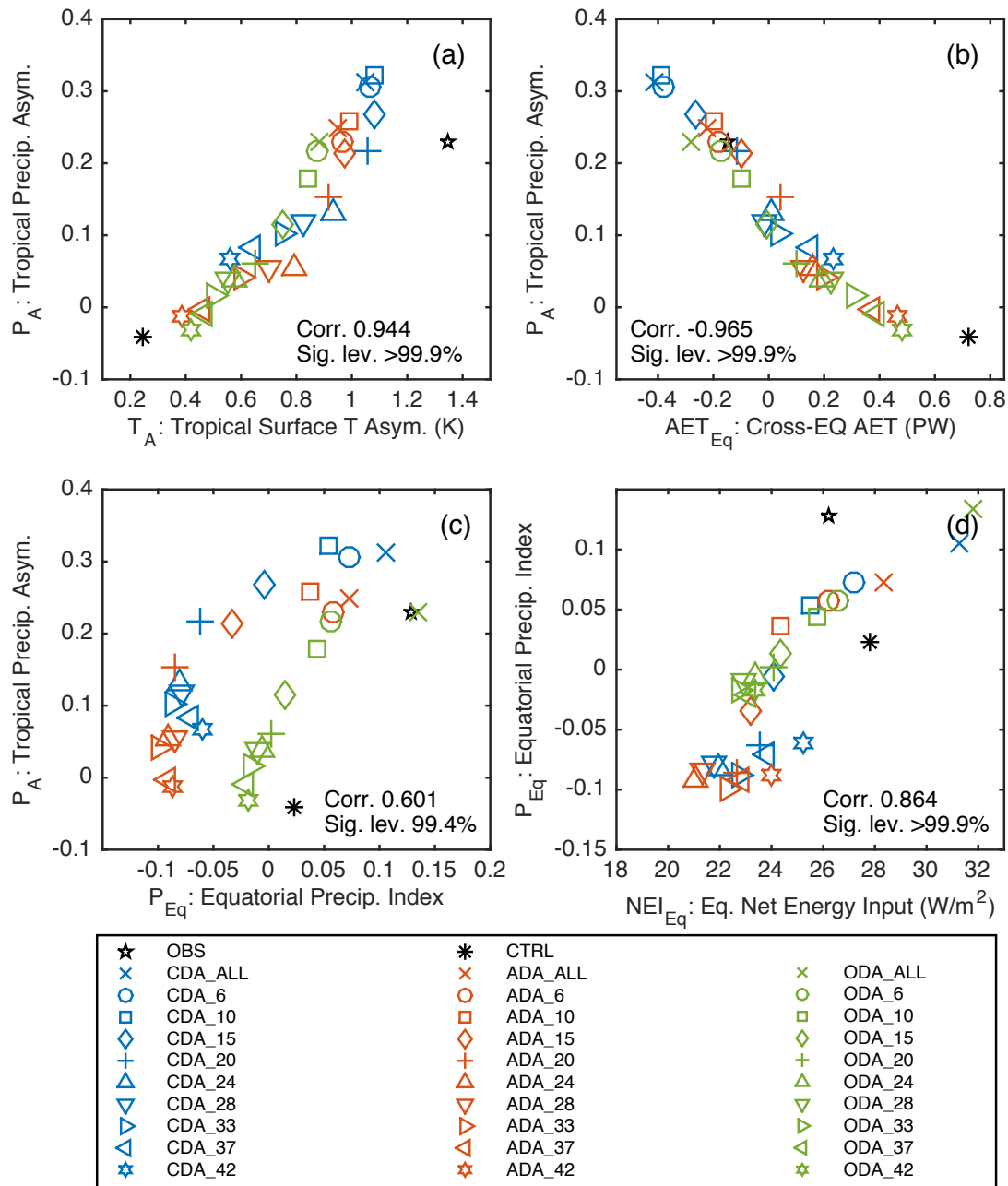


Figure 3.11 Scatterplots between indices for observation (pentagon), *CTRL* (asterisk), *CDA* (blue), *ADA* (red) and *ODA* experiments (green). (a) Tropical precipitation asymmetry P_A against tropical surface temperature asymmetry T_A . (b) P_A against cross-equatorial atmospheric energy transport AET_{Eq} . (c) P_A against equatorial precipitation index P_{Eq} . (d) P_{Eq} against equatorial net energy input NEI_{Eq} . (from [Lu et al., 2017a])

The correlation between P_A and P_{Eq} is not nearly as strong ($R = 0.508$) and much more scattered (Figure 3.11c), which again shows that P_A and P_{Eq} could be controlled by different mechanisms, at least in this model. The bias of insufficient tropical precipitation asymmetry (small or negative P_A) can be greatly improved by correcting extratropical large-scale dynamics toward observation, while the bias of insufficient equatorial precipitation (small or negative P_{Eq}) is only alleviated when the model is constrained by assimilation in the deep tropics. The local control of P_{Eq} is further shown by the high correlation between P_{Eq} and NEI_{Eq} for the RCDA experiments ($R = 0.847$, Figure 3.11d), as in CMIP5 models [Adam *et al.*, 2016]. NEI_{Eq} is the 5°S-5°N average of the atmospheric net energy input, calculated from top-of-atmosphere and surface net shortwave and longwave radiative fluxes, and sensible and latent heat fluxes at the surface. The observed NEI_{Eq} of 26.2 W/m² is used in this paper [Adam *et al.*, 2016]. It is notable that P_{Eq} of *CTRL* is much smaller than observation despite larger NEI_{Eq} . Only *CDA_ALL* and *ODA_ALL* have P_{Eq} close to observation, but NEI_{Eq} exceeds 30 W/m² in both experiments, far over the observed NEI_{Eq} . The fact that the observed $P_{Eq} - NEI_{Eq}$ relationship is more of an outlier among the RCDA experiments indicates flaws in FOAM's tropical precipitation schemes.

3.5. Summary and Discussion of Chapter 3

This chapter explicitly shows that the tropical bias in a coupled climate model can be reduced by extratropical coupled data assimilation. The model bias in tropical north-south precipitation asymmetry shows improvement when the data assimilation is only active poleward of 30° or even 40° in both hemispheres, and further improves as the assimilation expands equatorward into the tropics. When the model's extratropics are

constrained by observations, the extratropical-to-tropical teleconnection leads to not only higher north-south asymmetry in tropical precipitation, but also higher north-south asymmetry in tropical atmosphere surface temperature and more southward atmospheric energy transport across the equator. However, extratropical data assimilation cannot reduce the bias of insufficient equatorial precipitation in the model. The equatorial precipitation is closely related to the net energy input into the equatorial atmosphere, and the bias is only reduced when the data assimilation is active the deep tropics.

The coupled nature of the double-ITCZ bias is also studied here by activating the data assimilation in different model components. The double-ITCZ bias can be improved whether the key atmosphere variables or SST are corrected by assimilation. This is in complete contrast with the extratropical influence on the tropical interannual variability, which is dominated by extratropical atmosphere in this model [Lu *et al.*, 2017b]. The WES feedback seems to play a role in the extratropical influence on both tropical climatology and variability, while other mechanisms such as oceanic transport remain to be further explored with the RCDA method.

This study suggests that correcting FOAM's extratropical biases in variability and climatology toward the real world could reduce its tropical bias, especially the lack of precipitation and temperature asymmetry. Therefore, in the pursuit of eliminating the double-ITCZ bias in climate models, extratropical biases and extratropical-to-tropical teleconnection may require similar attention as tropical precipitation schemes and SST climatology. The RCDA could quantify the extratropical influence in climate models as in this study if such an appropriate data assimilation system is available.

It should also be pointed out that tropical bias in climate models is not limited to only precipitation bias or the double-ITCZ bias. The zonally heterogeneous aspect of the

tropical precipitation distribution is not explored in this study; neither are the Pacific cold tongue bias nor the influence of landmass. The model we use also have deficiencies such as the coarse resolution of the atmosphere component and the persistent biases even with data assimilation. The effects of these deficiencies could not be addressed in this study. It would greatly benefit our understanding and modeling of the tropical climate, particularly the double-ITCZ bias, to apply the RCDA method with higher-resolution state-of-the-art earth system models and more comprehensive coupled data assimilation systems.

Chapter 4

4. Extratropical Influence on Tropical Variability:

Perfect-model Study

As a pilot study, we will use RCDA to systematically investigate coupled model dynamics and teleconnections involved in the extratropical control of ENSO variability, first in the perfect-model framework. More specifically, active data assimilation of model-generated observations is performed in the extratropics and the forced climate variability in the tropics is studied. The use of model ensemble minimizes the noise from natural variability in the experiments. Chapter 4 shows that extratropical atmospheric variability in our CGCM can indeed exert significant control on ENSO and therefore serve as a precursor for ENSO onset. This part is organized as follows. Section 4.1 describes the model and methods. Section 4.2 includes a summary analysis of all RCDA experiments. Section 4.3 discusses the precursors and their implications.

4.1. Model and Methods

4.1.1. ENSO in FOAM

The current version of FOAM incorporates a parameterization of the solar penetration depth (SPD), which can influence the tropical climate [Lewis *et al.*, 1990; Schneider and Zhu, 1998; Murtugudde *et al.*, 2002]. FOAM simulates a reasonable tropical climatology, although the model still exhibits a tendency of strong Cold Tongue and double ITCZ (Figure 4.1a) as in most state-of-the-art CGCMs [Li and Xie, 2014]. The model equatorial eastern Pacific SST is also dominated by an annual cycle (not shown).

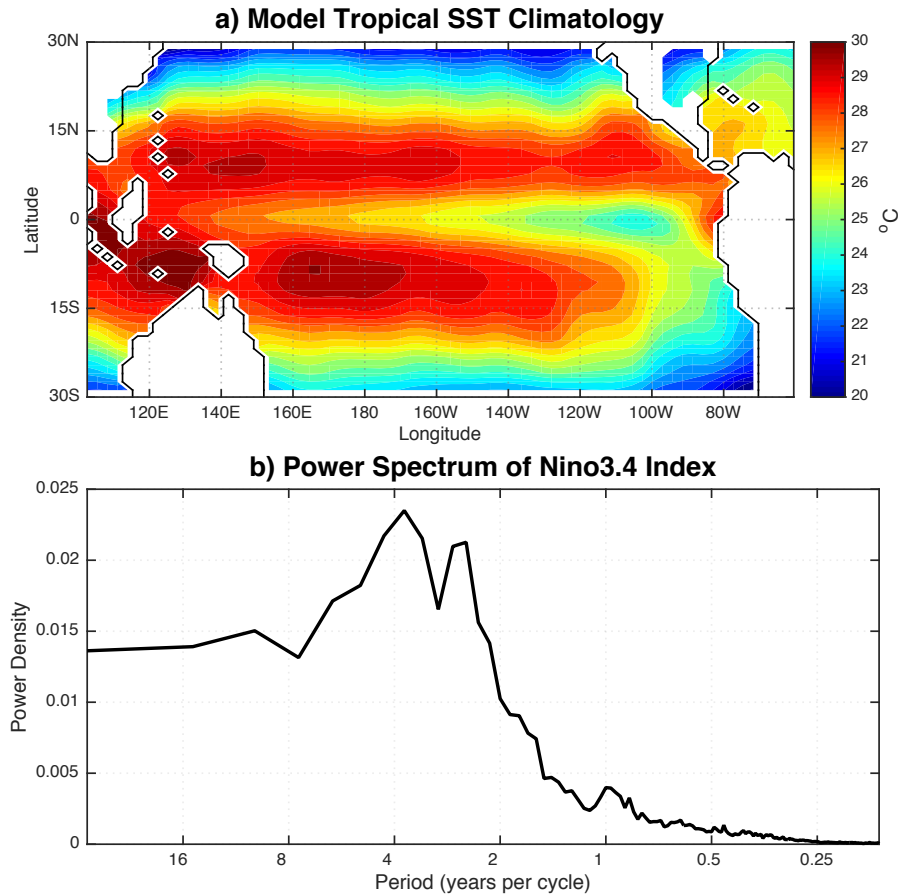


Figure 4.1 Annual-mean tropical SST climatology from a 500-year FOAM control simulation. (b) The power spectrum of the Nino3.4 index from the same 500-year FOAM control simulation. (from [Lu *et al.*, 2017b])

The model ENSO is dominated by variability with the frequency of 2-6 years, as shown by the power spectrum of the Nino3.4 index (average SST anomaly in the region of 5°S-5°N, 120°W-170°W) in Figure 4.1b, similar to previous work [Liu *et al.*, 2000]. The evolution of the equatorial (3°S-3°N meridional average) upper ocean temperature associated with ENSO can be seen in its regression on the normalized Nino3.4 index for different leads and lags (Figure 4.2). A weak subsurface warming develops in the western Pacific 12 months prior to the peak of ENSO (Figure 4.2a), expanding eastward along the thermocline and filling the entire equatorial upper Pacific with an anomalously high heat

content (Figure 4.2b); the eastern Pacific SST anomaly and therefore ENSO onset then starts to develop (Figure 4.2c), growing in amplitude (Figure 4.2d) and spread westward across the surface of equatorial Pacific (Figure 4.2e); in the meantime, a weak cooling develops in the subsurface western Pacific, grows in amplitude (Figure 4.2f) and spreads across the thermocline eastward (Figure 4.2g), leading to the following cold event of La Nina (Figure 4.2g, h, i), which resembles the preceding warm event (Figure 4.2a, b, c), albeit with a smaller amplitude and opposite sign. The similar patterns, but of opposite sign, between the 9-month lead (Figure 4.2b) and 9-month lag (Figure 4.2h) regressions imply a prevailing period of about 3 years. The oceanic process displayed in Figure 4.2, along with the active Bjerknes feedback (not shown), follows the classical delayed recharge oscillator theory [*Cane and Zebiak, 1985; Cane et al., 1986; Jin, 1997*].

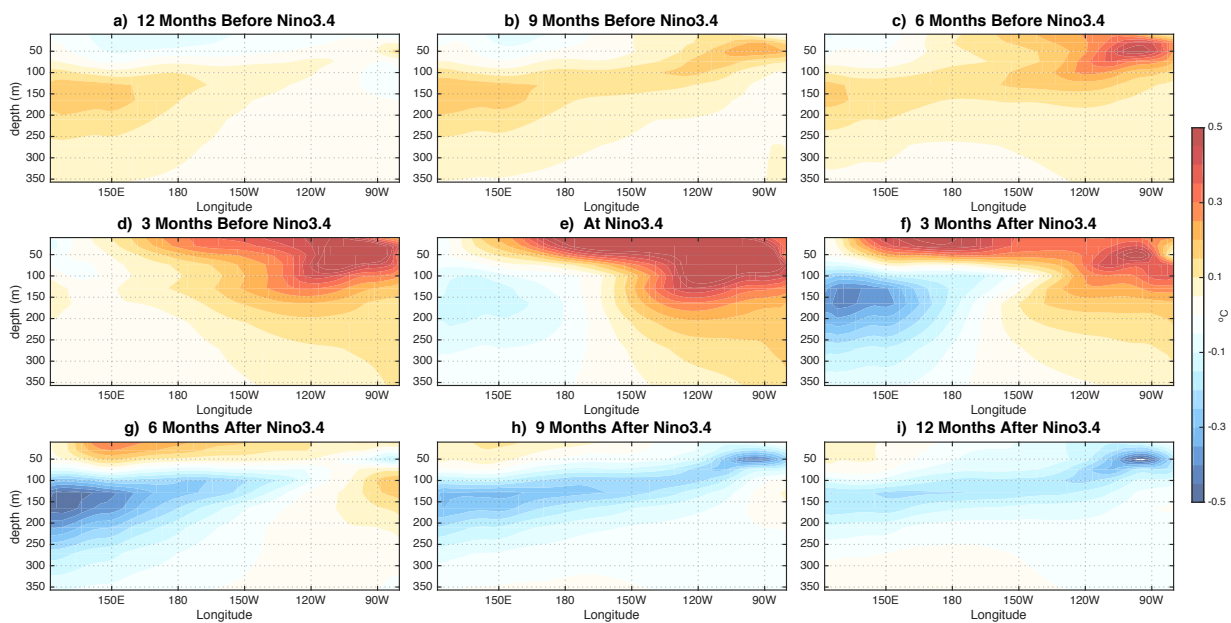


Figure 4.2 Regression of equatorial upper ocean temperature (3°S - 3°N meridional average) on normalized Nino3.4 index from the 500-year FOAM control simulation. The relative times between ocean temperature and Nino3.4 index are -12, -9, -6, -3, 0, 3, 6, 9 and 12 months (positive when Nino3.4 index leads) from left to right and top to bottom. (from [*Lu et al., 2017b*])

4.1.2. Experiment Design

Assimilation	Assimilated Latitudes	Experiment Name	RMSE of EnsMean Nino3.4	Ensemble Spread of Nino3.4	% of CTRL	
None	None	<i>CTRL</i>	0.641	0.637	100%	
	All	<i>ada_all</i>	0.114	0.085	17.8%	
	>10°N & <10°S	<i>ada_10</i>	0.206	0.169	32.2%	
	>20°N & <20°S	<i>ada_20</i>	0.366	0.309	57.0%	
	>30°N & <30°S	<i>ada_30</i>	0.439	0.384	68.4%	
	ADA	>20°N	<i>ada_north20</i>	0.558	0.533	87.0%
			<i>ada_north20A</i>	0.551	0.535	86.0%
		<20°S	<i>ada_south20</i>	0.517	0.506	80.7%
			<i>ada_south20A</i>	0.524	0.507	81.8%
		>30°N	<i>ada_north30</i>	0.581	0.542	90.6%
<30°S		<i>ada_south30</i>	0.600	0.605	93.5%	
ODA	All	<i>oda_all</i>	0.125	0.105	19.5%	
	>20°N & <20°S	<i>oda_20</i>	0.654	0.627	101.9%	
CDA	All	<i>cda_all</i>	0.119	0.041	18.5%	
	>20°N & <20°S	<i>cda_20</i>	0.347	0.319	54.1%	

Table 4.1 A summary of all experiments in [Lu et al., 2017b].

In this paper, we apply the RCDA method described in Section 2.4 to investigate the influence of extratropical climate variability on tropical Pacific climate variability with the focus on ENSO. In particular, we will focus on the forcing role of extratropical atmospheric variability on ENSO, so that most of our experiments apply only ADA in the

coupled model. The sole use of ADA ensures that the atmosphere is the only source of observational information, while the use of a coupled model provides the full ocean dynamics over the globe and fully coupled ocean-atmosphere dynamics both inside and outside the assimilation region. The major experiments consist of those with the ADA activated at all latitudes (*ada_all*), poleward of 20° in both hemispheres (*ada_20*), north of 20°N (*ada_north20*), and south of 20°S (*ada_south20*). These major experiments, along with other supplementary experiments, are summarized in Table 4.1: CTRL represents the ensemble control experiment without data assimilation; ADA (ODA) experiments employ only ADA (ODA) in the coupled model; CDA experiments employ both ADA and ODA simultaneously in the coupled model. For CDA and ODA, the assimilation is active either at all latitudes (*cda_all* and *oda_all*) or poleward of 20° (*cda_20* and *oda_20*) in both hemispheres. Besides, additional ADA experiments are performed with active ADA poleward of 10° (*ada_10*), 30° (*ada_30*) and 40° (*ada_40*) in both hemispheres, north of 30°N (*ada_north30*), or south of 30°S (*ada_south30*).

More specifics of the experiment design can be illustrated using the *ada_20* experiment as the example. The ADA is activated only in the extratropics (poleward of 20°) and therefore the atmosphere resembles closely to the observation in the extratropics. This observed atmospheric variability in the extratropics directly forces the underlying extratropical ocean via buoyancy, heat and momentum fluxes through the coupler, as well as the tropical climate system through atmospheric and coupled dynamics. In the tropics, the model is constrained along the boundaries at 20°S and 20°N in the atmosphere. Because the use of ensemble-based data assimilation, the model tropics are forced by slightly different extratropical variability in each ensemble member, so each model member's tropical coupled climate variability tends to develop differently due to

its chaotic natural variability. The averaged tropical variability of all ensemble members, however, can eliminate the influence of the chaotic natural variability, as later shown by the results of the CTRL experiment. Therefore, any tropical variability that is significant in the ensemble average should be generated by the common extratropical forcing to all ensemble members. The main difference between our approach and previous ensemble forecast experiments [Vimont *et al.*, 2009; Larson and Kirtman, 2014] is that the extratropical atmospheric variability, as well as its forcing on the ocean and the tropical atmosphere, are prescribed continuously as in the observation such that the coupled tropical climate variability is no longer a pure initial value ensemble forecast. Instead, our experiments represent the tropical climate variability forced by the observed extratropical atmospheric variability. Furthermore, EAKF should provide a more accurate analysis of the atmospheric/oceanic states in the assimilation region than, for example, a simple nudging scheme.

A perfect-model framework is adopted, and the output of a 50-year control simulation is used as the “truth”. The observations are constructed by adding Gaussian white noise onto the “truth”. The observations are therefore gridded data at the same gridpoints as the model state variables. The available observations include 5-day-mean SST with an error scale (standard deviation) of 0.5 K and daily-mean atmosphere temperature (T) and wind components (U, V) with error scales of 1 K and 1 m/s, respectively. These observational errors and frequencies represent typical conditions for such observed variables as in previous studies [Zhang *et al.*, 2007; Lu *et al.*, 2015b]. The details of the CDA is not critical for the purpose of this study, because the CDA is used only as a sophisticated way of “nudging” the model ensemble atmosphere towards the “observation”. Nevertheless, the CDA likely minimizes the shocks of “observational”

constraints and provides a more accurate reconstruction of atmospheric variability in the assimilation region. Furthermore, the ensemble aspect is of critical importance for the suppression of noise and the interpretation of the results.

Each experiment runs for 52 years, starting from an ensemble of initial conditions of 16 consecutive years within the long control simulation. The data assimilation is activated after 2 years of spin-up and lasts for 50 years, which is the length of the observation. The ensemble-mean output is calculated by averaging the monthly outputs from all ensemble members, and the anomalies of all variables are then calculated by subtracting the corresponding seasonal cycles. All experiments are repeated with different sets of initial conditions and observational errors, and the results are robust. Therefore, we will base our analysis on one set of experiments unless otherwise specified.

4.1.3. Performance of RCDA

Figure 4.3 displays the quality of the atmospheric (T and U) and oceanic (SST) analyses over the Pacific (120°E-80°W) for experiments *ada_all*, *ada_20*, *ada_north20* and *ada_south20*, all normalized by *CTRL*. The RMSE is calculated from the differences between monthly ensemble-mean analysis and the “truth” at each gridpoint, and Figure 4.3 shows the zonally-averaged RMSE. The quality of V analysis is quantitatively similar to T and U. When the ADA is employed across all latitudes (Figure 4.3a), the RMSE of both T and U are reduced by 70-80% across all latitudes and heights compared to *CTRL*. Because the analyzed atmosphere provides fairly accurate surface boundary condition to the ocean, the SST RMSE is also reduced by over 70% in the tropics and 40-60% in the mid-latitudes. When the ADA inside 20° is removed in *ada_20* (Figure 4.3b), the quality of analyses is largely maintained outside of 20°, but deteriorates rapidly from the 20° boundaries (dash-dot lines) equatorward. However, the tropical atmosphere and SST are

still partially constrained because of the accurate boundary conditions provided by ADA at 20° . In the deep tropics, RMSE of T, U and SST are still 30-40% smaller than *CTRL*. Similarly, for *ada_north20* (Figure 4.3c) and *ada_south20* (Figure 4.3d), the analyses are well constrained where assimilation is active, and deteriorates rapidly beyond the assimilation boundaries. The RMSE ratio of SST is essentially the same as that of the atmospheric surface temperature in Figure 4.3. The ADA outside of 20° in one hemisphere could affect the equatorial region, but shows little influence on the other hemisphere, where the RMSE remains the same as *CTRL*.

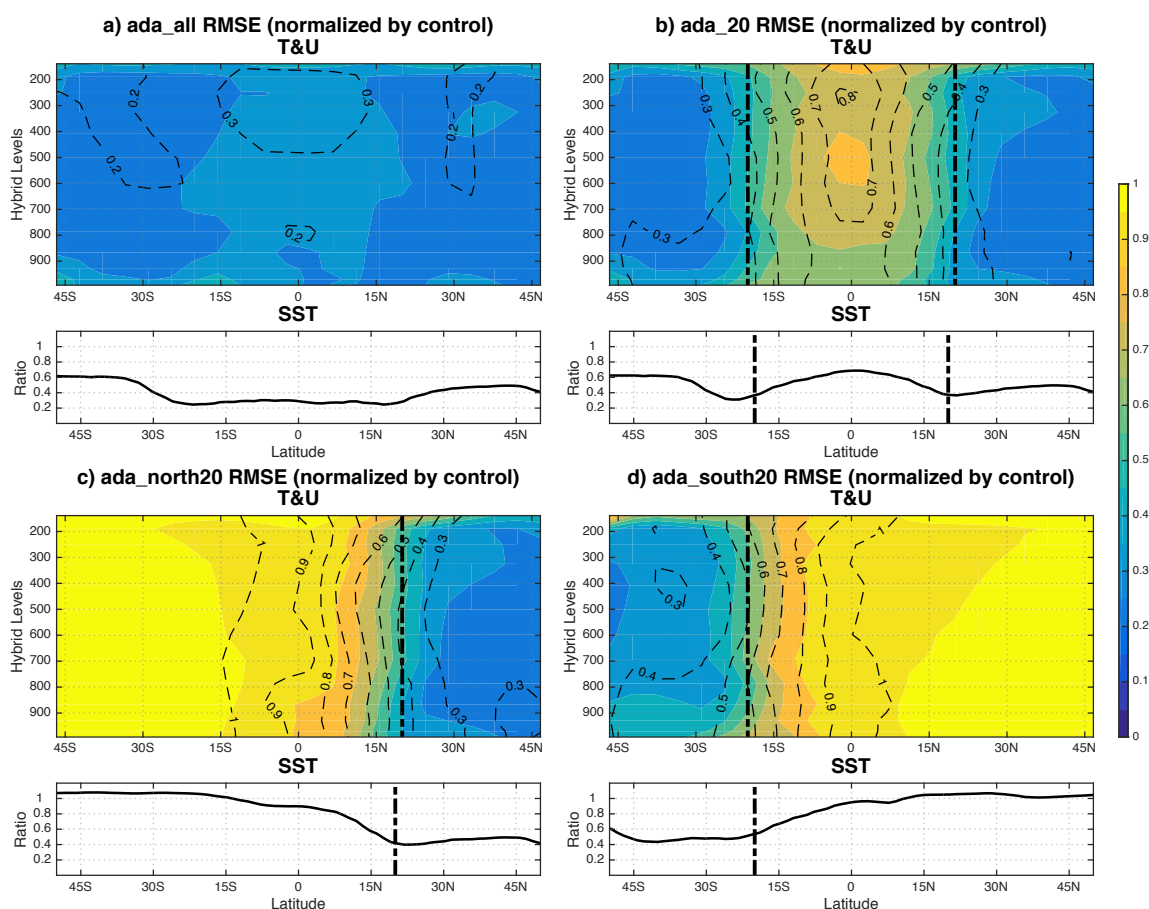


Figure 4.3 Pacific (120°E-80°W) zonal-mean RMSE (normalized by *CTRL*) of ensemble-mean atmospheric temperature (shadings), zonal wind (dashed lines) and SST (lower panel) for (a) *ada_all*, (b) *ada_20*, (c) *ada_north20*, and (d) *ada_south20*. The thick dash-dot lines indicate the boundaries of data assimilation where necessary. (from [Lu et al., 2017b])

4.2. Overview of Results

4.2.1. General Assessment

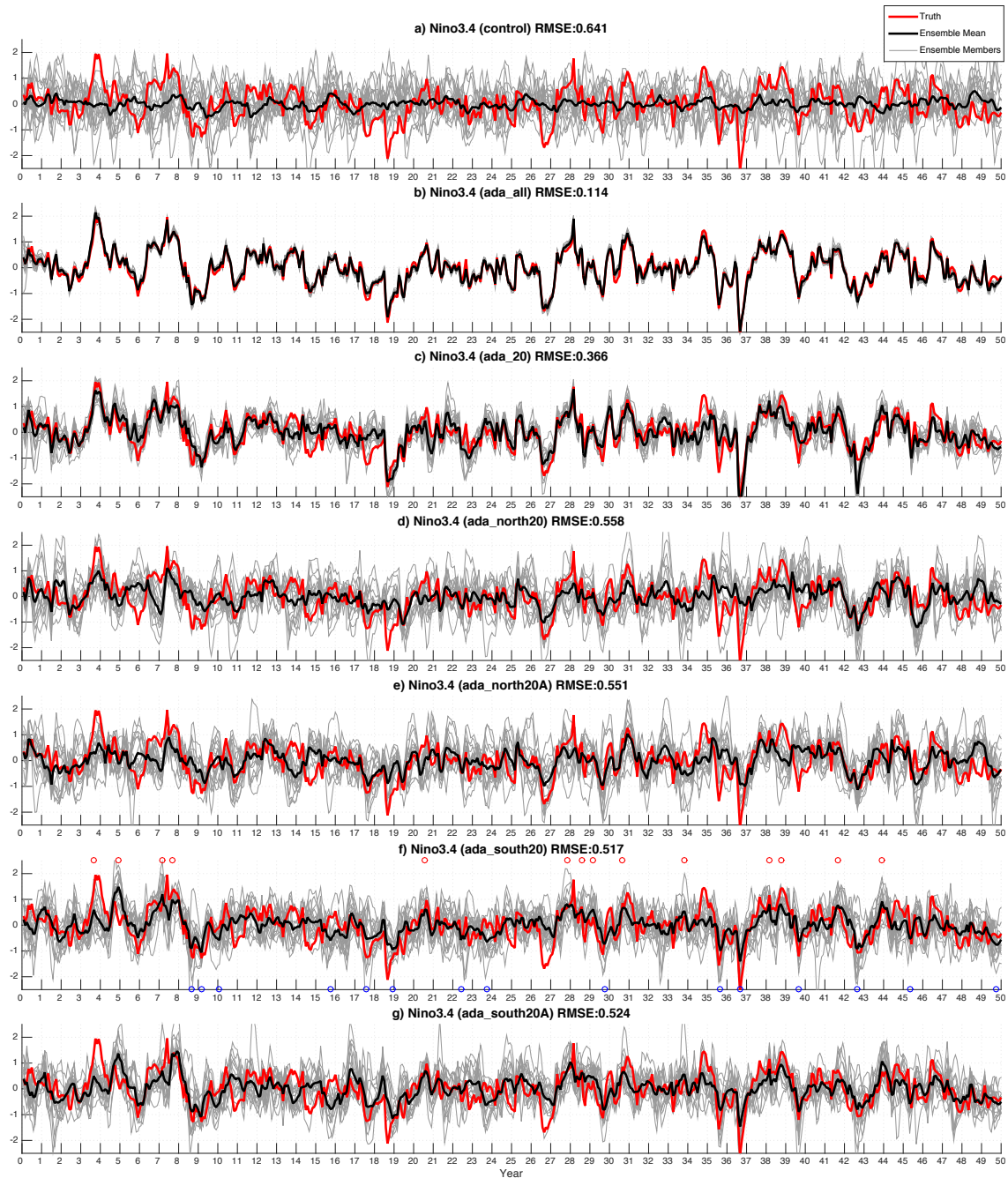


Figure 4.4 The time series of Nino3.4 index from (a) *CTRL*, (b) *ada_all*, (c) *ada_20*, (d) *ada_north20*, (e) *ada_north20A*, (f) *ada_south20*, and (g) *ada_south20A*. Red lines indicate the “truth” (same for all panels), black lines the ensemble mean, and grey lines all 16 ensemble members. (from [Lu et al., 2017b])

Overall, our experiments show a significant control of extratropical atmospheric variability on ENSO. Table 4.1 summarizes all experiments' ability to reproduce the "true" ENSO variability by showing the RMSE of their ensemble-mean Nino3.4 indices in regards to the "true" Nino3.4 index. The ensemble spread of the Nino3.4 indices and the RMSE as a percentage of that of *CTRL* are also shown for each experiment. The ensemble spread represents the uncertainty in the Nino3.4 indices of the model ensemble, and is comparable to the corresponding RMSE, which is usually the case for a well-behaved CDA system in the perfect model framework [Anderson, 2001; Zhang et al., 2007]. Figure 4.4 shows the Nino3.4 time series of several experiments (*CTRL*, *ada_all*, *ada_20*, *ada_north20*, *ada_north20A*, *ada_south20*, and *ada_south20A*), including those of each ensemble member, the ensemble mean and the "truth".

The RMSE of 0.617 in *CTRL* is very close to the standard deviation of the "true" Nino3.4 index because the ensemble average of 16 control simulations stays close to 0 at all times (Figure 4.4a). Even though each ensemble member has its own natural variability, the ensemble mean is affected little by the variability of any single member.

Nino3.4 index closely resembles the "truth" when ODA is active in the tropics. This should be expected since the tropical SST is directly adjusted by observations in *oda_all*. Meanwhile, extratropical ODA has no effect on Nino3.4, as the RMSE of *oda_20* is comparable to that of *CTRL*. It should be noted that *oda_20* only assimilates SST observations poleward of 20°. The failure of *oda_20* to reproduce the tropical variability in the observation implies the ineffectiveness of extratropical SST variability alone in forcing tropical climate variability.

Among the *ada* experiments, the RMSE increases, as expected, when the boundaries of active ADA move poleward. However, extratropical ADA shows significant influence

on ENSO variability, reducing the RMSE of Nino3.4 by over 40% in *ada_20* and over 30% in *ada_30* compared to *CTRL*. The *ada_all* experiment, in which the ocean is forced by close-to-observation atmosphere at all latitudes, could accurately reproduce the “true” Nino3.4 index with minimal ensemble spread (Figure 4.4b). The *ada_20* experiment produces both larger RMSE and ensemble spread compared to *ada_all*, but its ensemble-mean output still captures most of the major ENSO events in the “truth” (Figure 4.4c). The fact that most ENSO events in *ada_20* are significant among all ensemble members indicates that extratropical atmosphere alone could generate consistent ENSO signals.

When the ADA is limited to only one hemisphere, the resulting Nino3.4 variability is significantly worse than when ADA is active in both hemispheres with the same latitude boundary (87.0% and 80.7% vs. 57.0% for 20° cases). As shown by Figure 4.4d and f, not only are much fewer ENSO events correctly produced in *ada_south20* and *ada_north20*, the ensemble-mean magnitudes are also much smaller, and the ensemble spread much larger.

The ENSO variability in *ada_south20* and *ada_north20* is indeed forced by the extratropical atmosphere, confirmed by parallel experiments *ada_north20A* and *ada_south20A* (Table 4.1 and Figure 4.4), which are the same as *ada_north20* and *ada_south20*, respectively, except for different initial conditions and random observational errors. Each pair of experiments (e.g. *ada_north20* and *ada_north20A*) have almost identical RMSE of Nino3.4 indices and reproduce the ENSO events at roughly the same times and with similar magnitudes.

The results in Table 4.1, along with Figure 4.4, clearly demonstrate that the extratropical atmosphere has significant impact on ENSO variability. Figure 4.4 also shows the necessity of using ensemble. For *ada_north20* and *ada_south20*, or even some

ENSO events in *ada_20*, the Nino3.4 index differs greatly among ensemble members. Due to the chaotic natural variability, each individual member often fails to capture the “true” ENSO events, while also generates erroneous events that do not exist in the “truth”. Clearly, the impact of natural variability is minimized by taking the ensemble average from the CDA scheme, as shown by the near-zero Nino3.4 index of the *CTRL* experiment.

We note that the *CTRL* experiment can be used conveniently as a benchmark to evaluate the significance of other experiments. For every variable, the distribution of its ensemble-mean anomaly from *CTRL* specifies the magnitude of its natural variability without any input observations. In the following sections, the standard deviations of the ensemble-mean anomalies from *CTRL* (*CTRL_SD* hereafter) will be used to evaluate the significance of all variables. For example, the Nino3.4 index of *CTRL* has a standard deviation of 0.17°C and a maximum value of 0.55°C . In fact, there are only two instances when the Nino3.4 index exceeds 0.5°C over the 50 years of *CTRL*, and each lasts only one month. This means that the ensemble-mean ENSO events in *ada_20*, *ada_north20* or *ada_south20* that exceed peak Nino3.4 value of 0.5°C are very unlikely to be caused by natural variability. Rather, they are caused by the assimilation of extratropical atmospheric observations, which provides the same signal across all ensemble members. Therefore for the analysis of *ada_south20*, an ENSO event is counted everytime the monthly Nino3.4 index exceeds 0.5°C , regardless of the duration. A different criterion like Nino3.4 over 0.4°C for at least 3 consecutive months gives almost the same events. The ENSO events in *ada_south20* are identified with lower SST threshold and shorter duration compared to observational standard because first, the overall weaker ENSO variability in FOAM (Nino3.4 standard deviation 0.65°C) than in observation (around 1.0°C), and second, the even weaker ENSO variability of *ada_south20* than the “truth”

due to ensemble averaging. The identified ENSO events in *ada_south20* are indicated by the red (El Niño) and blue (La Nina) circles in Figure 4.4f. Note that there are a few instances where two ENSO events are very close to each other. Because the weak phase-locking of ENSO events to the seasonal cycle, we will keep the identified events that have peak values less than 1 year but more than 6 months apart from each other.

4.2.2. Extratropical Control on ENSO

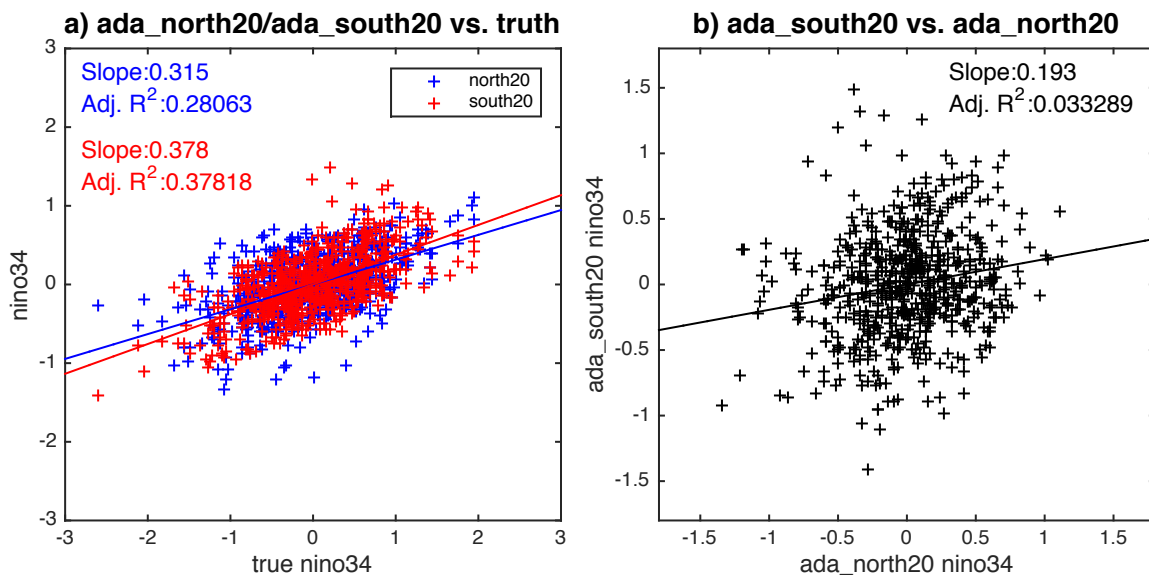


Figure 4.5 Scatter plots with linear regression slope coefficient and adjusted R² for the Nino3.4 indices of (a) *ada_north20* (blue) and *ada_south20* (red) vs. truth, (b) *ada_south20* vs. *ada_north20*. (from [Lu et al., 2017b])

Now, we examine the control of extratropical atmosphere on ENSO variability in detail with the focus on the three main experiments, *ada_20*, *ada_south20* and *ada_north20*. First, the extratropical atmospheric variability from both hemispheres can generate most of the “true” ENSO variability, while that from each hemisphere generates less. In Figure 4.4d and f, although both *ada_north20* and *ada_south20* could reproduce some of the ENSO events from the "truth", the magnitudes are mostly smaller than the "truth" or *ada_20*, and the overall variances of the Nino3.4 indices are also smaller. These

features are displayed more clearly in Figure 4.5a, where the Nino3.4 indices of *ada_north20* (blue) and *ada_south20* (red) are scattered against the “truth”. The markers are less scattered vertically than horizontally, indicating smaller variances of Nino3.4 in *ada_north20* and *ada_south20* than the “truth”. More specifically, the standard deviation of the Nino3.4 index is 0.63 for the "truth", 0.58 for *ada_20*, 0.39 for *ada_north20*, and 0.44 for *ada_south20*.

Although *ada_north20* and *ada_south20* each inherits, in a statistical sense, about half of the Nino3.4 variance from *ada_20*, the relationship among *ada_20*, *ada_north20* and *ada_south20* for individual ENSO events is complicated, as seen in the time series of Figure 4.4c, d and f. Some events in *ada_20* are produced in *ada_north20*, but not in *ada_south20* (around year 11, 27, 42); some are the opposite, produced in *ada_south20* but not in *ada_north20* (around year 5, 9, 36); some are partially produced in both *ada_north20* and *ada_south20*, but in smaller magnitudes (around year 4, 19). Overall *ada_north20* and *ada_south20* are reproducing mostly different ENSO events, indicating independent forcing from NH and SH. The independence of NH and SH extratropical control is supported by the plot between the Nino3.4 indices of *ada_north20* and *ada_south20* in Figure 4.5b, which has a weak correlation of 0.193 but an adjusted R^2 of only 0.033. Therefore, in the following sections, we will analyze *ada_north20* and *ada_south20* separately to better understand the role of extratropical atmospheric forcing on ENSO. Interestingly, the sum of the Nino3.4 indices of *ada_north20* and *ada_south20* closely resembles that of *ada_20* with a correlation of 0.81, and the standard deviation of the sum is 0.61.

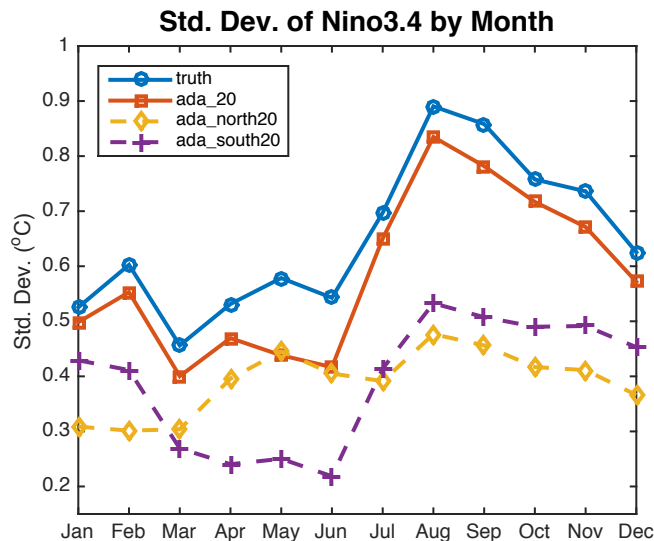


Figure 4.6 Standard deviations of the Nino3.4 index by calendar month from the *truth*, *ada_20*, *ada_north20* and *ada_south20*. (from [Lu et al., 2017b])

The extratropical control of ENSO and the comparable contribution from NH and SH can also be seen in the seasonality of ENSO. The phase-locking of ENSO variability with the seasonal cycle is another important feature of the observed ENSO variability, which has not been fully understood. Figure 4.6 plots the standard deviations by calendar month of the Nino3.4 indices from “*truth*”, *ada_20*, *ada_north20* and *ada_south20*. The seasonality of Nino3.4 variability in *ada_20* is similar to the observation, albeit slightly smaller in magnitude for all months. The peak variance of the Nino3.4 index occurs in August and September, followed by October and November, which is shifted early to boreal fall from the boreal winter in the real world. In the single-hemisphere forcing experiments, the overall variance decreases significantly and the seasonality changes. Relatively speaking, there are higher spring variability (April to June) in *ada_north20* and lower spring variability in *ada_south20*. These changes of seasonality should be related to their respective extratropical atmospheric forcing and will be discussed in the following sections.

4.3. ENSO Precursors

Now, we examine in detail the extratropical control of ENSO, with the emphasis on the precursors for ENSO events. We will focus on the SH forcing in *ada_south20*, because the NH influence can be discussed in a similar fashion. We first discuss the potential precursors in equatorial heat content and extratropical atmosphere based on the composite of ENSO events. We will then examine if each potential precursor is sufficient to trigger ENSO on its own based on the composite of anomalous events on each precursor. Finally, we will discuss a potentially necessary and sufficient precursor by combining the heat content and extratropical atmosphere precursors together.

4.3.1. ENSO Composites and Potential Precursors

ENSO evolution and its potential precursors of ENSO in *ada_south20* can be seen in the composite of ENSO events in Figure 4.7, which shows the composite of the Nino3.4 index (Figure 4.7a), the zonal propagation of equatorial (5°S - 5°N meridional average) Pacific SST (Figure 4.7b) for the 29 ENSO events in *ada_south20* (La Nina events are included with reversed sign). These ENSO events, as indicated by the circles in Figure 4.4f, have peak Nino3.4 magnitudes that exceed 0.5°C , which is very close to the maximum value (0.55°C) and 3 times the standard deviation (0.17°C , black dashed lines in Figure 4.7a) of the Nino3.4 index from CTRL. In other words, all these ENSO events in *ada_south20* are very unlikely to occur due to natural variability without the assimilated extratropical observations. The Nino3.4 composite shows a warming that starts 6-7 months prior to the peak, rises rapidly 2 months prior to the peak, and slowly decays afterwards over a span of 10 months. Although there is no obvious cycle, the Nino3.4 composite is slightly negative 1-2 years prior and after the peak, indicating the succession between warm and cold events. Figure 4.7b shows that the SST anomalies originate

mostly from the eastern equatorial Pacific, and propagate westward from 100°W to the dateline in 3-4 months. In sum, the composite ENSO events in Figure 4.7 are highly significant compared to CTRL, indicating a robust tropical response to SH extratropical atmospheric forcing.

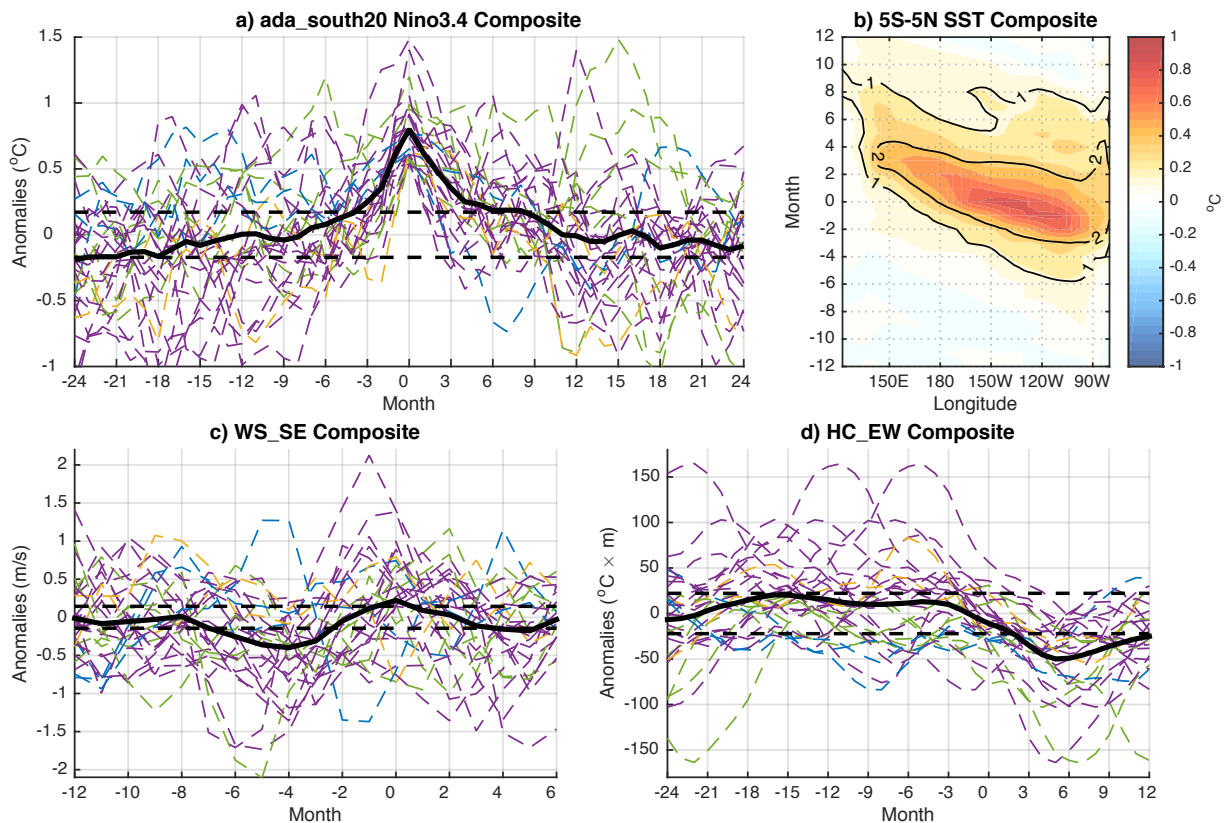
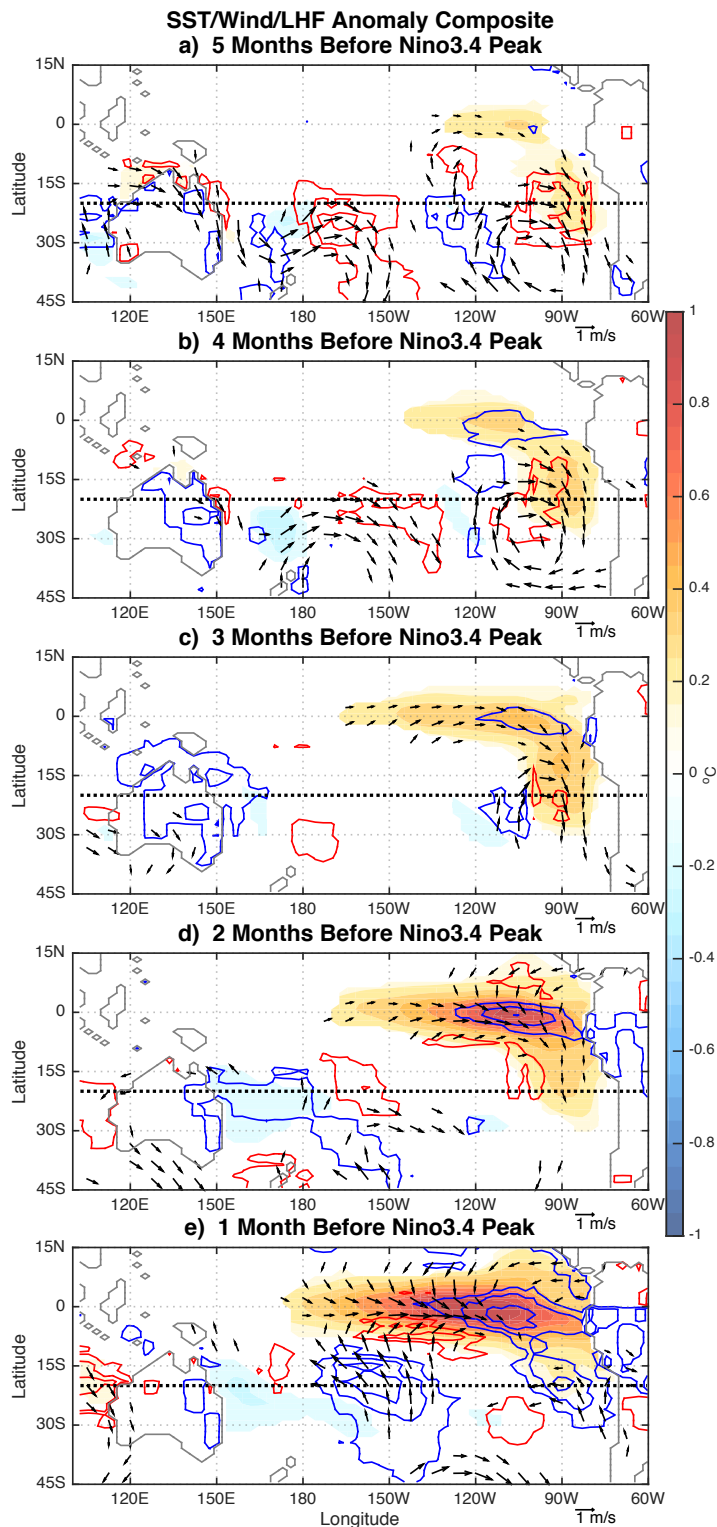


Figure 4.7 For *ada_south20*: (a) Composite of Nino3.4 index of 29 ENSO events exceeding 0.5°C. La Nina events are included with reversed sign. Dashed lines indicate CTRL_SD, the standard deviations of the ensemble-mean anomalies from CTRL. (b) Composite of 5°S-5°N averaged Pacific SST based on the Nino3.4 peaks (shadings) and its ratio to the corresponding CTRL_SD (contours). (c) Same as Figure 4.7a but for WS_SE. (d) Same as Figure 4.7a but for HC_EW. (from [Lu et al., 2017b])

Next we examine the evolution of surface (Figure 4.8) and subsurface (Figure 4.9) conditions prior to the ENSO events in *ada_south20*. Composites of SST, low-level wind, and latent heat flux (LHF hereafter) anomalies are created in the equatorial and south Pacific for the 5 months prior to the Nino3.4 peak in *ada_south20* (Figure 4.8). The low-

level wind is averaged over the bottom 3 levels ($>900\text{mb}$). Positive LHF anomaly (blue contours) indicates more LHF out of the ocean or a cooling effect on the ocean. The SST and wind anomalies are only visible where they exceed their CTRL_SD. The NH extratropics is excluded from Figure 4.8 because no robust ensemble-mean signals exist there for any variable. Only the atmospheric (T, U, V) observations south of 20°S are assimilated, so any robust signals in the ensemble-mean anomalies of *ada_south20* should be attributed, ultimately, to SH extratropical atmospheric variability.

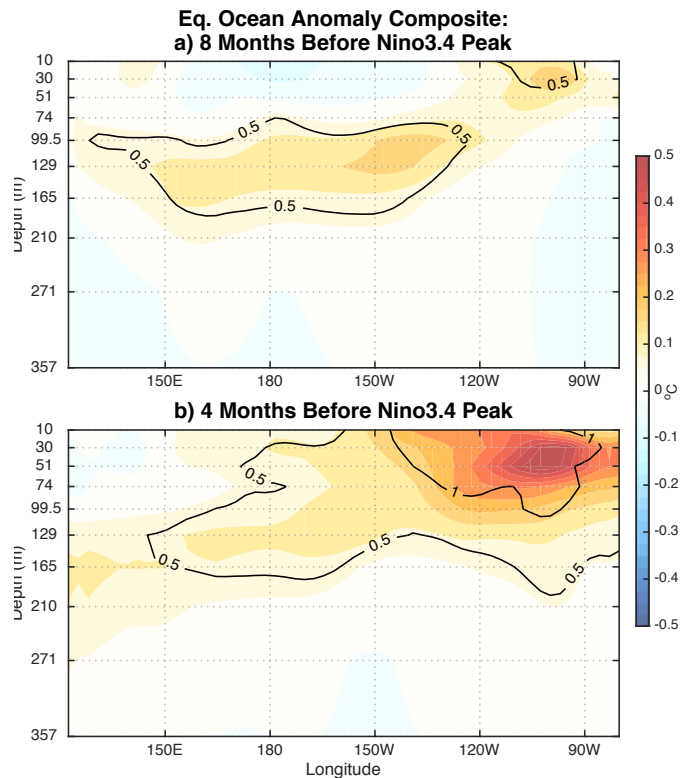
Figure 4.8 Composites of anomalous SST (shadings, K), LHF (contours, 4 W/m^2 intervals and zero line omitted) and wind (arrows) for the 5 months prior to the peak of the Nino3.4 composite in *ada_south20*. Blue (red) contours indicate more (less) upward LHF. Black dotted lines indicate the boundary of data assimilation. SST and wind anomalies are only shown where the composite exceed CTRL_SD. (from [Lu et al., 2017b])



The propagation of SH extratropical variability into the equatorial Pacific preceding ENSO in *ada_south20* resembles the SPMM described in [Zhang *et al.*, 2014]. At 5 months prior to the Nino3.4 peak (Figure 4.8 a), there is already positive SST anomaly in the eastern equatorial Pacific. Meanwhile, a low-pressure system centers at 40°S, 100°W as in the observation. The anomalous northwesterly to the northeast of the low-pressure center reduces the climatological southeasterly trade winds and, in turn, the LHF out of the ocean. One month later (Figure 4.8 b), the low-pressure center moves equatorward to 30°S, 100°W with the wind anomalies intensified. The wind anomalies that extend beyond the assimilation region to north of 20°S, where the atmosphere and ocean are fully coupled and active, could be caused by atmospheric dynamic adjustment [Pierce *et al.*, 2000]. Furthermore, the reduced LHF cooling continues to warm the SST in the southeast subtropical Pacific. This subtropical warming differs from the simultaneous equatorial warming in that the LHF anomaly tends to intensify, instead of damp, the SST anomaly in the former. As such, the coupled wind-SST anomaly can propagate equatorward through the WES feedback as suggested by [Liu and Xie, 1994]. The warm SST anomaly would induce anomalous westerlies on the equatorial side, which further reduces the mean easterly trade wind and LHF there, allowing the coupled anomaly to propagate equatorward. In the following 2 months (Figure 4.8 c, d), the subtropical SST anomaly moves from 20°S to 10-15°S and becomes connected to the pre-existing equatorial SST anomaly. The anomalous northwesterly still persists in the eastern equatorial and southeast tropical Pacific. Meanwhile, anomalous westerly wind expands westward and intensifies along the equator from 100°W all the way to 160°W. In the following month (Figure 4.8 e), the SST and wind anomalies start to move off the coast.

In the meantime, the off-equator northerly wind anomalies in southeast Pacific have mostly reversed to southerly, and the LHF anomalies have changed sign to positive across the entire tropical and subtropical eastern Pacific. Overall, the subtropics-to-tropics process in Figure 4.8 is similar to the SPMM process found in CMIP3 (Coupled Model Intercomparison Project phase 3) AGCM-slab ocean and fully coupled models, as well as in the real world [Zhang *et al.*, 2014].

Figure 4.9 Composite of anomalous 3°S-3°N averaged Pacific upper ocean temperature (a) 8 months and (b) 4 months prior to the peak of the Nino3.4 composite in *ada_south20*. The contours indicate the ratios of the composite anomalies to CTRL_SD. (from [Lu *et al.*, 2017b])



The accompanied evolution of the equatorial (3°S-3°N average) upper ocean temperature can be seen for 8 and 4 months prior to the Nino3.4 peak in the composite of Figure 4.9. There is significant subsurface warming before the ENSO events in *ada_south20*, like the regressed upper ocean temperature evolution of the 500-year control simulation in Figure 4.2 (thus only two snapshots in Figure 4.9). Both Figure 4.2 and Figure 4.9 show an eastward and upward propagation and the subsequent ENSO onset in the eastern equatorial Pacific.

Based on Figure 4.2 and Figure 4.9, we use the heat content anomaly in the equatorial western Pacific as the subsurface precursor for ENSO, with the heat content anomaly

(HC_EW hereafter) calculated as the 3-month running-averaged anomalous temperature integrated in the western equatorial Pacific (3°S - 3°N , 120°E - 180° , 40-240m). We will also use the 3-month running-averaged low-level wind speed anomaly (WS_SE hereafter) in the southeast subtropical Pacific (15°S - 25°S , 80°W - 100°W , bottom 3 levels) as the extratropical atmospheric precursor. We use wind speed instead of sea level pressure [Anderson, 2007; Deser *et al.*, 2012] or SST [Zhang *et al.*, 2014] because wind is directly constrained by the ADA in our experiments and better represents the prescribed extratropical atmospheric variability due to assimilation. As shown in Figure 4.8, the anomalous wind speed in this region is the largest 3-5 months prior to the Nino3.4 peak and leads to reduced LHF cooling, SST warming and subsequent WES propagation.

The composites of WS_SE and HC_EW series based on the 29 ENSO events in Figure 4.7a are plotted in Figure 4.7c and Figure 4.7d, respectively. The WS_SE composite shows significant negative values 3-5 months prior to the Nino3.4 peak, where it exceeds twice its CTRL_SD. There is also a sign change for WS_SE right before the Nino3.4 peak, consistent with the reversal of trade wind anomalies after the ENSO onset in Figure 4.8e. The HC_EW composite shows consistently positive values in the 1.5 years leading to the Nino3.4 peak and significant negative values after the Nino3.4 peak. The peak value of HC_EW composite preceding ENSO is not as significant as WS_SE, mainly because the time between HC_EW and Nino3.4 peaks varies greatly among ENSO events. Based on the preceding WS_SE and HC_EW, the 29 individual events in Figure 4.7 are color coded as follows: 18 “purple” events when any negative WS_SE value exceeds its CTRL_SD in the range of 3-5 months prior to Nino3.4 peak *AND* any positive HC_EW value exceeds its CTRL_SD in the range of 6-18 months prior to Nino3.4 peak; 6 “green “ events when *only* the WS_SE criterion is met; 2 “yellow” events when *only* the HC_EW criterion is

met; and 3 “blue” events when *neither* criterion is met. In sum, most of the ENSO events are preceded by significant anomalies in the wind and heat content precursors, given our wide range of leading times.

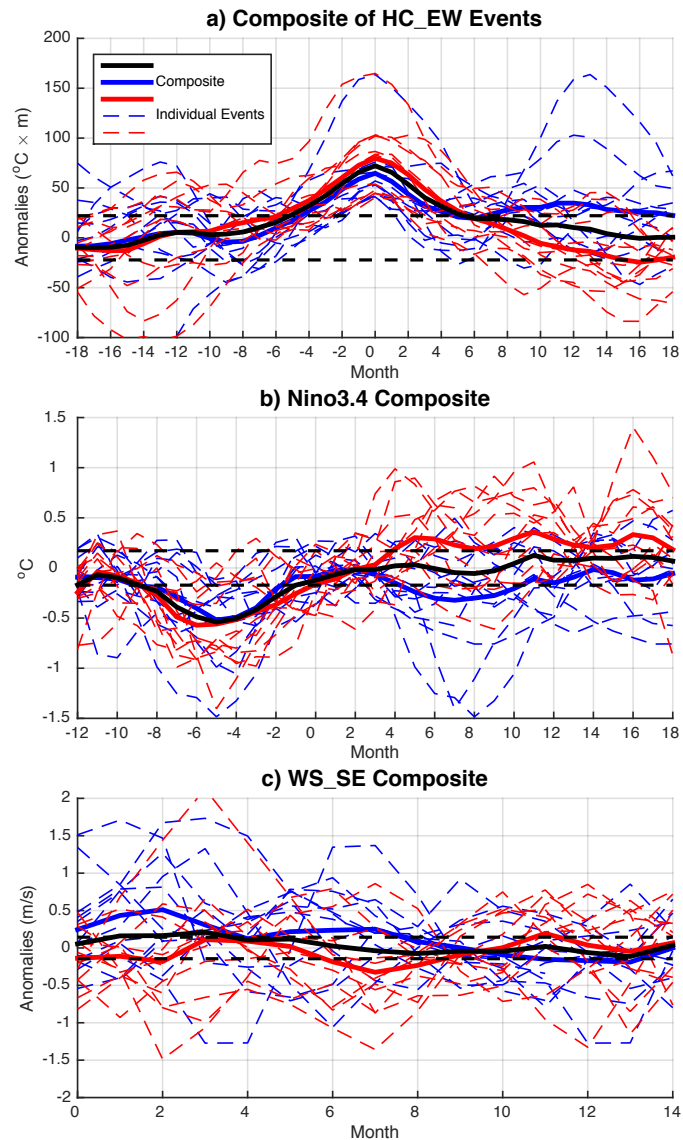
Figure 4.7, Figure 4.8 and Figure 4.9 together confirm that ENSO events in *ada_south20* are preceded by significant anomalous signals, or precursors, in both SH extratropical atmosphere/ocean and equatorial subsurface ocean. This is consistent with previous observational and modeling analyses, which showed that both the forcing of extratropical atmospheric variability and the preconditioning of the equatorial ocean heat content could play critical roles in the ENSO onset [Anderson, 2007; Vimont et al., 2009; Zhang et al., 2009; Deser et al., 2012; Larson and Kirtman, 2013, 2014]. As pointed out by [Larson and Kirtman, 2014], however, this type of composite analysis is based on subsampling only the years with ENSO events, therefore the identified precursors, such as WS_SE and HC_EW here, are potentially necessary precursors, but may be insufficient to trigger ENSO in the forecast sense or even produce false alarms. In the following, we further determine the necessity and sufficiency of either precursor, the anomalous equatorial heat content or extratropical atmosphere, for triggering ENSO events in the *ada_south20* experiment.

4.3.2. Equatorial Oceanic Precursor

To focus on the role of the equatorial ocean heat content as a precursor, the 24 strongest anomalous events in the HC_EW time series are composited (Figure 4.10a), accompanied by the corresponding composites of Nino3.4 (Figure 4.10b) and WS_SE (Figure 4.10c) that are aligned by the HC_EW peaks in Figure 4.10a. The threshold of anomalous HC_EW events is about twice the corresponding CTRL_SD and is chosen such that there are a comparable number of HC_EW events as ENSO events. The negative

anomalous events are again included by reversing the sign. The Nino3.4 and WS_SE series of those negative HC_EW events are also reversed accordingly. An individual event is marked as blue or red dashed line, while the average of all events as the black solid line. The horizontal black dashed lines in each plot indicate the corresponding CTRL_SD.

Figure 4.10 (a) Composite of HC_EW series for the 24 strongest HC_EW events. Negative anomalies are included with reversed sign. The HC_EW events that are followed by ENSO events of the same sign within 16 months are marked red, and the rest are marked blue. The blue (red) solid line is the average of all blue (red) dashed lines. (b) Composite of Nino3.4 index in *ada_south20* for the same events as (a); (c) Same as (b), but of WS_SE. (from [Lu et al., 2017b])



Although all the HC_EW events have significant heat content anomaly in the western Pacific, their composite Nino3.4 index following the HC_EW peaks is close to 0, indistinguishable from the natural variability of CTRL. Note the large spread among the Nino3.4 responses, we select those 12 HC_EW events that are followed by ENSO events (Nino3.4 over 0.5°C) of the same sign in the following 16 months and mark them red. The “red” events account for about half of the ENSO events in *ada_south20*. The remaining

12 HC_EW events are marked blue, and the averages of “red” and “blue” events are shown by the solid red and blue lines, respectively, in all of Figure 4.10. The 6 strongest HC_EW events are indeed “red”, but most other “red” and “blue” events are indistinguishable in terms of HC_EW magnitude. The “red” Nino3.4 composite hovers around only 0.2-0.4°C because the response time from the HC_EW peak to the Nino3.4 peak varies considerably. For the same reason of various Nino3.4 response time, there is no clear negative peak in the wind WS_SE composite for the “red” events (Figure 4.10c). However, the “red” WS_SE composite does stay negative in 6 of the 9 months following the HC_EW peak, while consistent and significant positive values of the “blue” WS_SE composite following the HC_EW peak are more notable (Figure 4.10c), indicating that intensified trade wind in southeast subtropical Pacific could hamper the possible ENSO onset induced by the heat content anomaly. It is also notable that very robust negative Nino3.4 anomalies precede the HC_EW events (Figure 4.10b), indicating the overshoot effect of previous ENSO events on subsequent equatorial heat content. The composite analyses based on the HC_EW events show that the heat content precursor is not a reliable predictor for ENSO onset (12 of 24 are followed by ENSO events), although its reliability could be increased (decreased) by subsequent favorable (unfavorable) extratropical atmospheric conditions.

The spatial pattern of the difference between the “red” and “blue” HC_EW events can be seen in the composites of the equatorial subsurface ocean (Figure 4.11). At the time of HC_EW peak (Figure 4.11a, d), the ocean temperature anomalies are almost identical, with cold anomalies at the surface and in the eastern Pacific and strong warm anomalies in the western Pacific thermocline. On average, the eastern Pacific is slightly cooler in “blue” events than in “red” ones. The warm temperature anomalies propagate eastward

for both “red” and “blue” events, however, the anomalies decay considerably for the “blue” events such that the magnitude and extent of the heat content anomaly in the eastern Pacific are much smaller in the “blue” events than in the “red” events (Figure 4.11e vs. b). At 6 months after the HC_EW peak, the “red” events have displayed considerable warming in the eastern Pacific SST (Figure 4.11c), while the warm anomalies in the “blue” events have disappeared and turned into substantial cooling in the eastern Pacific.

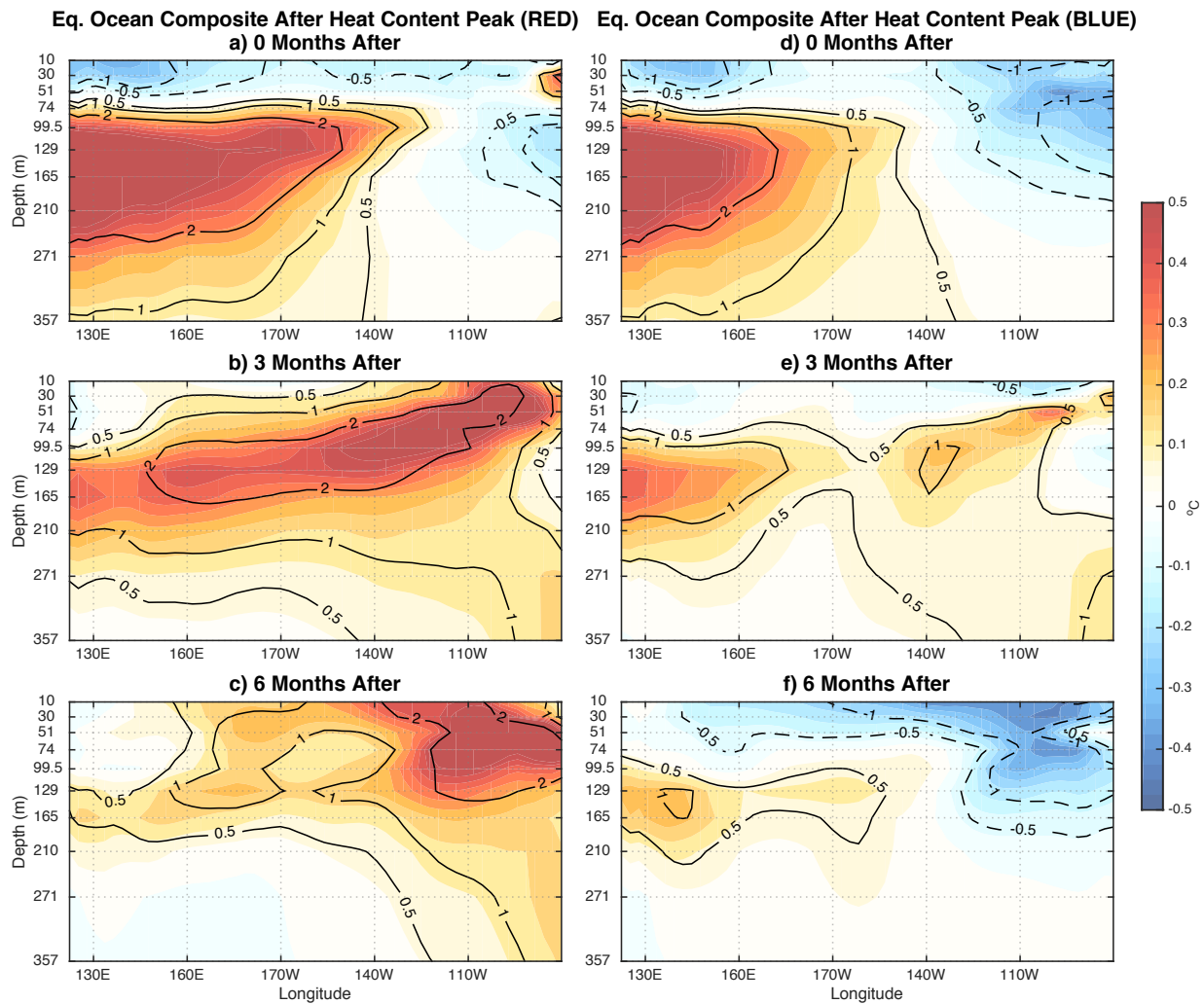


Figure 4.11 Same as Figure 4.9, but for the “red” (left column, a-c) and “blue” (right column, d-f) HC_EW events from Figure 4.10, respectively. The composites are at the same time as the peak of HC_EW composite (a, d), 3 months after (b, e), and 6 months after (c, f). (from [Lu et al., 2017b])

The comparison of the two evolutions is quite striking: almost identical thermocline anomalies in the western Pacific lead to completely different ENSO responses. Different from previous analyses of the observation or a fully coupled control simulation [Anderson, 2007; Deser *et al.*, 2012; Larson and Kirtman, 2013, 2014], the design of our experiments ensures that this difference is caused, ultimately, by the information from the extratropical atmosphere in the SH, rather than that in the NH or the initial conditions in the tropics.

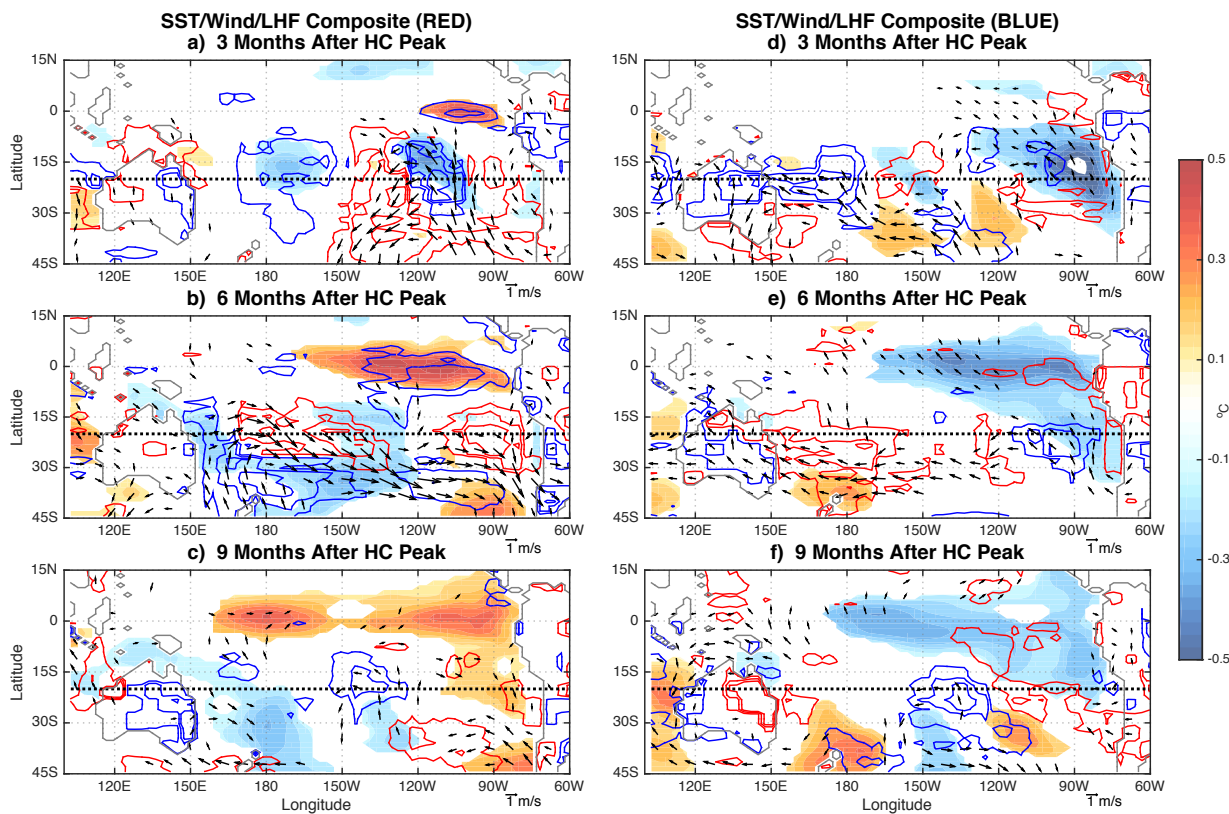


Figure 4.12 Same as Figure 4.8, but for the “red” (left column, a-c) and “blue” (right column, d-f) HC_EW events from Figure 4.10, respectively. The composites are at 3 months (a, d), 6 months (b, e) and 9 months (c, f) after the peak of HC_EW composite. (from [Lu *et al.*, 2017b])

The difference between the “red” and “blue” events can also be seen in the composites of the surface climate (Figure 4.12) for SST, wind and LHF composites at several lags after

the HC_EW peak. For the “red” events, the tropical warming following the HC_EW events is the direct surfacing of the subsurface anomalies in Figure 4.11, but it is not preceded by any significant extratropical anomalies as in Figure 4.8. Because the timing from HC_EW peaks to the triggering of ENSO events varies considerably for different events, the short extratropical signals would not result in robust composites in Figure 4.12a-c. Conversely and more notably for the “blue” events, cold SST anomalies and intensified trade winds persist in the southeast tropical and subtropical Pacific following the HC_EW peak, which could offset the positive temperature anomalies propagating eastward (Figure 4.11d-f) and hamper the possible onset of ENSO events. The discussion here suggests that equatorial heat content alone is insufficient to trigger ENSO and is therefore not a sufficient predictor for ENSO. This is consistent with an real-world observational analysis by [Anderson, 2007].

4.3.3. Extratropical Atmospheric Precursor

Next, we assess the extratropical atmospheric variability, namely WS_SE, as a precursor for ENSO events in *ada_south20*. Figure 4.13 shows the composite analyses based on the 24 strongest anomalous WS_SE events from *ada_south20* in the same way as the heat content in Figure 4.10. The threshold for WS_SE events is 1m/s and it is 7 times the corresponding CTRL_SD. The much stronger ensemble-mean wind variability compared to CTRL is due to the data assimilation in the WS_SE region. The composite in Figure 4.13a shows that all the WS_SE events have highly significant 1-month peaks (the width is enlarged due to the 3-month running average), reflecting the short timescale of the extratropical atmospheric internal variability. Most of these WS_SE events occur from May through August, since the model SH extratropical atmosphere is the most energetic in boreal summer. At the peak of the WS_SE composite, the SST, wind and LHF

anomalies (Figure 4.13b) resemble the precursor composite based on ENSO events in Figure 4.8b, albeit with much stronger magnitudes in wind and weaker magnitudes in the equatorial SST warming.

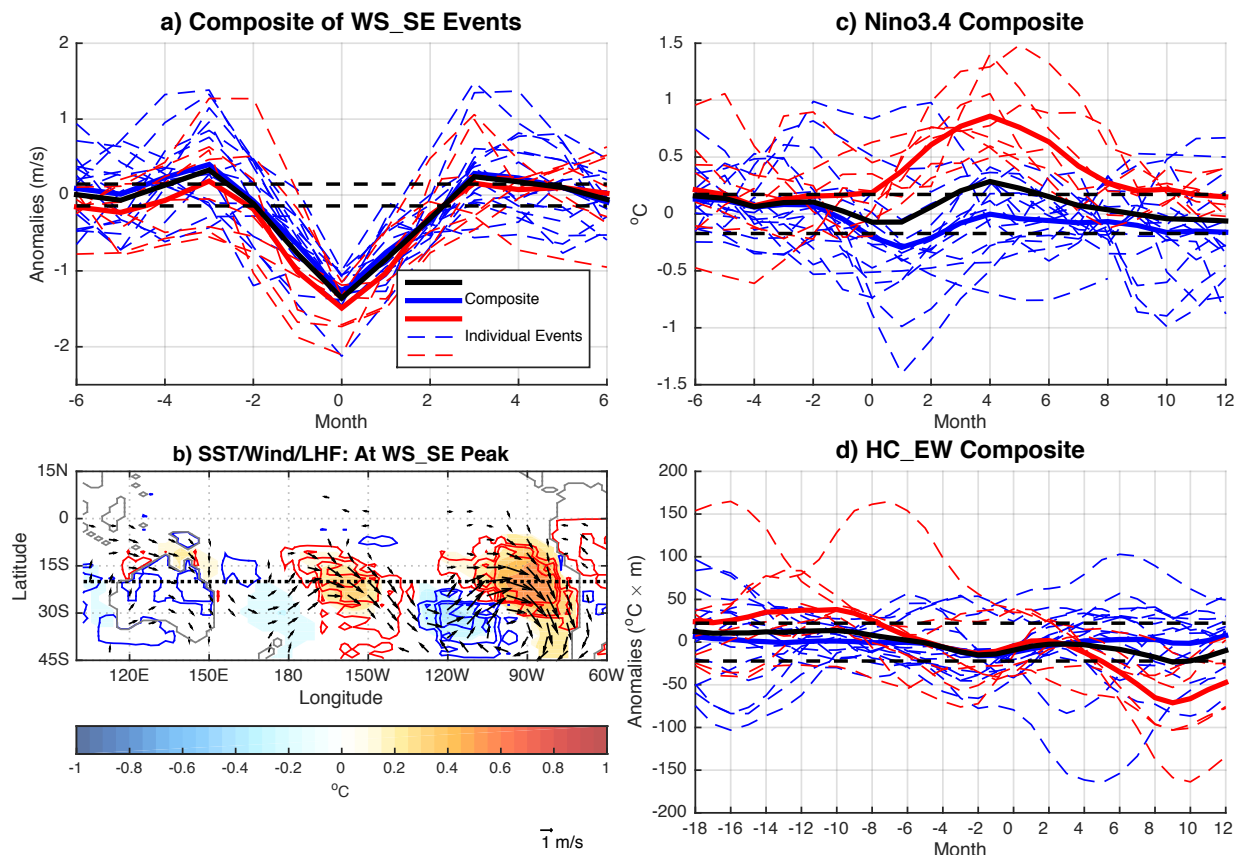


Figure 4.13 (a) Composite of WS_SE anomalies for the 24 strongest WS_SE events. Positive anomalies are included with reversed sign. The WS_SE events that are followed by ENSO events of opposite sign within 6 months are marked red, and the rest are marked blue. The blue (red) solid line is the average of all blue (red) dashed lines. (b) Same as Figure 4.8, but for all the WS_SE events at the peak. (c) Composite of Nino3.4 index in *ada_south20* for the same events as (a); (d) Same as (c), but of HC_EW. (from [Lu *et al.*, 2017b])

Following the WES feedback as in Figure 4.8, the coupled anomalies of reduced wind speed, weaker LHF cooling, and warm SST could propagate into the equatorial region and trigger ENSO onset in about 2 months. However, on average, the Nino3.4 composite reaches the maximum of only 0.28°C and stays within or very close to CTRL_SD

throughout the entire period following the WS_SE peaks (black solid, Figure 4.13c). Among the 24 WS_SE events, only 8 are followed by ENSO events (Nino3.4 over 0.5°C) of the correct sign in the following 2-6 months. Again, we mark these 9 events in red (dashed) and the other 16 in blue (dashed), and plot their averages as the solid red and blue lined, respectively. In terms of the magnitude of the WS_SE events, the “red” average is indistinguishable from the “blue” average (Figure 4.13a), but the subsequent responses in Nino3.4 are notably different: the “red” average exhibits a significant warming 4 months after the negative peak of WS_SE, while the “blue” average exhibits no warming after the wind peak (Figure 4.13c). The HC_EW composite based on the WS_SE events is plotted in Figure 4.13d. The 3 WS_SE events that are preceded by large positive HC_EW values are indeed “red”, while the other 6 “red” events do not have significant leading HC_EW events. On average, the positive “red” HC_EW composite is primarily caused by the 3 events with large HC_EW values. Like the heat content precursor, the composite analyses based on the WS_SE events show that the extratropical atmospheric precursor alone is not a reliable predictor either (9 of 24 are followed by ENSO events), while favorable equatorial preconditioning could increase its skill.

The preconditioning role of the equatorial ocean can also be seen by comparing the preceding patterns of SST and heat content between the “red” and “blue” events. The surface conditions at the peak of the WS_SE composite are plotted for “red” and “blue” events separately in Figure 4.14. While the SH extratropical anomalies remain the same as in the total composite in Figure 4.13b, there is a dramatic difference in the equatorial eastern Pacific. The “red” events have the same equatorial warming as in Figure 4.8, while the “blue” events have slight cooling in the equatorial Pacific. This cold anomaly does not favor the onset of ENSO events, and is likely to prevent the extratropical atmospheric

variability from triggering ENSO. Indeed, the difference in equatorial SST between the “red” and “blue” events can be traced back to the subsurface conditions prior to the WS_SE events. Figure 4.15 shows the composites of ocean temperature anomaly 8 and 4 months prior to, and at simultaneous time of WS_SE events for the “red” and “blue” events, separately. The subsurface evolution of the “red” events (Figure 4.15a-c) matches the development in the composites of Figure 4.9 and Figure 4.11a-c. In contrast, the “blue” events exhibit weak to moderate subsurface cooling across the entire Pacific thermocline (Figure 4.15d-f), which does not provide the favorable preconditioning for the onset of ENSO events. The discussion here suggests that, like the heat content, the extratropical atmospheric variability alone is insufficient to trigger ENSO and therefore is not a sufficient precursor, either.

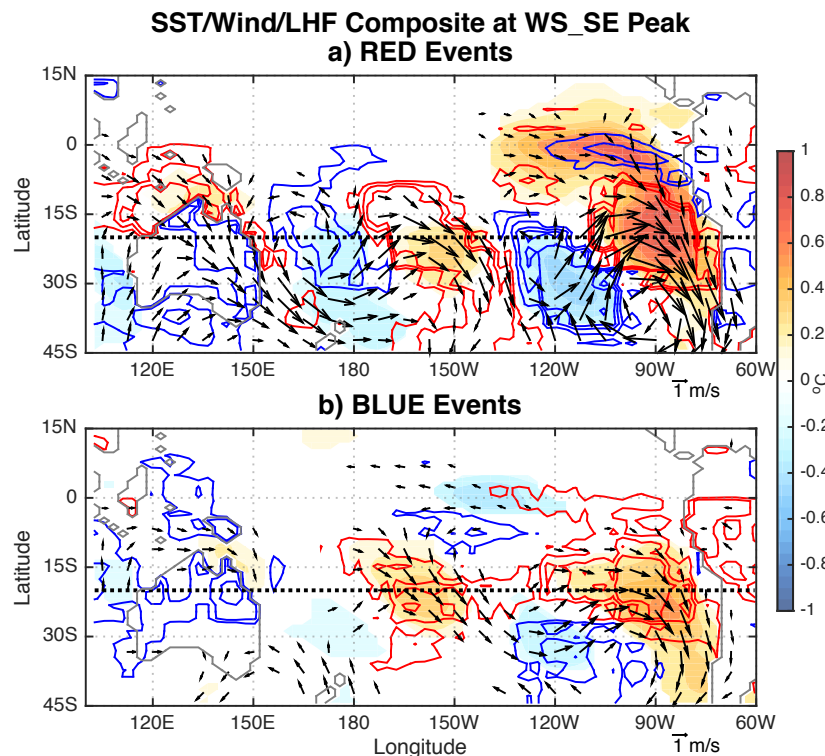


Figure 4.14 Same as Figure 4.13b, but for (a) “red” and (b) “blue” events, respectively. (from [Lu *et al.*, 2017b])

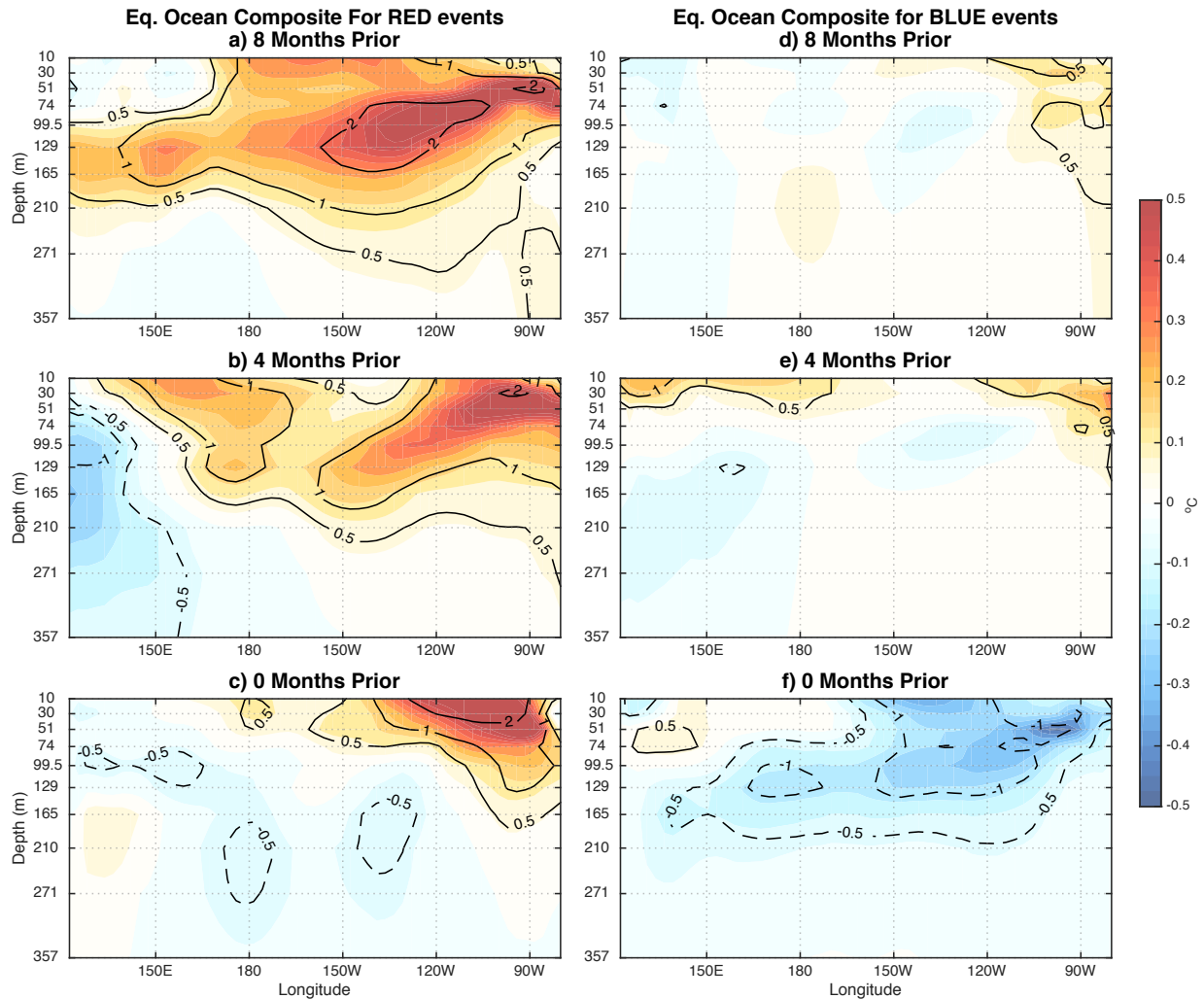


Figure 4.15 Same as Figure 4.9, but for the “red” (left column, a-c) and “blue” (right column, d-f) WS_SE events from Figure 4.13a, respectively. The composites are 8 months (a, d), 4 months (b, e) prior to, and at the same month (c, f) as the peak of the WS_SE composite. (from [Lu *et al.*, 2017b])

4.3.4. The Precursors Combined

The discussions above show that both WS_SE and HC_EW demonstrate robust signals prior to ENSO events in *ada_south20* and therefore can be considered as potentially necessary precursors for ENSO onset. However, neither is sufficient to trigger ENSO by itself and be considered as a reliable predictor. This is consistent with previous studies of observational and model analyses [Anderson, 2007; Deser *et al.*, 2012; Larson

and Kirtman, 2013, 2014, 2015]. These previous works further suggested that the combined effect of both equatorial preconditioning and extratropical atmospheric variability is more likely to trigger ENSO. This point seems to be consistent with our study here (Figure 4.10 through Figure 4.15).

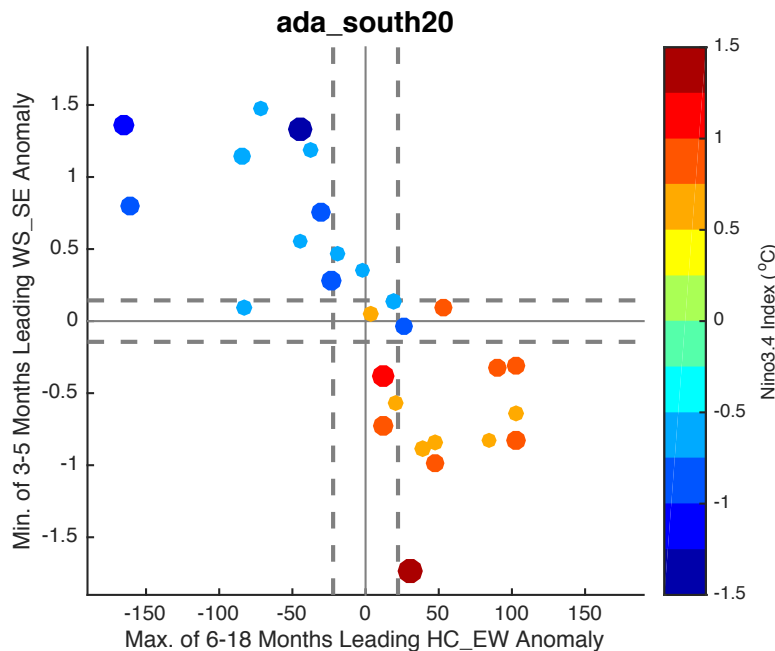


Figure 4.16 Scatterplot of all 29 ENSO events in *ada_south20* based on the minimum opposite-sign value of 3-5 months leading WS_SE (y-direction) and maximum same-sign value of 6-18 months leading HC_EW (x-direction). The color and size of the markers together indicate the peak Nino3.4 values. The dashed lines indicate the corresponding CTRL_SD. (from [Lu et al., 2017b])

The combined effect of both the WS_SE and HC_EW precursors can be illustrated more clearly in Figure 4.16, which is the scatterplot of the peak Nino3.4 values of all 29 ENSO events in *ada_south20* based on the maximum WS_SE (opposite-sign) in the range of 3-5 months prior to Nino3.4 peak and the maximum HC_EW value (same-sign) in the range of 6-18 months prior. Most El Niño events are in the bottom right quadrant, preceded by significantly negative WS_SE and positive HC_EW values. Conversely, the upper left quadrant contains most La Nina events, which are preceded by significantly

positive WS_SE and negative HC_EQ values. Based on Figure 4.16, it may seem that WS_SE and HC_EW is negatively correlated. However, this “correlation” exists because only the values preceding ENSO events are chosen and more importantly, each precursor is chosen from a range of leading times to highlight its impact on ENSO variability. The entire WS_SE and HC_EW series in the *ada_south20* experiment vary independently with a correlation of -0.01.

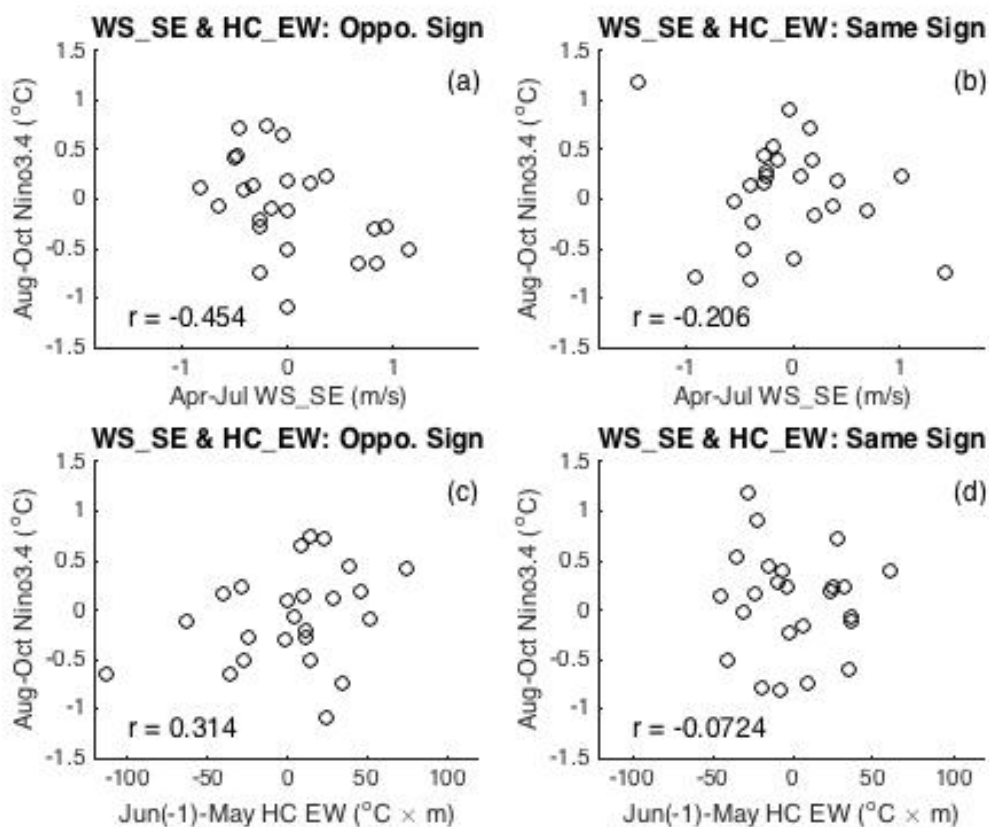


Figure 4.17 (a) Scatterplot of the April-July averaged WS_SE with August-October averaged Nino3.4 index of the same year, plotted for the years when the averaged WS_SE has the opposite sign as the June (previous year)-May (same year) averaged HC_EW . (b) Same as (a), but for the years when the averaged WS_SE has the same sign as the averaged HC_EW . (c) Scatterplot of the June (previous year)-May (same year) averaged HC_EW with August-October averaged Nino3.4 index, plotted for the years when the April-July averaged WS_SE has the opposite sign as the averaged HC_EW . (d) Same as (c), but for the years when the averaged WS_SE has the same sign as the averaged HC_EW . (from [Lu et al., 2017b])

The combined effect of WS_SE and HC_EW is further demonstrated in Figure 4.17, which is the same as the Fig. 3 of [Anderson, 2007] and Fig. 19 of [Deser *et al.*, 2012]. In Figure 4.17, the correlation between April-July averaged WS_SE or June (previous year)-May averaged HC_EW and August-October averaged Nino3.4 of all years in *ada_south20* is separately estimated depending on whether the leading averaged WS_SE and HC_EW have the opposite or same sign. When the averaged WS_SE and HC_EW have the opposite sign, the two precursors may work together to trigger ENSO onset; when they have the same sign, they may work against each other and fail to trigger ENSO onset. Figure 4.17 shows that for averaged WS_SE (HC_EW), its negative (positive) correlation with the subsequent Nino3.4 is larger in the opposite-sign case (Figure 4.17a, c) than the same-sign case (Figure 4.17b, d). The inability of the two precursors to explain all the ENSO events is also reasonable, since ENSO variability can be forced by atmospheric variability features not considered here, such as the atmospheric variability in the central and western subtropical Pacific. The analyses on the SH impact in *ada_south20* can also be carried out similarly for the NH impact in *ada_north20*, a point to return to later.

The effectiveness of WS_SE and HC_EW together as a ENSO precursor (Figure 4.16) and their relation with each other (Figure 4.17) are consistent qualitatively with the previous works on ENSO precursors in the real world [Anderson, 2007] and climate models [Deser *et al.*, 2012; Larson and Kirtman, 2013, 2014]. However, there is an important difference between our study and previous studies. By experimental design, all the significant ensemble-mean tropical responses in *ada_south20* or *ada_north20*, including the ENSO events, are ultimately forced by SH or NH extratropical atmospheric variability. In contrast, the ENSO events in the observation or a fully coupled model simulation could be simultaneously related to extratropical variability from both

hemispheres as well as internal climate variability within the tropics. The exclusively forced tropical response in our model assures that the equatorial heat content anomaly precursor is also forced, somehow, by the extratropical atmosphere. In contrast, the ocean preconditioning in previous observational or modeling studies could be caused, again by extratropical variability from both hemispheres and tropical natural variability. It remains to be studied how the equatorial subsurface ocean is preconditioned by extratropical atmospheric variability. Tentatively, we speculate the heat content anomaly can be induced by the oceanic teleconnection [Matei *et al.*, 2008], with the extratropical atmospheric variability directly forcing subtropical oceanic anomaly, which then propagations into the equatorial ocean via oceanic Rossby wave and the subsequent tropical thermocline adjustment [Kirtman, 1997; Anderson *et al.*, 2013; Anderson and Perez, 2015], or via thermocline subduction [Liu *et al.*, 1994; Schott *et al.*, 2004]; it can also be forced directly by the atmospheric adjustment from the subtropics [Pierce *et al.*, 2000].

4.4. Summary and Discussion of Chapter 4

This section studies the control of extratropical atmospheric variability on ENSO variability in a CGCM using a limited-domain CDA system, in which the active assimilation is confined to the extratropics. The extratropical atmospheric variability is shown to have significant impact on ENSO variability, while the extratropical SST has no influence on ENSO at the timescale considered here. When atmospheric observations are assimilated only poleward of 20° in both hemispheres, most of the strong ENSO events in observation are reproduced in *ada_20* and the RMSE of the Nino3.4 index is reduced by over 40% compared to *CTRL* with no assimilation. The comparison with *CTRL* also indicates that any robust ensemble-mean tropical variability must be attributed to the

assimilated extratropical atmosphere ultimately. Furthermore, the forced ENSO variability is contributed independently and roughly equally by the atmospheric forcing from the NH and SH extratropical atmosphere, as shown by *ada_south20* and *ada_north20*.

Composite analyses of the ENSO events in *ada_south20* reveal robust signals in both extratropical atmosphere and equatorial subsurface Pacific, following previous studies of SPM and the discharge-recharge paradigm. Specifically, most *ada_south20* ENSO events are preceded by corresponding precursors of wind speed, LHF and SST anomalies in the southeast subtropical Pacific like the SPM and heat content anomalies in the equatorial western Pacific. Furthermore, the ability of each precursor to act as a predictor is investigated based on their own composites in *ada_south20*. It is found that neither the extratropical atmospheric nor the tropical oceanic precursor alone is sufficient to trigger ENSO onset. The combined effect of the two precursors is also considered: when one precursor strongly favors ENSO onset, the other should also be favorable, or at least neutral for the emergence of ENSO. The existence of ENSO events without either precursor indicates the possibility of other connections from SH extratropical atmosphere to ENSO variability.

Detailed analysis of the *ada_north20* experiment, which is performed in the same way as *ada_south20*, is not shown in this paper. The major conclusions from *ada_south20* qualitatively hold for *ada_north20*, although the results are somewhat more complex for *ada_north20*. In *ada_north20*, most ENSO events are preceded by wind, LHF and SST anomalies in the northeast and north-central subtropical and tropical Pacific, while only some are preceded by heat content anomalies in the equatorial western Pacific. The extratropical signals in *ada_north20* spread over a larger region compared

to *ada_south20* and resemble the key patterns of the NPMM. However, a few notable differences should be pointed out. First, *ada_north20* appears to include both the Central-Pacific (CP) and Eastern-Pacific (EP) types of ENSO events [Yu and Kao, 2007; Kao and Yu, 2009], while *ada_south20* includes the EP type exclusively. The EP type in *ada_north20* is preceded by significant HC_EW precursor like *ada_south20*, while the CP type is not. Furthermore, the CP type in *ada_north20* is more closely linked to preceding SST anomalies in the northeast subtropical Pacific and NH trade wind anomalies, similar to the “footprinting” mechanism [Vimont et al., 2001, 2003a, 2003b] and the trade wind charging [Anderson et al., 2013; Anderson and Perez, 2015]. The relation between NPMM or SPMM and different types of ENSO events has been investigated by several studies [Yu et al., 2010; Vimont et al., 2014; Zhang et al., 2014; Yeh et al., 2015], and most of which agree that NPMM is related to both types while SPMM leads to mostly the EP type. The different types of ENSO events and their respective mechanism in *ada_north20* will be explored in the future.

The quantitative strength of the extratropical control on ENSO variability depends on the dynamics of the model. The same *ada_20* experiment is also performed in two other versions of FOAM with modified model parameters and shows significantly different strength of extratropical control. In one version of FOAM, ENSO becomes much stronger than the default version and is dominated by a biennial oscillation. In this version, the extratropical atmospheric variability has little impact on ENSO, suggesting the ENSO is generated predominantly by the tropical coupled system. In another version of FOAM, ENSO becomes weaker and its spectrum appears much “redder”. In this version, the extratropical atmosphere exerts an even stronger control on ENSO than in the default version. Our diagnosis of the control simulations of the various versions of FOAM

suggests that the default version is the closest to the real world. In addition, the almost equal strength of extratropical control from both hemispheres could also be model-specific. Nevertheless, we caution the direct application of the quantitative results in this study to other CGCMs and the real world.

There are still many issues to be further explored on the current study. As previously discussed, the coupled dynamics in the eastern Pacific should only be one of the mechanisms by which extratropical atmosphere could influence ENSO variability. In addition, it remains unclear how the ocean preconditioning is caused by extratropical atmospheric variability. More analyses are needed to investigate the roles of atmospheric/oceanic/coupled processes in transferring extratropical variability into the tropics. This pilot study also serves to demonstrate of the utility of the limited-domain CDA method, or more generally the use of coupled data assimilation in studying climate dynamics. The real potential of this method would be its application to the understanding of the real-world ENSO events using a state-of-the-art CGCM. With this new method based on the CDA system, Section 0 will investigate the specific atmospheric noise forcing and related coupled dynamics that contribute to the historical ENSO events.

Chapter 5

5. Extratropical Influence on Tropical Variability: Applications with Real-world Observations

In Chapter 4, the extratropical influence on ENSO variability is studied within the model dynamics of FOAM in a perfect-model framework. Here in Chapter 5, the extratropical influence on historical ENSO variability is studied by assimilating real-world reanalysis data into FOAM, which is a biased model compared to the observation. The same experiments as in Chapter 4 are repeated with reanalysis data. Additional sensitivity and forecast experiments are performed to study the triggers of a few ENSO events. Part of the results in this chapter will be reported in an upcoming paper [*Lu and Liu, 2017*].

5.1. Datasets and Experiment Design

The experiments in this chapter again use FOAM and the RCDA method described in Section 2.1 and Section 2.4, respectively. The same reanalysis datasets as in Chapter 3 (NCEP/NCAR Reanalysis 1 and NOAA ERSST) are assimilated in the RCDA experiments here. See Section 3.1 for a detailed description of the setup of the assimilation system and Table 5.1 for the list of experiments. Most of the analysis in this chapter is based on the same set of experiments in Chapter 3 unless noted otherwise. Some experiments are repeated with the addition of 2016 observations for validation purposes. Additional short-term (2 to 3 years) forecast or assimilation experiments are performed to test the sensitivity of ENSO onset and development to different tropical and extratropical precursors.

Assimilated Variables & Latitudes	None	Atm T/U/V & SST (coupled)	Atm T/U/V	SST
None	<i>ctrl</i>			
All		<i>cda_all</i>	<i>ada_all</i>	<i>oda_all</i>
>10°N & <10°S		<i>cda_10</i>	<i>ada_10</i>	<i>oda_10</i>
>15°N & <15°S		<i>cda_15</i>	<i>ada_15</i>	<i>oda_15</i>
>20°N & <20°S		<i>cda_20</i>	<i>ada_20</i>	<i>oda_20</i>
>24°N & <24°S		<i>cda_24</i>	<i>ada_24</i>	<i>oda_24</i>
>28°N & <28°S		<i>cda_28</i>	<i>ada_28</i>	<i>oda_28</i>
>33°N & <33°S		<i>cda_33</i>	<i>ada_33</i>	<i>oda_33</i>
>37°N & <37°S		<i>cda_37</i>	<i>ada_37</i>	<i>oda_37</i>
>42°N & <42°S		<i>cda_42</i>	<i>ada_42</i>	<i>oda_42</i>

Table 5.1 Table of all RCDA experiments in Chapter 5.

5.2. Overview of Results

5.2.1. ENSO Variability

The Nino3.4 indices from selected RCDA experiments are shown in Figure 5.1 (*ctrl*, *cda_all*, *ada_all* and *oda_all*) and Figure 5.2 (*ada_10*, *ada_20*, *ada_28* and *ada_37*). The strongest ENSO events in the past 70 years are marked by the circles, which are red for El Niño events and blue for La Nina events. The *ctrl* experiment shows no ensemble-mean ENSO variability like the perfect-model study in Chapter 4 (Nino3.4 correlation with observation $R=-0.012$). In the RCDA experiments where observation coverage is global, FOAM could produce accurate historical ENSO variability. Among *cda_all*, *ada_all* and *oda_all*, *oda_all* is the most accurate in terms of Nino3.4 index due to its

direct constraint on SST ($R=0.874$), while *ada_all*, despite its constraint on the atmosphere, is the least accurate because of the model bias in the coupling and oceanic components ($R=0.746$). Although *oda_all* assimilates the most observations, it slots between *oda_all* and *ada_all* in the ability to reproduce observed ENSO variability ($R=0.818$).

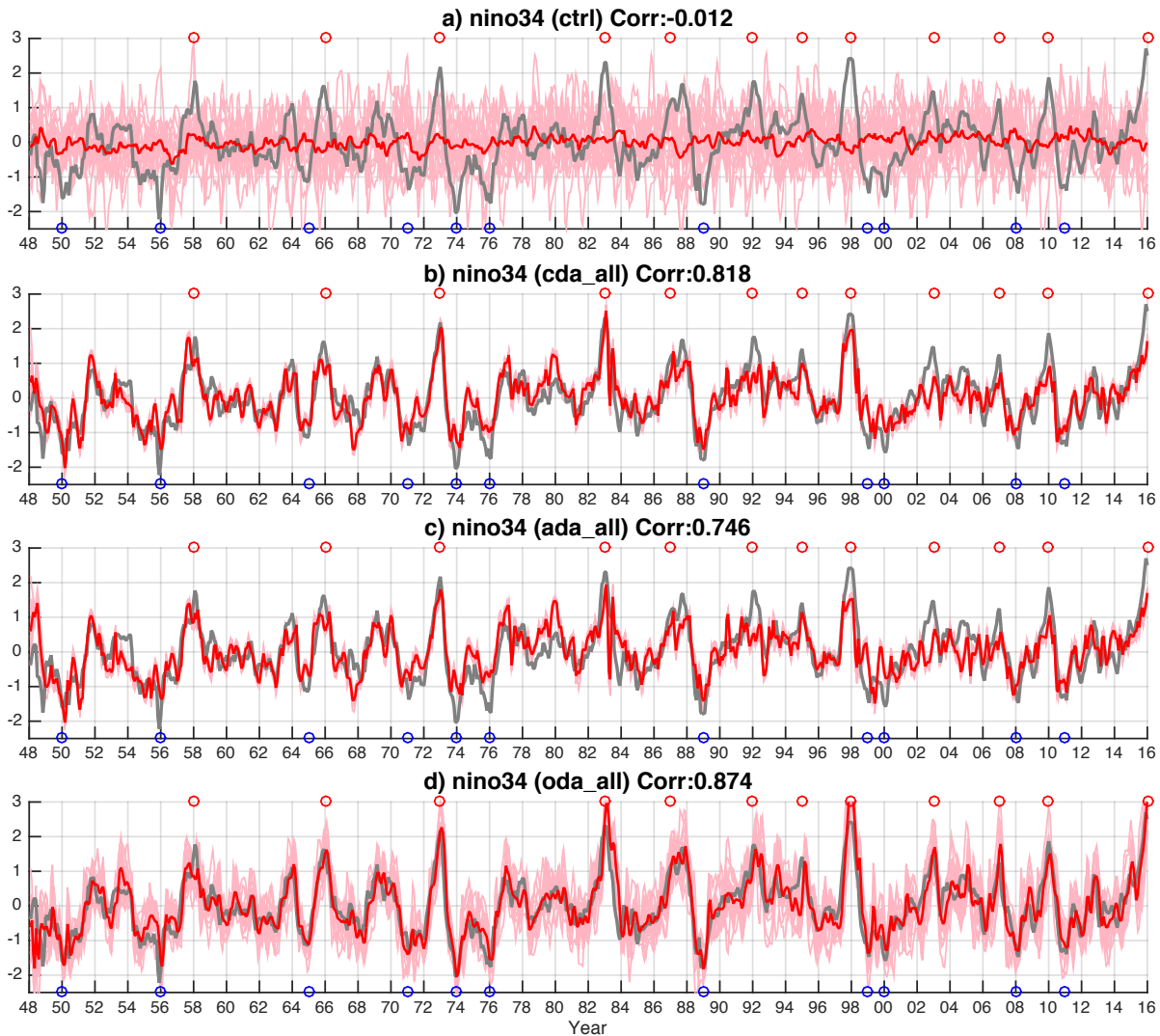


Figure 5.1 The time series of Nino3.4 index from (a) *ctrl*, (b) *cda_all*, (c) *ada_all* and (d) *oda_all*. Grey lines indicate the observed Nino3.4 index (same for all panels), red lines the ensemble mean, and pink lines all 16 ensemble members.

Next we focus on the *ADA* experiments. Like the perfect-model experiments in Chapter 4, the accuracy of the Nino3.4 variability declines as the assimilation boundary moves poleward. The Nino3.4 index correlation with observation decreases from 0.746 in *ada_all* to 0.655 in *ada_10*, 0.49 in *ada_20*, and 0.325 in *ada_28*. Their perfect-model counterparts have Nino3.4 correlations that are around 0.2 higher, ranging from over 0.9 to about 0.5. Overall, the control of extratropical atmospheric variability on ENSO variability is weaker in the real-world experiments than in the perfect-model experiments. This could be caused by several reasons, most of which are related to the presence of model bias. First, the analysis quality in the regions with data assimilation is worse in the real-world experiments. Second, FOAM may be lacking or biased in some aspects of model dynamics and feedbacks related to extratropical-to-tropical teleconnection. Third, there are discrepancies between the regions with assimilation and those without. For example, the climatological annual cycle of SST is dragged toward observation in the extratropics, but it is still affected by FOAM's biased climatology in the tropics without assimilation (Figure 5.5 and Figure 5.6). Last but not the least, it is possible that the extratropical control on ENSO variability is weaker in the real world than in FOAM. As we mentioned in Section 4.4, the extratropical control on ENSO variability in FOAM could be made stronger or weaker depending on certain model parameters. The real-world extratropical control could be weaker than that in our current version of FOAM. Despite all these reasons, experiments like *ada_20* and *ada_28* did reproduce a few ENSO events and partial variability. For example, in *ada_20*, correct warming or cooling of the Nino3.4 index is reproduced for 1955-56 La Nina, 1957-58 El Niño, 1972-73 El Niño, 1986-87 El Niño, 1988-89 La Nina, 1997-98 El Niño, and 2009-10 El Niño, although many of these reproduced events are inaccurate in magnitude and/or off in timing by a few months. The

magnitude issue could be caused by the FOAM's model bias in ENSO-related equatorial dynamics, while the timing issue could be related to the ENSO phase-locking in FOAM. Both issues will be discussed later in this chapter. Furthermore, *ada_28* also reproduces ENSO events like 1957-58 El Niño, 1972-73 El Niño, and 2007-08 La Niña. The accuracy of the 1972-73 El Niño in both *ada_20* and *ada_28* is particularly prominent, which will be analyzed in details in Section 5.3. The ability to reproduce ENSO variability is almost gone in *ada_37*.

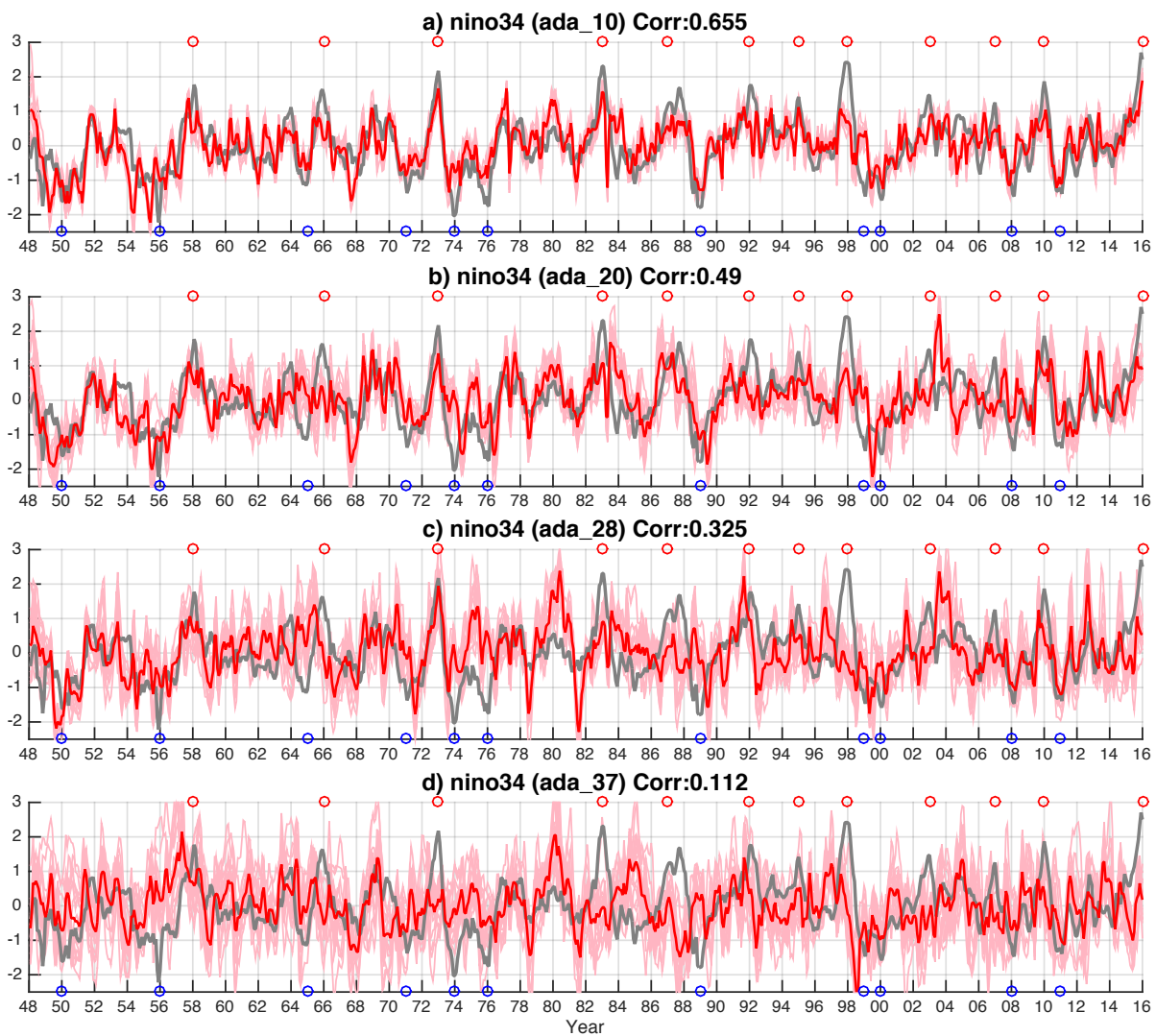


Figure 5.2 Same as Figure 5.1, but for (a) *ada_10*, (b) *ada_20*, (c) *ada_28* and (d) *ada_37*.

Among the strongest El Niño events, the contrast between the 1972-73 event and the 1997-98 event among the *ADA* experiments is particularly interesting. While the 1972-73 El Niño is reproduced accurately in *ada_20* and even *ada_28*, the 1997-98 El Niño is weak in *ada_20* and complete absent in *ada_28*. Previous study has shown that both events are preceded by North Pacific Meridional Mode (NPMM) signals, however, this contrast in RCDA experiments indicates the extratropical control on these two events may be completely different despite similar NPMM precursors. These two events and their precursors will be further analyzed in Section 5.3 and 5.3.2.

The power spectrum of the Nino3.4 index is not heavily affected in the RCDA experiments. In Figure 5.3, *ctrl* represents a single member FOAM control simulation since the *ctrl* experiment has almost no ensemble-mean ENSO variability. FOAM has a realistic ENSO cycle of 2-7 years, slightly weaker than observation at lower frequency in the range. The *ADA* experiments still have similar Nino3.4 power spectrum, indicating mostly unchanged intrinsic ENSO dynamics in the coupler and ocean components.

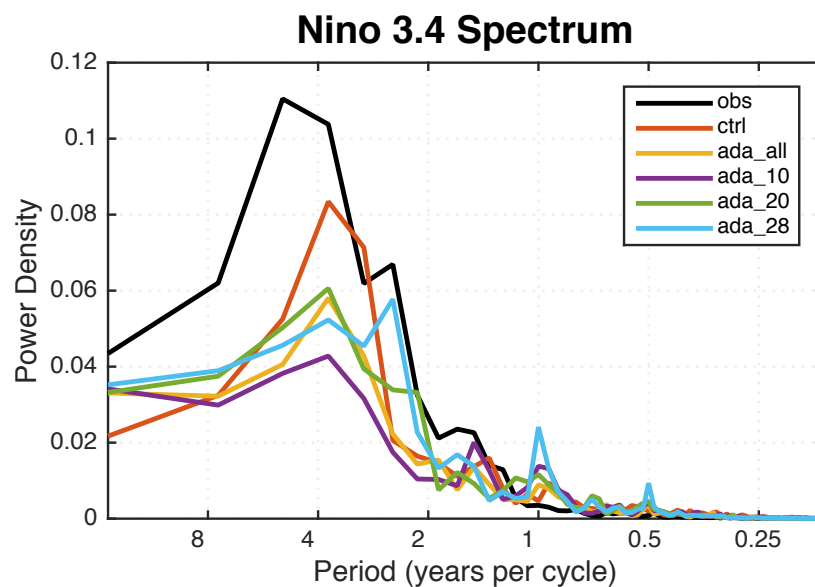


Figure 5.3 The power spectrum of the Nino3.4 index from observation, *CTRL*, *ada_all*, *ada_20* and *ada_28*.

Overall, the influence of extratropical assimilation is seen more clearly in Figure 5.4, which contains the Nino3.4 index correlation and RMSE of all RCDA experiments. With no assimilation, *ctrl* has a correlation close to 0 with the observed Nino3.4. When the assimilation boundaries expand equatorward, the correlation gradually and linearly increases for *ADA* and *CDA* experiments, but not for *ODA* experiments. As demonstrated in the perfect-model experiments, extratropical SST assimilation (*oda_15* and beyond) has almost no influence on the ENSO variability, and the effect of *ODA* only materializes when SST assimilation reaches inside 15°. Like the correlation, the RMSE of *ADA* and *CDA* experiments decrease when the assimilation boundaries move equatorward. The RMSE is relatively small for *ctrl* because the *ctrl* ensemble-mean Nino3.4 index just hovers around 0, thus reducing the error variance. Figure 5.2 and Figure 5.4 are clear evidence that certain extratropical atmospheric variability has a causal effect on ENSO variability.

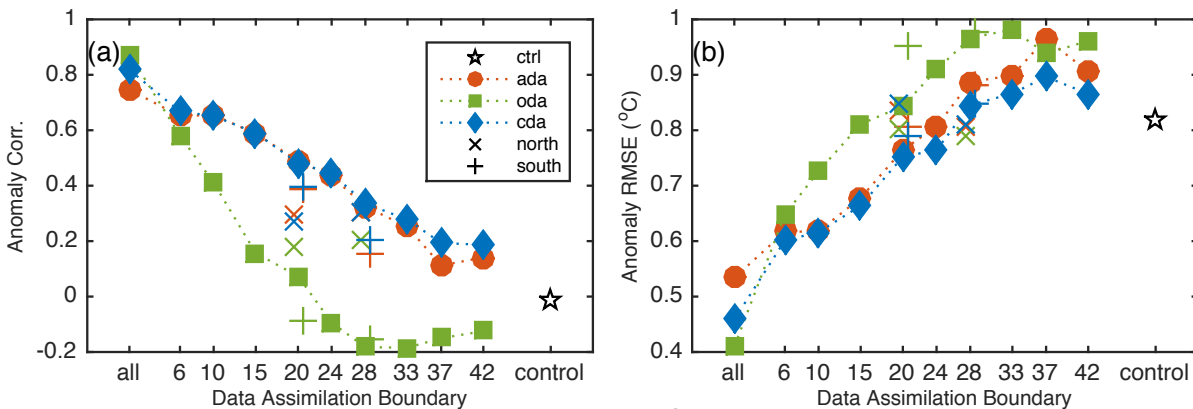


Figure 5.4 A summary of ENSO variability statistics from *CTRL* (asterisk), *CDA* (blue diamond), *ADA* (red circle), and *ODA* (green square) experiments. (a) Correlation of Nino3.4 index with the observation. (b) RMSE of Nino3.4 index compared to observation.

5.2.2. Annual Cycle and ENSO Phase-locking

Besides the annual-mean climatological features discussed in Chapter 3 and the interannual variability shown in Section 5.2.1, another important aspect of the tropical climate is the seasonality of the tropical climate and ENSO variability, as well as their interaction. Current climate models, even the state-of-the-art ones, are still unable to simulate some of the tropical features such as the annual—instead of semi-annual—cycle of SST and precipitation in the Eastern Tropical Pacific, the phase-locking of ENSO variance with the seasonal cycle, and the spring barrier of ENSO prediction [Bellenger *et al.*, 2014; Li and Xie, 2014; Chen *et al.*, 2016].

The observed equatorial Pacific SST shows a weak semi-annual cycle in the western part and a strong annual cycle in the eastern part (Figure 5.5a). In comparison, FOAM has an annual cycle in the west and a slightly semi-annual cycle in the east. With tropical and/or extratropical atmospheric data assimilation, the semi-annual cycle in the east is replaced by an annual cycle, in addition to the improved annual-mean climatology shown in Chapter 3. The improvement comes mainly from the southern hemisphere since *ada_S20* is very close to *ada_20* while *ada_N20* is more like *ctrl*.

The Eastern Pacific seasonal cycle is shown in Figure 5.6. The most prominent bias in FOAM is the warm boreal spring SST in the southeastern tropical Pacific (Figure 5.6b vs. a), which is highly correlated with the double-ITCZ bias since SST and precipitation are strongly coupled in the tropics. The warm SST bias is much reduced in the ADA experiments, which again mainly comes from the southern hemisphere as shown by *ada_S20* (Figure 5.6h).

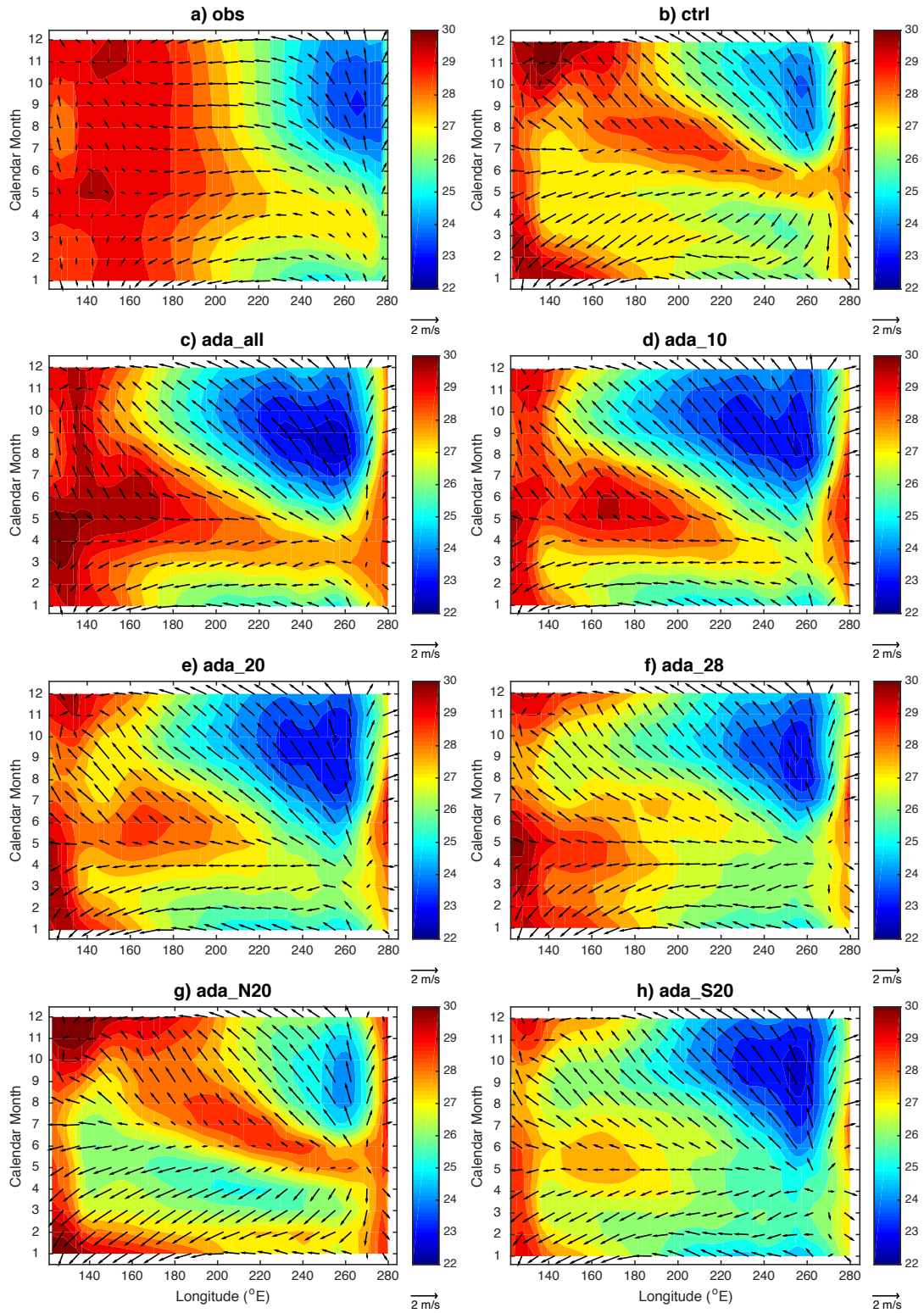


Figure 5.5 Equatorial (5°S - 5°N average) Pacific SST and wind annual cycle for (a) CTRL, (b) observation, (c) *ada_all*, (d) *ada_10*, (e) *ada_20*, (f) *ada_28*, (g) *ada_N20* and (h) *ada_S20*.

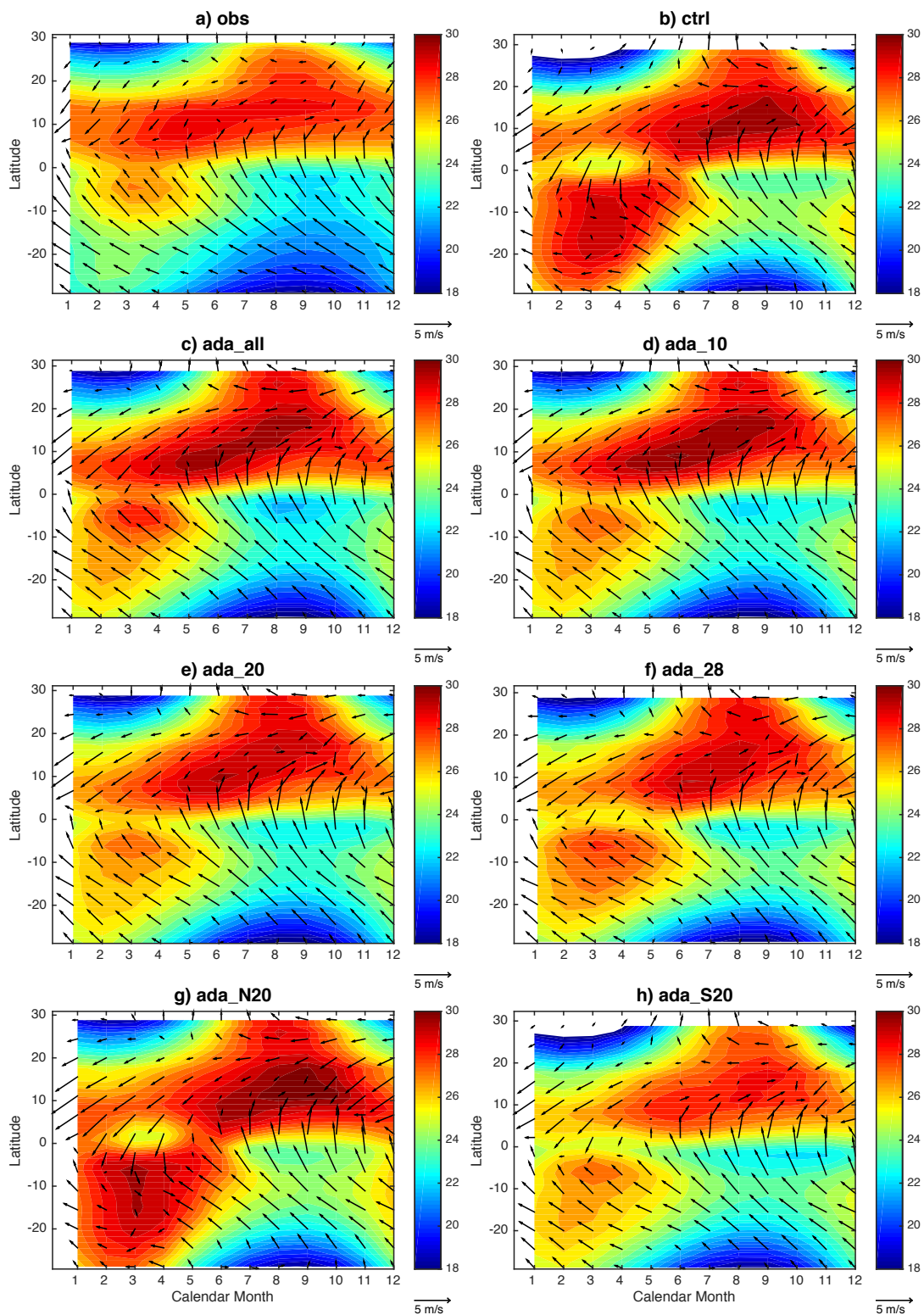
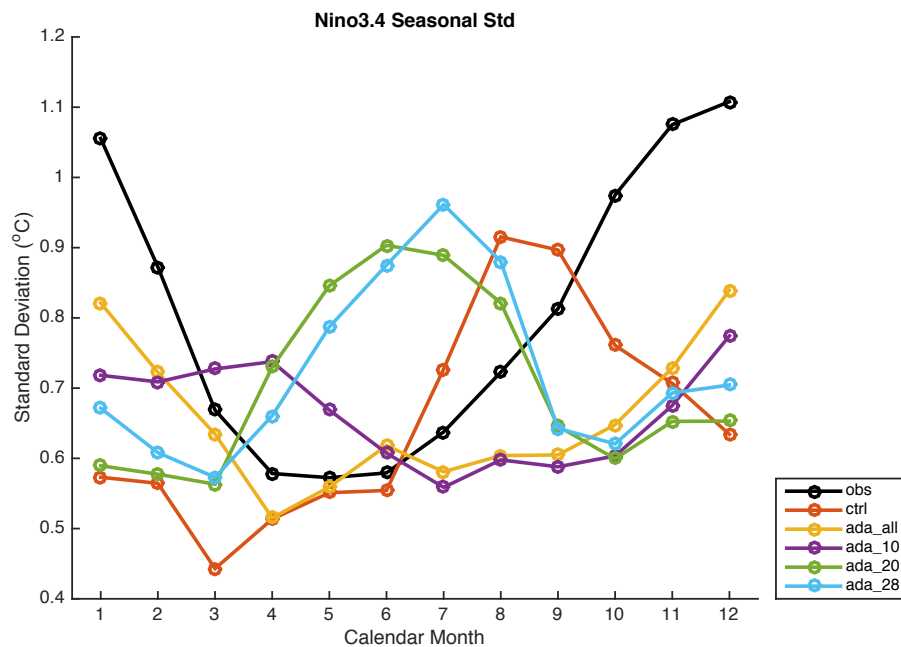


Figure 5.6 Eastern (80°W-120°W average) Pacific SST and wind annual cycle for (a) CTRL, (b) observation, (c) *ada_all*, (d) *ada_10*, (e) *ada_20*, (f) *ada_28*, (g) *ada_N20* and (h) *ada_S20*.

In observation, a typical ENSO event—as represented by the Nino3.4 index—usually develops in boreal summer and fall, and peaks in boreal winter. This phenomenon is called the phase-locking between ENSO variability and the seasonal cycle. This can be seen from the standard deviation of the observed Nino3.4 index by calendar month (black line in Figure 5.7). In contrast, the ENSO variance in FOAM control simulation grows mostly in boreal summer and peaks in boreal fall (orange line in Figure 5.7). When assimilation is available in or close to the deep tropics (*ada_all* and *ada_10*), the RCDA experiments produce the correct phase-locking, while extratropical assimilation (*ada_20* and *ada_28*) moves the strongest Nino3.4 variance to the summer, even farther away from the correct phase-locking. The inability of FOAM—and some other climate models—to produce the correct phase-locking could be attributed to many sources, including biased tropical climatology and seasonal cycle, deficiency in coupled instability, and wrong forcing of ENSO onset. These problems are likely connected and all contributing to the biased phase-locking.

Figure 5.7 Standard deviations of Nino3.4 index by calendar month in observation, CTRL, *ada_all*, *ada_10*, *ada_20* and *ada_28*.



5.2.3. Equatorial Pacific Heat Content

The equatorial Pacific upper-ocean heat content is an important indicator of ENSO variability and a common precursor for ENSO onset. The $t300$ index, the average temperature in the equatorial Pacific upper ocean (5°S - 5°N , 120°E - 80°W , 0-300m), is shown for observation and some RCDA experiments in Figure 5.8 and Figure 5.9. Like the Nino3.4 index, ctrl has no ensemble-mean $t300$ variability either. The *cda_all* experiment can be considered our own reanalysis product, and its $t300$ index will be used as the reference to judge other RCDA experiments. The $t300$ index from *cda_all* is highly correlated with those from SODA (Simple Ocean Data Assimilation) [Carton *et al.*, 2000, 2008] reanalysis and NCEP GODAS (Global Ocean Data Assimilation System) reanalysis except for the first 10 years of SODA reanalysis, which have higher uncertainty due to the lack of subsurface observations.

Due to the lack of subsurface assimilation, $t300$ index of *oda_all* is not as well reconstructed as those of *cda_all* and *ada_all*, which both have the surface air temperature to force the SST as well as wind observations to drive the ocean transport. In a series of ADA experiments from *ada_all* to *ada_37* shown in Figure 5.9, the correlation of $t300$ index with *cda_all* and observation decreases when the assimilation boundary moves poleward. The similarity between Nino3.4 and $t300$ is expected since the heat content is usually a prerequisite for the occurrence of ENSO events, and there is always overshoot of the heat content to the opposite sign after ENSO events.

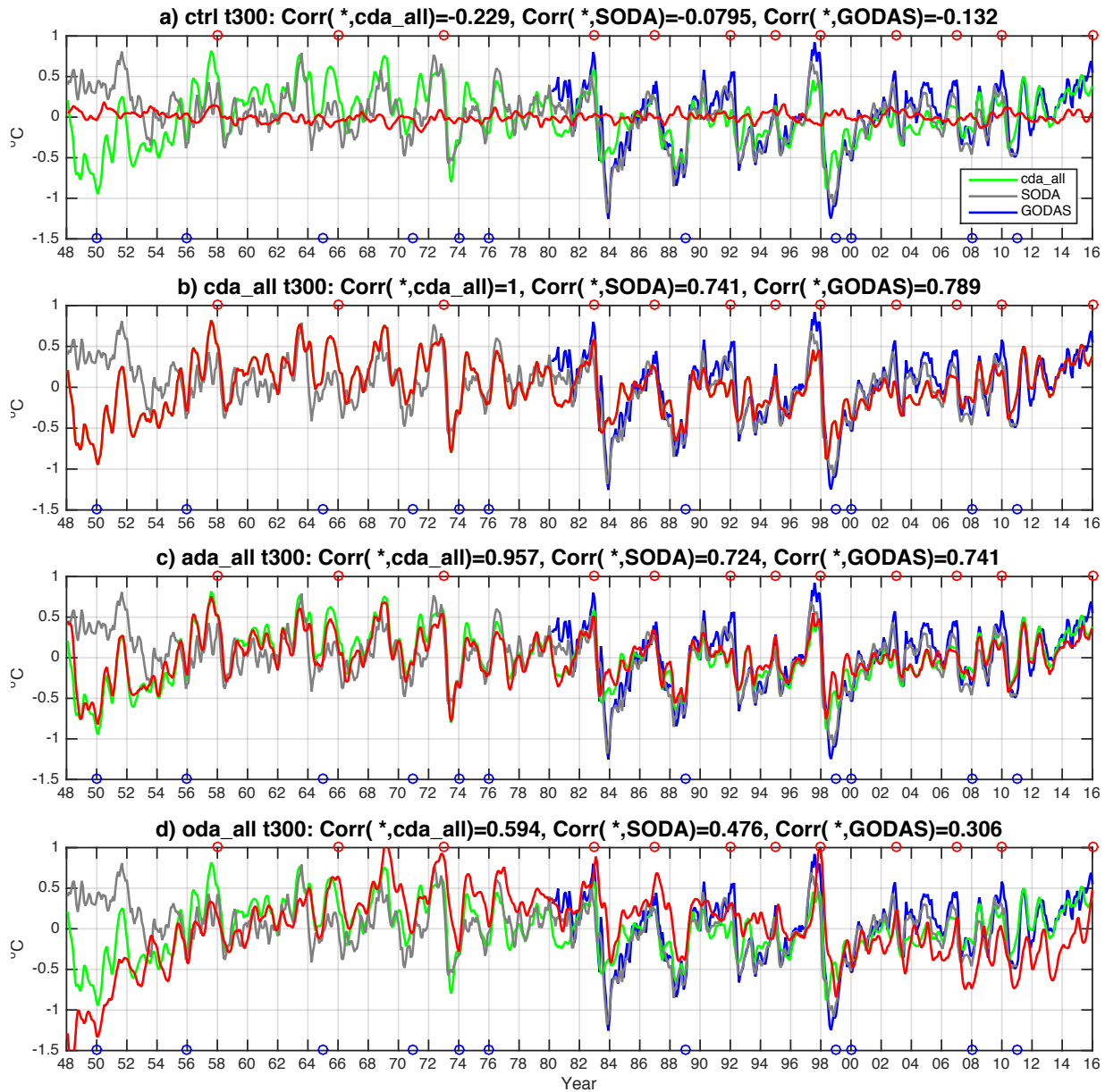


Figure 5.8 Equatorial Pacific (5°S - 5°N , 120°E - 80°W) zonal-mean 0-300m average temperature (t_{300}) time series of (a) *ctrl*, (b) *cda_all*, (c) *ada_all* and (d) *oda_all*, red in each panel. The green, grey and blue lines are t_{300} of *cda_all*, SODA and GODAS respectively. Linear trends are removed from all t_{300} time series.

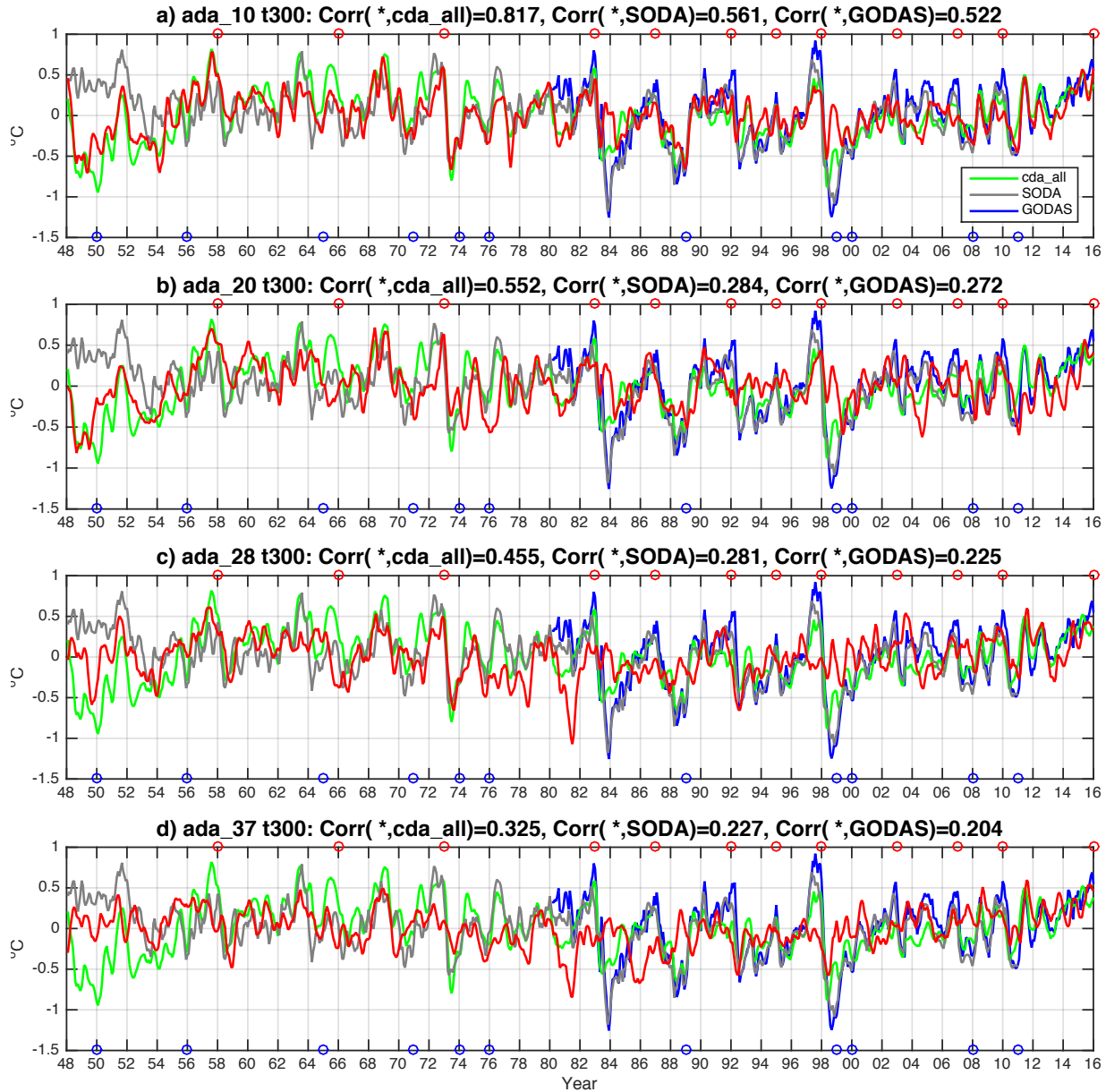


Figure 5.9 Same as Figure 5.8, but for (a) *ada_10*, (b) *ada_20*, (c) *ada_28* and (d) *ada_37*.

5.3. Case Studies

5.3.1. 1972-73 El Niño (Successful)

Among all the strong ENSO events reproduced in the *ADA* experiments (Figure 5.2), it is easy to spot the high accuracy of the 1972-73 El Niño in both *ada_20* and *ada_28*. In

this section, we will take a closer look at 1972-73 El Niño and investigate its triggering mechanism with additional short-term sensitivity experiments.

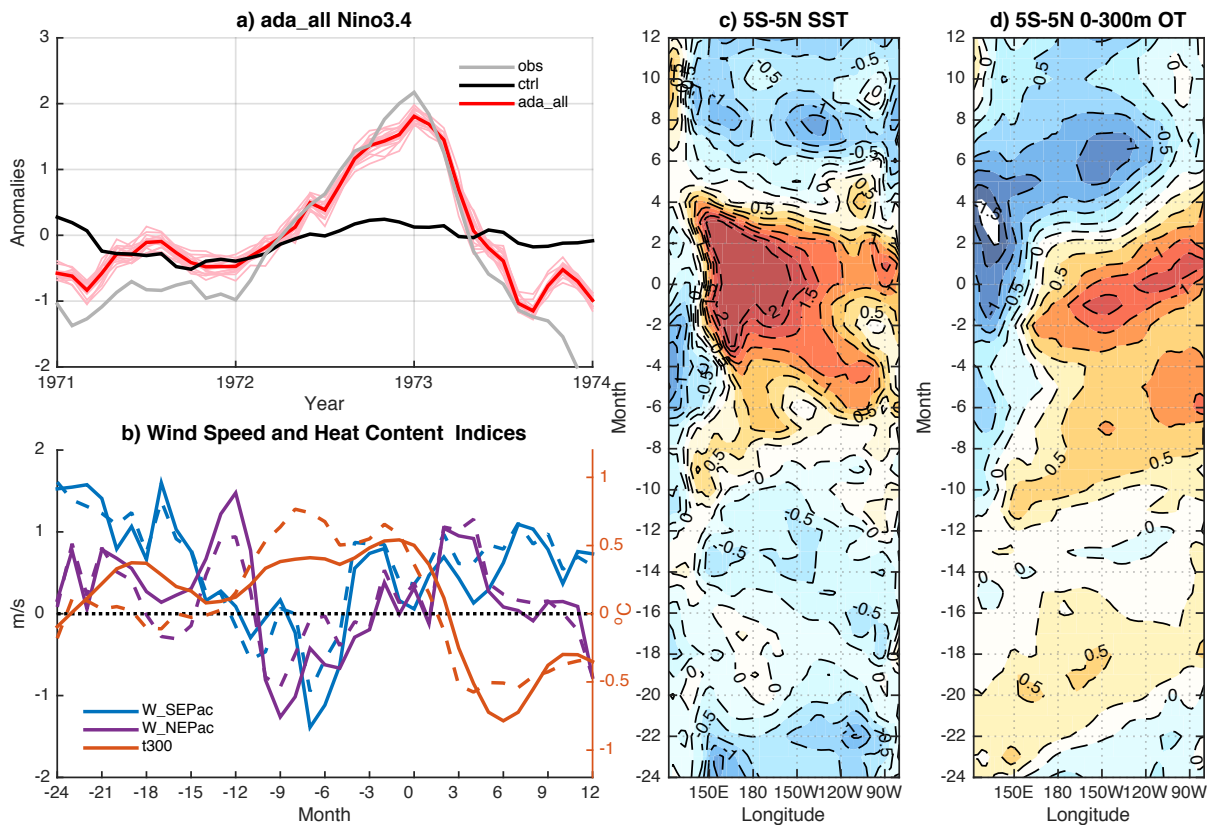


Figure 5.10 For *ada_all* in the period 1971-1973: (a) Nino3.4 index of ensemble mean (red) and all ensemble members (pink) of *ada_all*, along with observation (grey) and ctrl (black); (b) W_{SEPac} (blue), W_{NEPac} (Purple) and t_{300} (orange) of *ada_all* (solid) and observation (dashed); (c) evolution of equatorial (5°S-5°N) Pacific SST in *ada_all*; (d) evolution of equatorial (5°S-5°N) Pacific 0-300m average ocean temperature.

In *ada_all*, the Nino3.4 index is almost identical to the observation from the spring of 1972 all the way to the fall of 1973 (Figure 5.10a). Three indices in the same period are shown in Figure 5.10b, including t_{300} and two wind speed indices W_{SEPac} and W_{NEPac} . W_{SEPac} is the average low-level wind speed in the southeastern tropical Pacific (15°S-25°S, 80°W-110°W, bottom 3 levels), and W_{NEPac} the average low-level wind speed in the north-central and northeastern tropical Pacific (15°N-25°N, 120°W-

180°, bottom 3 levels). W_SEPac and W_NEPac anomalies represent the anomalous events in the strength of the trade wind that are related to SPMM and NPMM, respectively. Due to the complete coverage of atmospheric observations, both W_SEPac and W_NEPac in *ada_all* closely follows the observation. The $t300$ anomaly is slightly colder than observation in 1971 and warmer in the first half of 1972, but stays close to the observation after the El Niño onset.

All three indices in Figure 5.10b favor an El Niño event in 1972 based on the analysis of Section 4.3 and previous studies of NPMM. The greatly reduced trade wind in the southeastern tropical Pacific (W_SEPac) in the summer of 1972 could initiate the WES feedback process that warms up the eastern equatorial Pacific. The equatorial Pacific upper ocean is in a recharged state in all of 1971 and 1972 (Figure 5.10d). Moreover, the NH atmospheric variability—reduced trade wind in the spring and summer of 1972 as indicated by the negative W_NEPac anomaly—also favors the development of an El Niño event [Chang *et al.*, 2007; Vimont *et al.*, 2009]. The combination of multiple favorable precursors is likely a prerequisite for the occurrence of strong ENSO events [Anderson, 2007; Lu *et al.*, 2017b], however, it's important to know the relative importance of the precursors since each precursor contributes differently to the predictability and mechanism of ENSO variability. For example, the extratropical variability and equatorial heat content both favor the development of El Niño events in the year 1972, 1997 and 2014, but they did not lead to an El Niño event in 2014 as in 1972 and 1997. Even between 1972 and 1997, previous observational studies may indicate that both extratropical and equatorial forcing played important roles, but our RCDA experiments demonstrate that the similar precursors may have different effects on triggering the El Niño events.

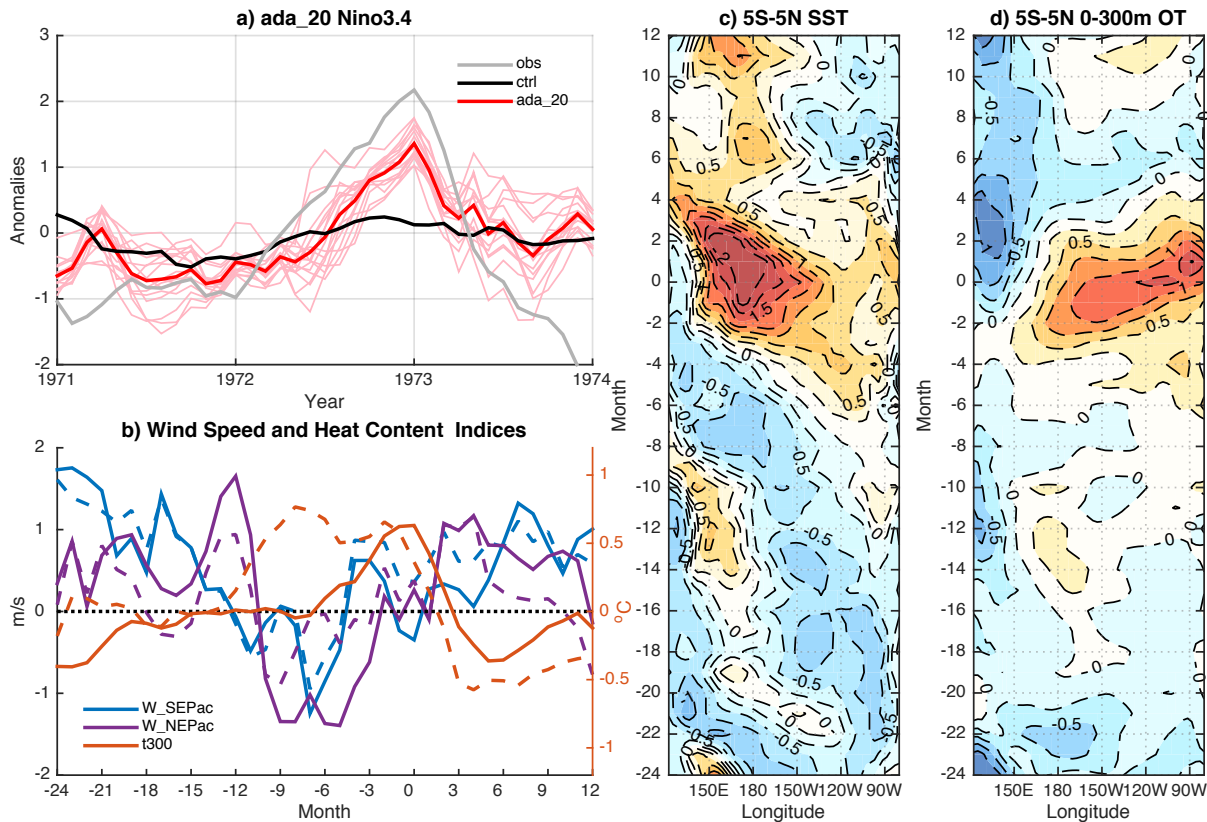


Figure 5.11 Same as Figure 5.10, but for *ada_20* in the period 1971-1973.

During the 1972-73 El Niño, *ada_20* and *ada_28* both reproduced accurate Nino3.4 variability (Figure 5.11 and Figure 5.12), and in the case of *ada_20*, the equatorial Pacific is not in a recharged state at all as in observation (Figure 5.11b and d) in more than a year leading to the El Niño onset. The lack of a recharged equatorial Pacific thermocline may be responsible for the slightly weaker warming in *ada_20* compared to *ada_all*, but the El Niño warming is still significant and thus likely caused by extratropical forcing such as *W_SEPac* and *W_NEPac* anomalies. Both *ada_20* and *ada_28* have *W_SEPac* and *W_NEPac* anomalies that closely follow the observation or *ada_all*, since the data assimilation either covers the wind speed region or is close enough to affect the atmospheric variability. The positive heat content anomaly in *ada_28*— caused by a La Nina event in 1971—results in stronger warming of the Nino3.4 index than *ada_20*.

Regardless of the state of the equatorial thermocline, the forced El Niño events in both *ada_20* and *ada_28* indicate extratropical atmospheric variability as the main trigger for the 1972-73 El Niño.

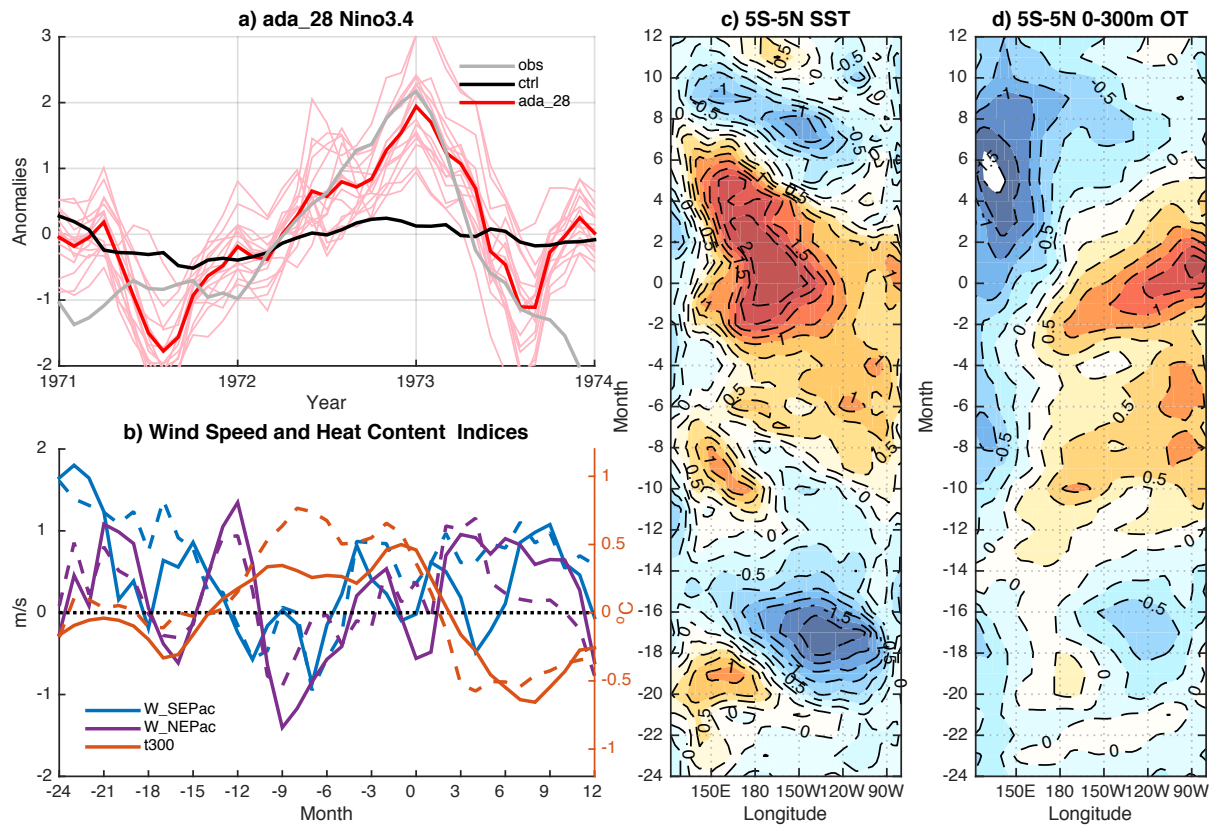


Figure 5.12 Same as Figure 5.10, but for *ada_28* in the period 1971-1973.

The surface conditions—including monthly SST and wind anomalies—from March to November of 1972 are shown in Figure 5.13. The reduced trade wind and accompanied warm SST anomalies in the north-central tropical Pacific are persistent from April through October. Although the SST anomalies did not spread all the way in the equatorial Pacific, such wind speed anomalies could charge the equatorial thermocline through the Sverdrup transport or “trade wind charging” [Clarke *et al.*, 2007; Anderson *et al.*, 2013]. In the meantime, the WES feedback process from the southeastern tropical Pacific starts from June and propagates SST anomalies into the eastern equatorial Pacific in August

and September, which is joined by the SST warming caused by the surfacing of the eastward-propagating heat content anomaly (Figure 5.12d) and becomes a strong El Niño.

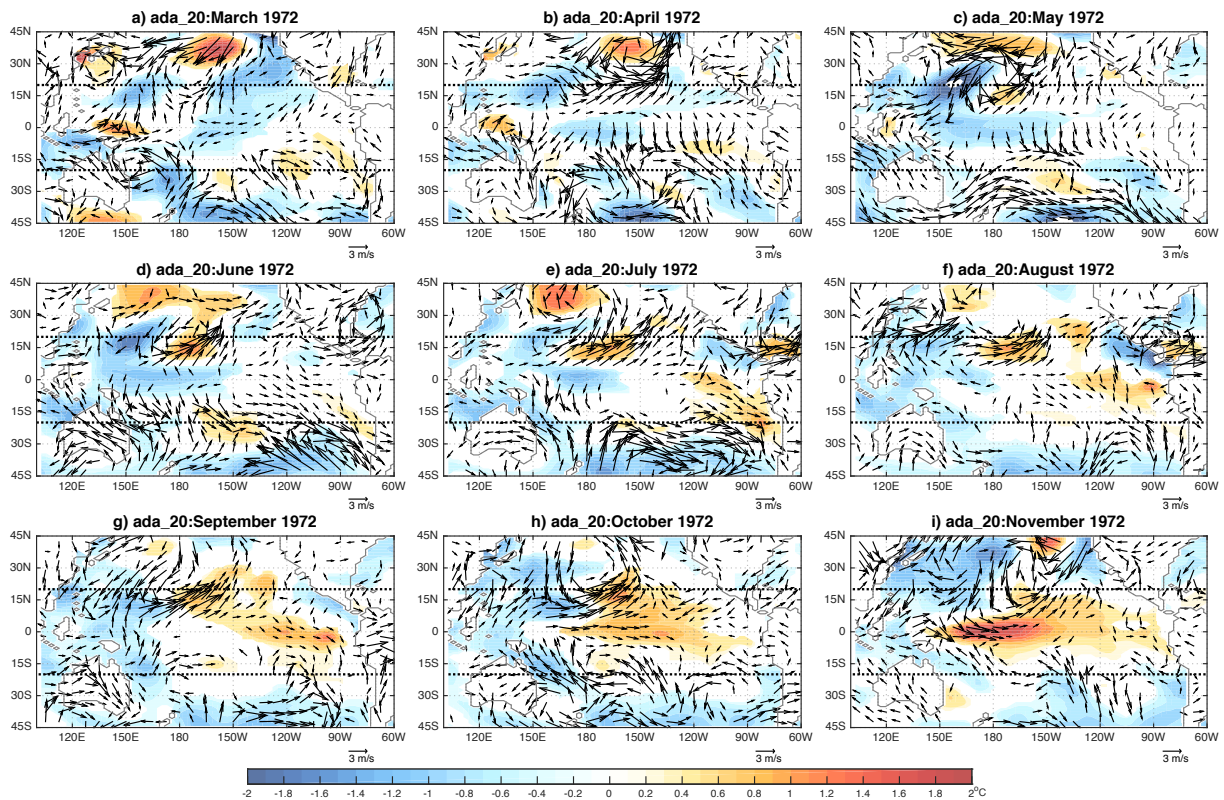


Figure 5.13 Composites of anomalous monthly SST (shadings) and wind (arrows) from March 1972 to November 1972 in *ada_20*. Black dotted lines indicate the boundary of data assimilation. SST and wind anomalies are only shown where the composite exceed twice the standard deviation of *ctrl* (CTRL_SD as described in Section 4.2.1).

To further test the extratropical atmospheric precursors for the 1972-73 El Niño, additional short experiments (No.1-4 in Table 5.2) are performed with modified initial conditions (IC) or observations. The first such experiment, listed as No.1 in Table 5.2 and shown in Figure 5.14 and Figure 5.15, is a 2-year *ada_20* experiment from the start of 1972, but with the ocean IC from the start of 1976. Otherwise, it is identical to the 1972-1973 period of the original *ada_20* experiment, including the same atmospheric observations and atmosphere IC. The 1976 ocean IC are chosen because t_{300} is very low

at the start of 1976. The ENSO variability following a discharged equatorial Pacific thermocline while forced with favorable extratropical atmospheric variability could demonstrate the relative importance of the precursors.

No.	Period	RCDA	Atm Obs	Atm IC	Ocn IC
1	1972-73	<i>ada_20</i>	1972-73	1972	1976
2	1972-73	<i>ada_20</i>	1972-73 (30-day running average)	1972	1972
3	1972-73	<i>ada_20</i>	1972-73 (30-day running-averaged anomalies removed)	1972	1972
4	1972-73	<i>ada_20</i>	1972-73	1972	1997
5	1997-98	<i>ada_20</i>	1997-98	1997	1972
6	1972-73	<i>ada_28</i>	1972-73	1972	1997
7	1997-98	<i>ada_28</i>	1997-98	1997	1972

Table 5.2 List of the short experiments used in Chapter 5. The modified aspects of the experiments that are different from the original RCDA experiments are bold.

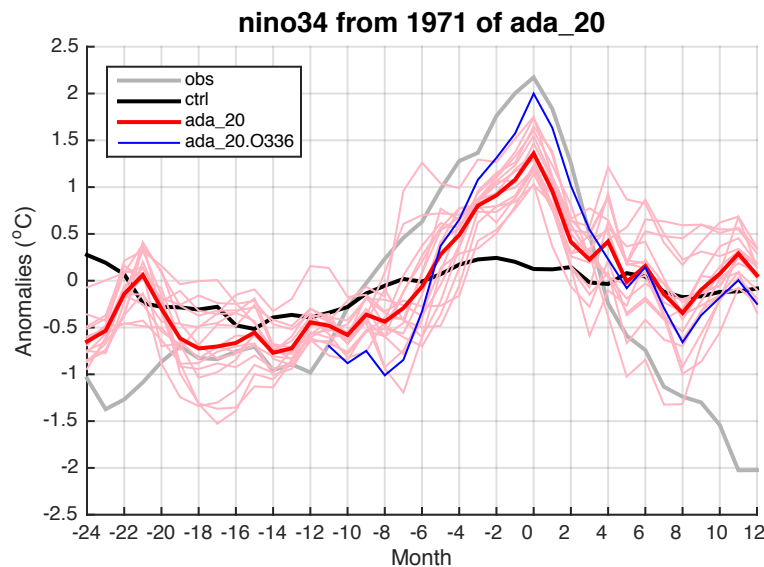
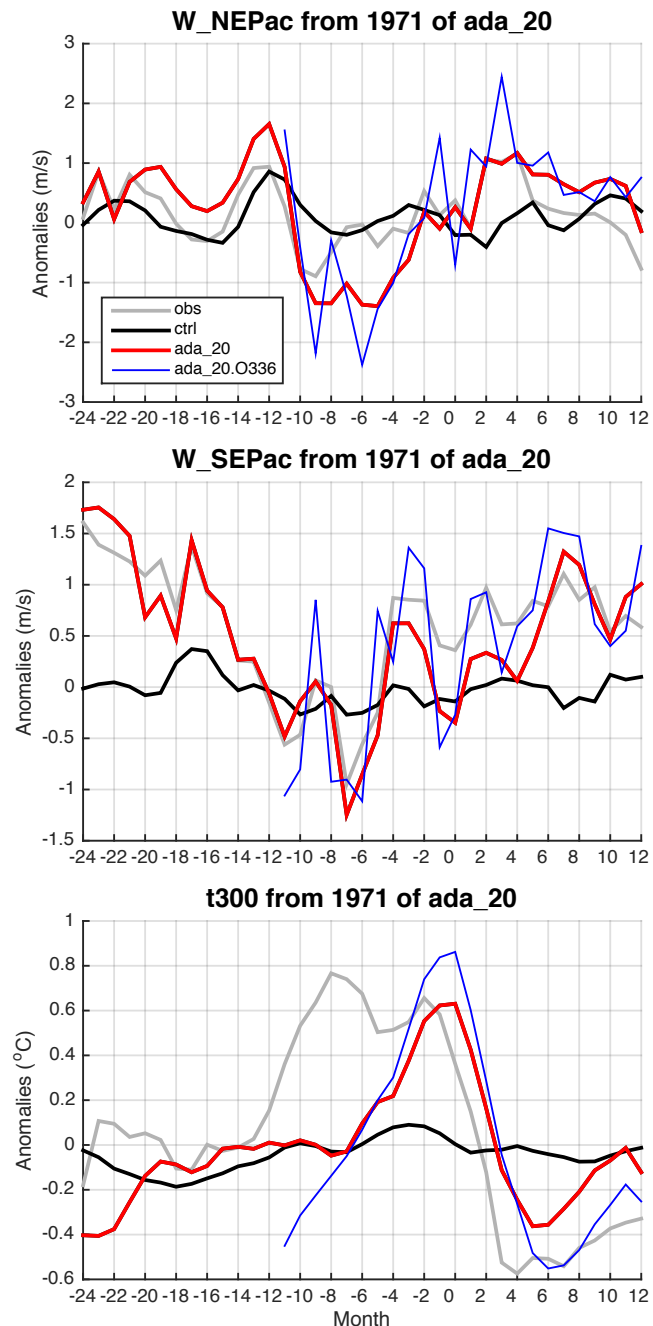


Figure 5.14 Same as Figure 5.11a, with the addition of the Nino3.4 index from short experiment No.1 (blue). The grey, black, red and pink lines are observation, *ctrl*, original ensemble mean and ensemble members, respectively.

The Nino3.4 index in short experiment No.1 rises higher than the original 1972-73 El Niño in *ada_20* (Figure 5.14), despite the initial dip due to the initial negative t_{300} anomaly (Figure 5.15). As shown in Figure 5.15, the extratropical wind anomalies, represented by W_{NEPac} and W_{SEPac} , still start from and follow those from observation or the original *ada_20*, while t_{300} starts from a much lower initial value, but quickly rises to the same as the original *ada_20* in less than 6 months.

Short experiment No.1 demonstrates that even with a discharged equatorial Pacific, an El Niño event could still be triggered with extratropical atmospheric forcing. We can safely assume that without the wind anomalies from both NH and SH extratropics, there won't be such an El Niño event.

Figure 5.15 Same as Figure 5.14, but for W_{NEPac} , W_{SEPac} and t_{300} instead of Nino3.4 index, and without individual ensemble members.



The wind anomalies analyzed so far are monthly values, and we are mostly focusing on their low-frequency variability. The actual daily atmospheric observations that are

assimilated should have a lot of high-frequency variability. The daily, weekly and monthly time series of $W_SE\text{Pac}$ in 1972 are shown in Figure 5.16. The $W_SE\text{Pac}$ time series have very large variance at high frequency, with extreme events lasting one to a few days every one to two weeks, which is typical of the mid-latitude synoptic variability. The high-frequency variability is modulated by the monthly variability, resulting in more extreme events with reduced trade wind from April to June 1972. The low-frequency variability could be caused by teleconnection with the Pacific-South America (PSA) Pattern, SST variability, or just synoptic noise.

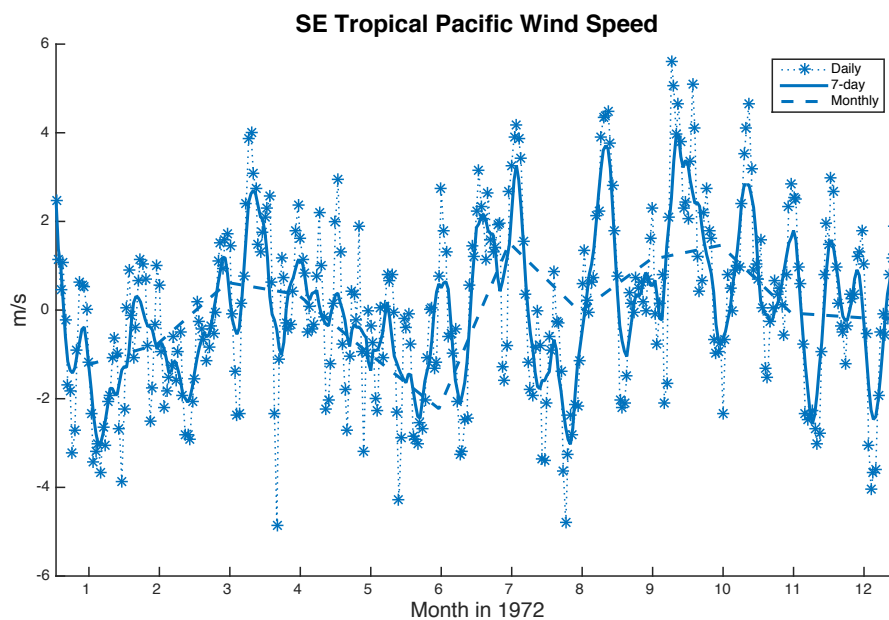


Figure 5.16 Observed daily (asterisk with dotted line), weekly (solid line) and monthly (dashed line) $W_SE\text{Pac}$ anomalies in 1972.

It turns out that the low-frequency variability is more important for triggering ENSO events. In short experiment No.2, a 2-year experiment starts from the ensemble atmosphere and ocean IC at the start of 1972 of ada_20 , but a 30-day running average is performed on the atmospheric observations. With the high-frequency extreme events removed but low-frequency variability retained, the resulting El Niño event ends up much

stronger than the original 1972-73 El Niño (Figure 5.17). Without the high-frequency variability, the more persistent forcing from the reduced trade wind, albeit weaker in extreme values, is much more effective in triggering a strong El Niño event. Another short experiment with 7-day-running-averaged observations (not shown) also produces an stronger El Niño event than the original *ada_20*. In contrast to No.2, short experiment No.3 removes the 30-day running-averaged anomalies—the low frequency wind forcing retained in No.2—from the atmospheric observations. The removal of low-frequency wind anomalies leads to a neutral Nino3.4 index and eliminates the El Niño event all together.

Figure 5.17 Same as Figure 5.11a, with the addition of the Nino3.4 index from short experiment No.2 (blue).

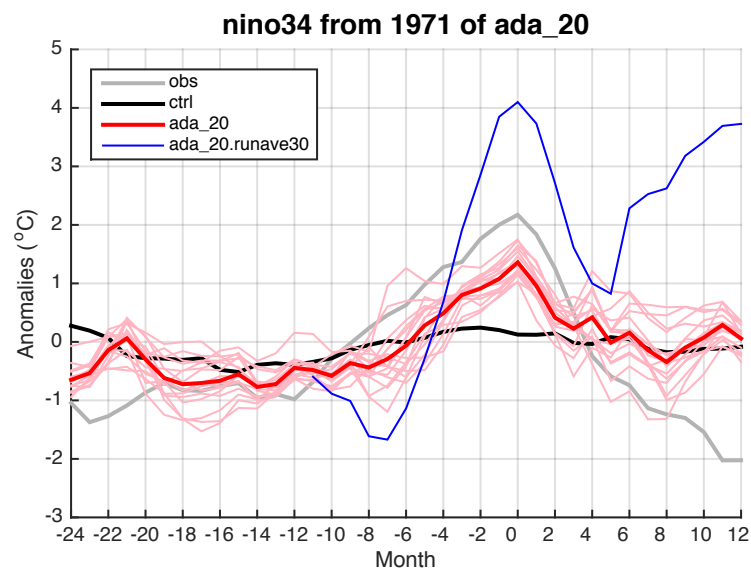
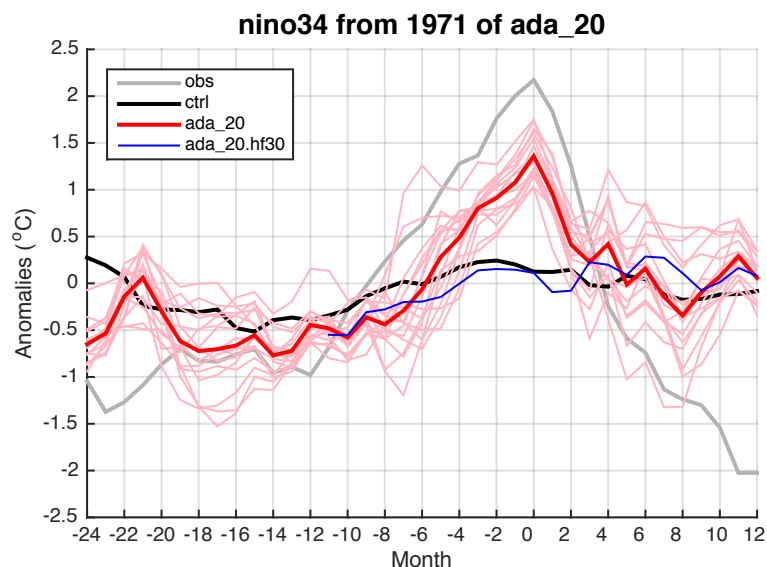


Figure 5.18 Same as Figure 5.11a, with the addition of the Nino3.4 index from short experiment No.3 (blue).



5.3.2. 1997-98 El Niño (Unsuccessful)

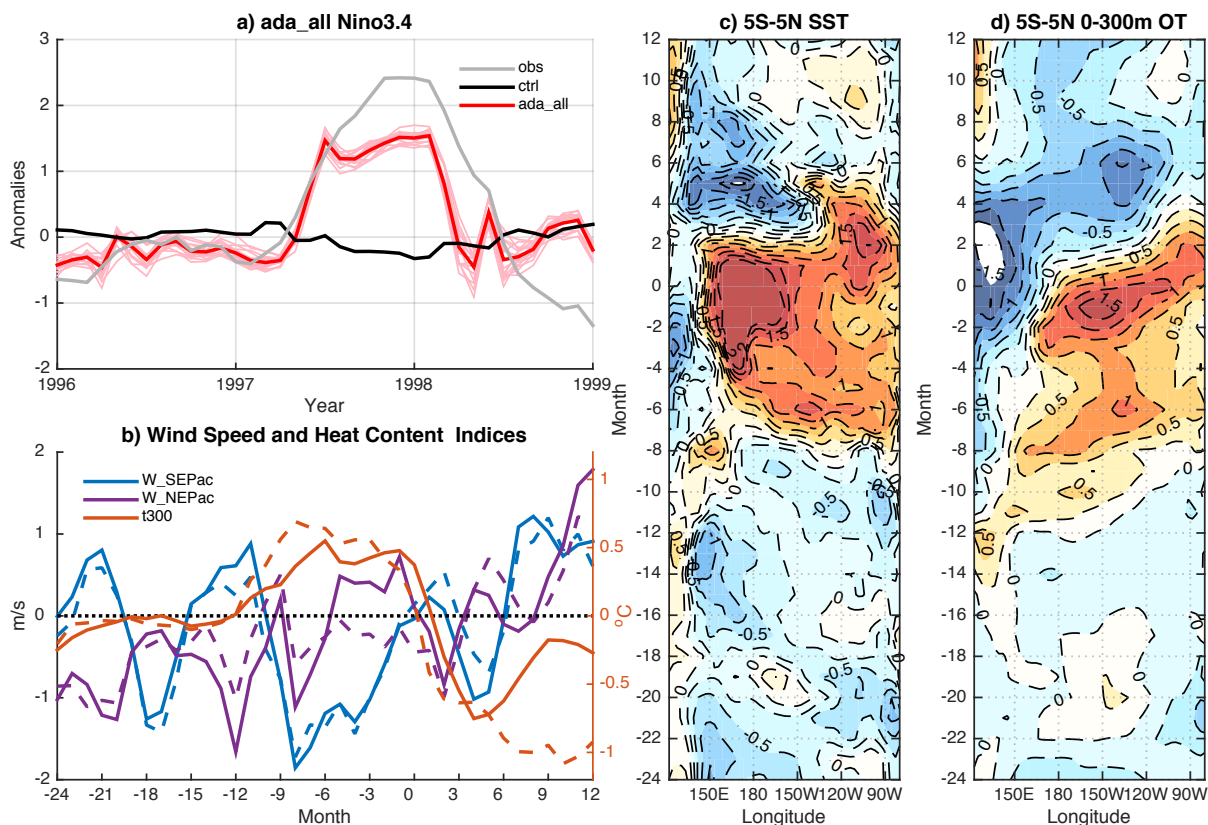


Figure 5.19 Same as Figure 5.10, but for *ada_all* in the period 1996-1998.

The reproduction of the 1997-98 El Niño in the RCDA experiments is much worse than that of the 1972-73 El Niño, despite being one of the strongest ENSO events in history and preceded by favorable NPM conditions [Chang *et al.*, 2007]. Even in *ada_all* as shown in Figure 5.19, the Nino3.4 index only reaches 1.5°C, compared to the observed peak of 2.5°C. The initial warming in the early summer of 1997 is as rapid as the observation, which follows the extreme event of reduced trade wind in the southeastern tropical Pacific. However, the equatorial heat content does not reach the observed value, especially the eastward propagation of heat content anomaly from the western Pacific. The lack of positive heat content anomalies could be responsible for the plateauing of the El Niño warming in *ada_all*, since the 1997-98 El Niño was preceded by many strong MJO and

WWB events, which produced large heat content anomalies that contributed to one of the strongest El Niño in the observed history [McPhaden, 1999; Vecchi *et al.*, 2000]. Due to the coarse resolution of the atmosphere component and other model deficiencies, FOAM is unable to simulate high-frequency and/or small-scale phenomena like MJO and WWB, which could explain the lack of positive heat content anomalies even in *ada_all*. Weak instability in the coupled equatorial Pacific coupled system could also be a reason for the weak 1997-98 El Niño, since the overall strength of ENSO variability is weaker in FOAM than in observation.

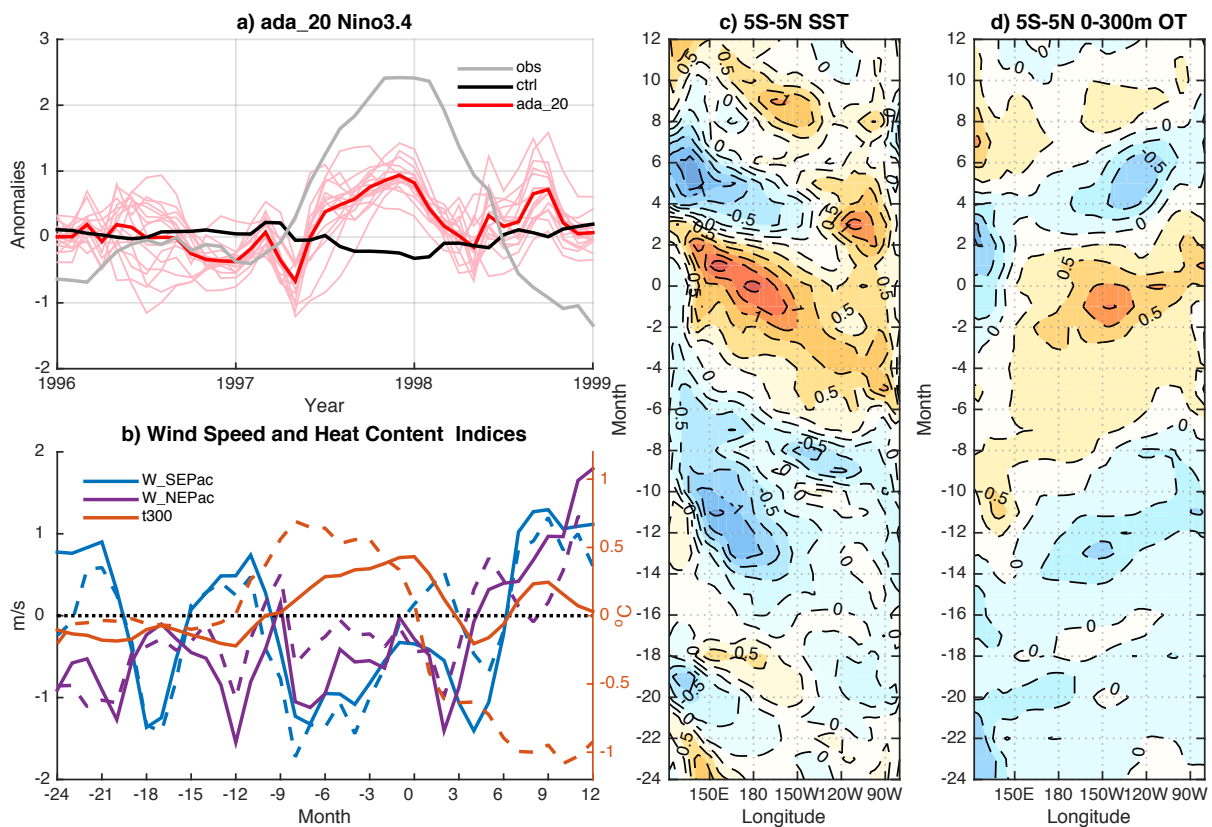


Figure 5.20 Same as Figure 5.10, but for *ada_20* in the period 1996-1998.

The large negative anomalies of W_{NEPac} in early 1997 and W_{SEPac} in summer 1997 make the unsuccessful reproduction of the 1997-98 El Niño in *ada_all* even more intriguing, since the equatorial Pacific is not as recharged as the observation before the

1972-73 El Niño either. The extratropical atmospheric forcing, primarily in the form of trade wind anomalies, is enough to produce enough warming for the 1972-73 El Niño, but insufficient for the 1997-98 El Niño. This contrast can be further demonstrated by the *ada_20* (Figure 5.20) and *ada_28* (Figure 5.21) experiments. Both trade wind speed indices W_NEPac and W_SEPac still follow the observed variability like *ada_all* because of the available subtropical and extratropical data assimilation, but these wind speed anomalies, despite similar strength to those in 1972, fail to produce a strong El Niño event. The Nino3.4 index even become negative from summer of 1997 through 1998.

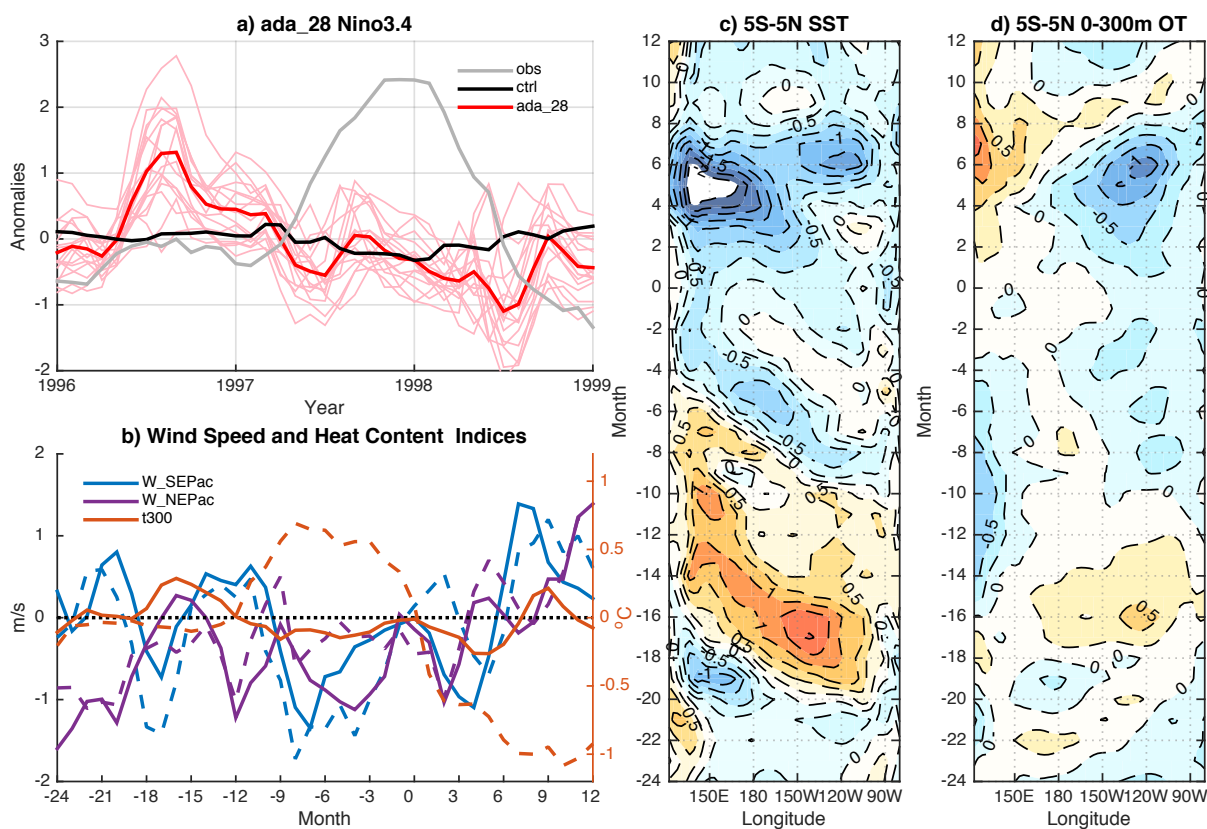


Figure 5.21 Same as Figure 5.10, but for *ada_28* in the period 1996-1998.

5.3.3. Comparison of 1972-73 El Niño and 1997-98 El Niño

The contrast between the 1972-73 and 1997-98 El Niño events are further examined. With the ocean IC from 1997, short experiment No.4 still reproduces the observed 1972-

73 El Niño by assimilating atmospheric observations poleward of 20° (Figure 5.22). The slight negative t_{300} index at the start of 1997 (Figure 5.20b) does not affect the onset of the 1972-73 El Niño, which is expected considering that the more negative t_{300} at the start of 1976 does not prevent the onset either (Figure 5.14 and Figure 5.15).

On the contrary, with the ocean IC from 1972, short experiment No.5 produces similar Nino3.4 index as the 1997-98 period of the original *ada_20* (Figure 5.23). The stronger warming is caused by the positive t_{300} at the start of 1972 replacing the negative one at the start of 1997, but this stronger initial warming does not significantly increase the subsequent warming and the peak Nino3.4 index.

Figure 5.22 Same as Figure 5.11a, with the addition of the Nino3.4 index from short experiment No.4 (blue).

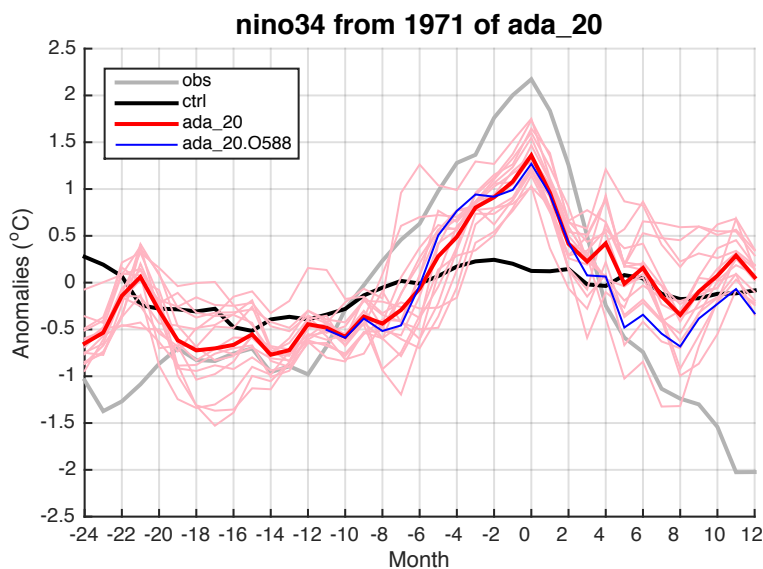
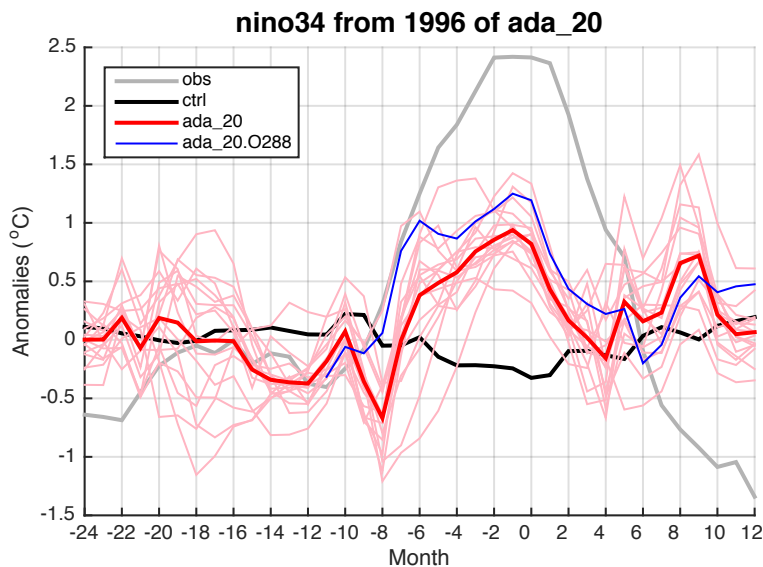


Figure 5.23 Same as Figure 5.20a, with the addition of the Nino3.4 index from short experiment No.5 (blue).



The same pair of short experiments as No.4 and 5 are also performed based on the *ada_28* experiment as No.6 (Figure 5.24) and 7 (Figure 5.25). In *ada_28*, there is a large gap between the oceanic conditions at the start of 1972 and 1997. The equatorial Pacific is in a recharged state in 1972 (Figure 5.12d), but in a neutral or discharged state in 1997 of *ada_28* (Figure 5.21d). By swapping the ocean IC from 1972 and 1997, the El Niño warming of short experiment No.5 is initially suppressed in early 1972 (Figure 5.24), while triggered in early 1997 (Figure 5.25). However, after the initial period, the trends of Nino3.4 index mostly follow those from the original *ada_28* experiment during the

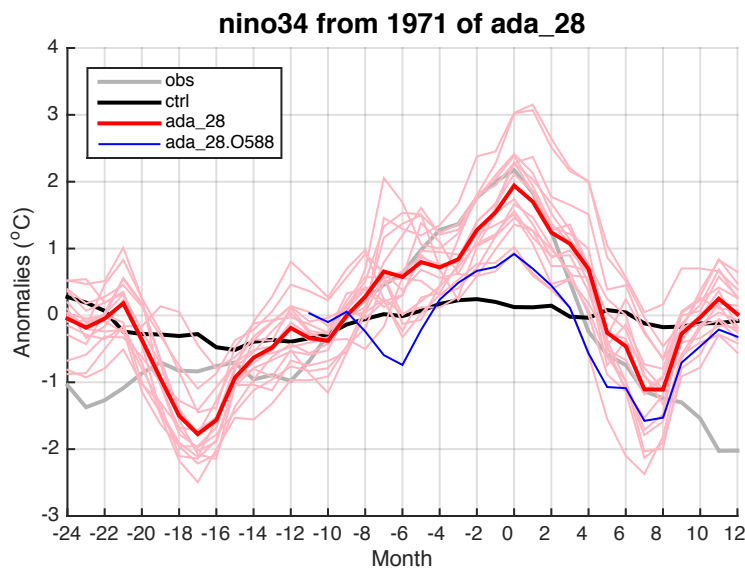
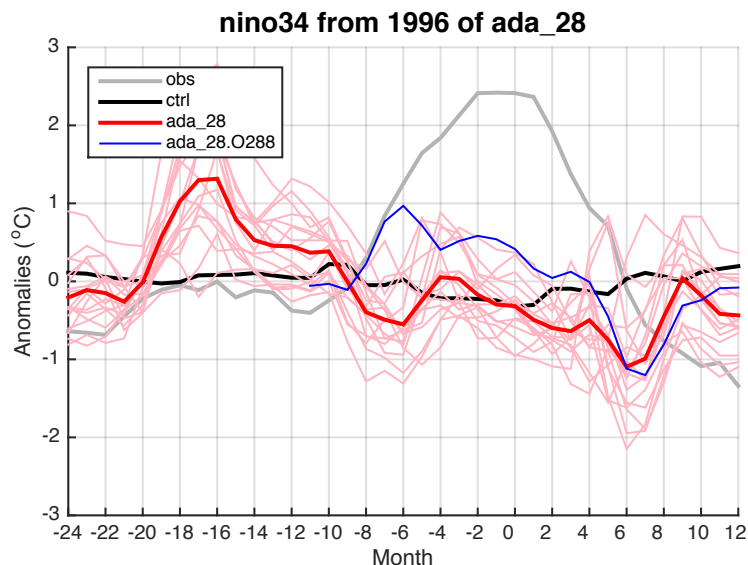


Figure 5.24 Same as Figure 5.12a, with the addition of the Nino3.4 index from short experiment No.6 (blue).

Figure 5.25 Same as Figure 5.21a, with the addition of the Nino3.4 index from short experiment No.7 (blue).



growing phase of the ENSO variability, up from summer 1972 to produce a weak El Niño event in No.6 while down to become neutral from summer 1997 in No.7.

Chapter 4, along with previous modeling and observational studies, has established that favorable extratropical atmospheric forcing and equatorial oceanic preconditioning are both needed to produce strong ENSO events, so it is no surprise to see that both the 1972-73 and 1997-98 El Niño events are preceded by these favorable precursors. However, the existence of the precursors does not mean that each of them has the same function for every El Niño event. On the contrary, the comparison between the 1972-73 and 1997-98 El Niño events in RCDA experiments such as *ada_20* and *ada_28* suggests that the more critical trigger is the extratropical atmospheric forcing for the former and the equatorial preconditioning for the latter.

We speculate the difference between the 1972-73 and 1997-98 El Niño events in the RCDA experiments could be explained by two reasons. First, the equatorial oceanic preconditioning could simply have more contribution to the 1997-98 El Niño, so that the lack of it has a larger effect on the magnitude of the event. The weaker 1972-73 El Niño in *ada_20* compared to *ada_all* and *ada_28* could also be related to the lack of oceanic preconditioning, but the larger contribution from extratropical atmospheric forcing mitigates the loss of equatorial preconditioning. Second, the timing of the precursors could also play a role. The W_NEPac anomalies, which could recharge the western and central equatorial Pacific, exist primarily in the spring of 1972 and the winter of 1996, and this difference could change the equatorial heat content in the summer and fall when the El Niño is developing.

5.4. Summary and Discussion of Chapter 5

In this chapter, real world reanalysis data are assimilated with the RCDA method in FOAM to systematically and quantitatively study the precursors of historical ENSO events, the extratropical atmospheric control on ENSO onset. The RCDA experiments

demonstrate clear extratropical control within the model dynamics of FOAM, although the control is expectedly weaker than in the perfect-model RCDA experiments. For example, the correlation of Nino3.4 index with observation is about 0.5 in *ada_20*, while it is over 0.8 in the perfect-model framework. The decrease from perfect-model to real-world experiments could be explained mostly by the introduction of model bias. A correlation of 0.5 is still significant and proves a causal extratropical-to-tropical teleconnection.

The introduction of model bias by assimilating reanalysis data into FOAM leads to some caveats in this study. Here we will discuss the caveats, in the order of increasing significance. First, the model bias directly impacts the quality of the data assimilation. Thus, the analysis is still biased compared to the observation as in the case of *cda_all*, and the ensemble spread tends to be too small to represent the uncertainty of the model. Second, the model does not include all the possible mechanisms that could facilitate extratropical-to-tropical teleconnections, while the current mechanisms could also have the wrong strength or physics. Third, and most importantly, the model climatology and annual cycle are still heavily biased in the regions without assimilation. Since the ENSO variability is highly connected with the tropical climatology and annual cycle [Guilyardi, 2005; Liu et al., 2014c], such biases could result in biased ENSO variability such as the wrong phase-locking, which makes it harder to analysis ENSO mechanisms and precursors. The perfect-model study in Chapter 4 showed the model dynamics of FOAM and mitigated the impact of model bias on the analysis in Chapter 5. However, there are still model-specific aspects in the conclusions here, so one should take caution when applying the results to observation or other models.

Chapter 6

6. Summary

6.1. Summary

In this dissertation, we systematically studied the extratropical influence on tropical climatology and variability. The RCDA method, based on the coupled data assimilation system in a CGCM, is proposed that enable us to study the extratropical-to-tropical teleconnections systematically and quantitatively. Both the ITCZ position and the ENSO variability are demonstrated to be causally connected to the extratropical climate.

The RCDA experiments in FOAM showed that the tropical asymmetry bias in precipitation and surface temperature can be caused significantly by extratropical processes, with contributions from both the subtropics and mid-to-high latitudes. The extratropical climate changes the cross-equator AET and in turn the tropical climate asymmetry. This extratropical impact on tropical climatology seems to be accomplished through a combination of atmospheric teleconnection, ocean dynamics, and coupled processes. In contrast, the bias of insufficient equatorial precipitation is caused mainly by local tropical processes. The equatorial precipitation is closely related to the net energy input into the equatorial atmosphere, and the bias is only reduced when the data assimilation is active in the deep tropics. Our study suggests that, to improve tropical climate bias, it is essential to consider the fully coupled ocean-atmosphere system, and it is equally important to improve both the extratropics and tropics of climate models.

The RCDA experiments also demonstrated significant control of extratropical atmospheric forcing on ENSO variability. First in a perfect-model setup in FOAM, when

atmospheric “observations” are assimilated only poleward of 20° in both hemispheres, most ENSO events in the “observation” are reproduced and the correlation of the Nino3.4 index with the “observed” index is 0.89 compared to 0.2 in the ensemble control experiment that does not assimilate any observations. Further experiments with the assimilation in each hemisphere show that the forced ENSO variability is contributed roughly equally by the Southern and Northern Hemisphere extratropical atmosphere. Further analyses of the ENSO events in the southern hemisphere forcing experiment reveal robust precursors in both the extratropical atmosphere over southeastern Pacific and the equatorial Pacific thermocline, consistent with previous studies of the South Pacific Meridional Mode and the discharge—recharge paradigm, respectively. However, composite analyses based on each precursor show that neither precursor alone is sufficient to trigger ENSO onset by itself and therefore neither alone could serve as a reliable predictor. Additional experiments with northern hemisphere forcing, ocean assimilation or different assimilation boundaries are also performed. Contrary to the extratropical control on tropical climatology, the subtropical and extratropical ocean has no control on the seasonal and interannual variability in the tropics.

Moving onto real world reanalysis data, the RCDA experiments still demonstrated clear extratropical control on ENSO variability by correctly triggering certain historical ENSO events, although the control is weaker than in the perfect-model study. For example, the perfect-model `ada_20` experiment reproduced most of the “observed” ENSO events, while the real-world counterpart reproduced about half of the events with less accuracy. However, the accurate triggering of only certain historical ENSO events in RCDA experiments is already an improved determination of causality of extratropical control on ENSO variability compared to most previous observational and modeling

studies. The analysis of two representative events, the 1972-73 El Niño and the 1997-98 El Niño, shows that the known precursors may have varying importance in triggering different events. Although both favorable extratropical atmospheric variability and equatorial oceanic preconditioning are found before all the strongest El Niño events, the extratropical precursor seems more important to the 1972-72 El Niño, while the equatorial preconditioning seems critical for the 1997-98 El Niño.

6.2. Possibilities for Future Research

This dissertation work introduced the RCDA method and applied it to the extratropical control on tropical climatology and variability. There are still a lot to be explored, both in terms of using data assimilation to study climate dynamics and the extratropical-to-tropical teleconnections.

Coupled data assimilation has been shown to be a powerful tool to study both synoptic and climate dynamics. It has even more potential as a tool to diagnose model errors. The ensemble-based assimilation methods even have built-in model ensemble to account for the uncertainty in model dynamics or parameterization schemes.

The RCDA could also be applied to study other climate teleconnections. A simple extension of this dissertation work would be to zonally limit the data assimilation and study the impact of the Atlantic or Indian Ocean on tropical Pacific climatology and ENSO variability. Or more generally, the RCDA method could be used to test the interaction between the climatology or variability of different ocean basins.

Perfect-model study like Chapter 4 could be very informative, although the RCDA method could use real world observations. Without the complication of model bias, the research subject can be investigated in great details within the scope of the model dynamics. For example, the extratropical atmospheric forcing from the two hemispheres

could be further studies by comparing single-hemisphere RCDA experiments. Such analysis could be very difficult with real world observations, since the forcing signal from each hemisphere may be too small to detect with the additional noises from model bias. A perfect-model study using the RCDA method in a high-resolution state-of-the-art CGCM, which has more realistic features like tropical climatology, annual cycle and ENSO diversity, will be immensely valuable to our understanding of all aspects of the ENSO phenomenon.

It goes without saying that a high-resolution state-of-the-art CGCM would also greatly benefit real-world applications like Chapter 5. The ability to resolve MJO and WWB events could help further qualify the contributions from different precursors. The diversity of ENSO events has drawn a lot of attention recently. A CGCM with realistic ENSO diversity could also be used to study the difference between Central-Pacific and Eastern-Pacific ENSO events in terms of precursors and mechanisms.

Besides the precursors, other aspects of the ENSO variability, such as the phase-locking, spring prediction barrier and interaction with equatorial annual cycle, are all important and interesting topics that could be explored with the RCDA method. Creative applications of the RCDA method to these topics may greatly augment the current modeling and observational studies.

References

- Adam, O., T. Schneider, F. Brient, and T. Bischoff (2016), Relation of the double-ITCZ bias to the atmospheric energy budget in climate models, *Geophys. Res. Lett.*, doi:10.1002/2016GL069465.
- Alexander, M. a., I. Bladé, M. Newman, J. R. Lanzante, N. C. Lau, and J. D. Scott (2002), The atmospheric bridge: The influence of ENSO teleconnections on air-sea interaction over the global oceans, *J. Clim.*, 15(16), 2205–2231, doi:10.1175/1520-0442(2002)015<2205:TABTIO>2.0.CO;2.
- Anderson, B. T. (2007), On the joint role of subtropical atmospheric variability and equatorial subsurface heat content anomalies in initiating the onset of ENSO events, *J. Clim.*, 20(8), 1593–1599, doi:10.1175/JCLI4075.1.
- Anderson, B. T., and R. C. Perez (2015), ENSO and non-ENSO induced charging and discharging of the equatorial Pacific, *Clim. Dyn.*, 45(9–10), 2309–2327, doi:10.1007/s00382-015-2472-x.
- Anderson, B. T., R. C. Perez, and A. Karspeck (2013), Triggering of El Niño onset through trade wind-induced charging of the equatorial Pacific, *Geophys. Res. Lett.*, 40(6), 1212–1216, doi:10.1002/grl.50200.
- Anderson, J. L. (2001), An ensemble adjustment Kalman filter for data assimilation, *Mon. Weather Rev.*, 129(12), 2884–2903.
- Anderson, J. L. (2003), A local least squares framework for ensemble filtering, *Mon. Weather Rev.*, 131(4), 634–642.
- Barsugli, J. J., and D. S. Battisti (1998), The basic effects of atmosphere-ocean thermal coupling on midlatitude variability, *J. Atmos. Sci.*, 55(4), 477–493, doi:Doi

10.1175/1520-0469(1998)055<0477:Tbeoao>2.0.Co;2.

Bellenger, H., E. Guilyardi, J. Leloup, M. Lengaigne, and J. Vialard (2014), ENSO representation in climate models: from CMIP3 to CMIP5, *Clim. Dyn.*, *42*(7–8), 1999–2018, doi:10.1007/s00382-013-1783-z.

Bischoff, T., and T. Schneider (2014), Energetic constraints on the position of the intertropical convergence zone, *J. Clim.*, *27*(13), 4937–4951, doi:10.1175/JCLI_D_13_00650.1.

Bloom, S. C., L. L. Takacs, A. M. da Silva, and D. Ledvina (1996), Data Assimilation Using Incremental Analysis Updates, *Mon. Weather Rev.*, *124*(6), 1256–1271, doi:10.1175/1520-0493(1996)124<1256:DAUIAU>2.0.CO;2.

Broccoli, A. J., K. A. Dahl, and R. J. Stouffer (2006), Response of the ITCZ to Northern Hemisphere cooling, *Geophys. Res. Lett.*, *33*(1), n/a-n/a, doi:10.1029/2005GL024546.

Cane, M. A., and S. E. Zebiak (1985), A theory for el nino and the southern oscillation., *Science*, *228*(4703), 1085–7, doi:10.1126/science.228.4703.1085.

Cane, M. A., S. E. Zebiak, and S. C. Dolan (1986), Experimental forecasts of El Niño, *Nature*, *321*(6073), 827–832, doi:10.1038/321827a0.

Carton, J. A., G. Chepurin, X. Cao, B. Giese, J. A. Carton, G. Chepurin, X. Cao, and B. Giese (2000), A Simple Ocean Data Assimilation Analysis of the Global Upper Ocean 1950–95. Part I: Methodology, *J. Phys. Oceanogr.*, *30*(2), 294–309, doi:10.1175/1520-0485(2000)030<0294:ASODAA>2.0.CO;2.

Carton, J. A., B. S. Giese, J. A. Carton, and B. S. Giese (2008), A Reanalysis of Ocean Climate Using Simple Ocean Data Assimilation (SODA), *Mon. Weather Rev.*, *136*(8), 2999–3017, doi:10.1175/2007MWR1978.1.

- Chang, P., L. Zhang, R. Saravanan, D. J. Vimont, J. C. H. Chiang, L. Ji, H. Seidel, and M. K. Tippett (2007), Pacific meridional mode and El Niño-Southern Oscillation, *Geophys. Res. Lett.*, *34*(16), n/a-n/a, doi:10.1029/2007GL030302.
- Chen, C., M. A. Cane, A. T. Wittenberg, D. Chen, C. Chen, M. A. Cane, A. T. Wittenberg, and D. Chen (2016), ENSO in the CMIP5 simulations: lifecycles, diversity, and responses to climate change, *J. Clim.*, JCLI-D-15-0901.1, doi:10.1175/JCLI-D-15-0901.1.
- Chiang, J. C. H., and C. M. Bitz (2005), Influence of high latitude ice cover on the marine Intertropical Convergence Zone, *Clim. Dyn.*, *25*(5), 477–496, doi:10.1007/s00382-005-0040-5.
- Chiang, J. C. H., and D. J. Vimont (2004), Analogous Pacific and Atlantic Meridional Modes of Tropical Atmosphere–Ocean Variability*, *J. Clim.*, *17*(21), 4143–4158, doi:10.1175/JCLI4953.1.
- Clarke, A. J., S. Van Gorder, and G. Colantuono (2007), Wind Stress Curl and ENSO Discharge/Recharge in the Equatorial Pacific, *J. Phys. Oceanogr.*, *37*(4), 1077–1091, doi:10.1175/JPO3035.1.
- Compo, G. P., and P. D. Sardeshmukh (2010), Removing ENSO-related variations from the climate record, *J. Clim.*, *23*(8), 1957–1978, doi:10.1175/2009JCLI2735.1.
- Cox, M. D. (1984), *A primitive equation 3-dimensional model of the ocean*, GFDL–Princeton University.
- Cvijanovic, I., and J. C. H. Chiang (2013), Global energy budget changes to high latitude North Atlantic cooling and the tropical ITCZ response, *Clim. Dyn.*, *40*(5–6), 1435–1452, doi:10.1007/s00382-012-1482-1.
- Deser, C., A. S. Phillips, R. a. Tomas, Y. M. Okumura, M. a. Alexander, A. Capotondi, J. D.

- Scott, Y.-O. Kwon, and M. Ohba (2012), ENSO and Pacific Decadal Variability in the Community Climate System Model Version 4, *J. Clim.*, 25(8), 2622–2651, doi:10.1175/JCLI-D-11-00301.1.
- Deser, C., R. A. Tomas, L. Sun, C. Deser, R. A. Tomas, and L. Sun (2015), The Role of Ocean–Atmosphere Coupling in the Zonal-Mean Atmospheric Response to Arctic Sea Ice Loss, *J. Clim.*, 28(6), 2168–2186, doi:10.1175/JCLI-D-14-00325.1.
- Dirren, S., and G. J. Hakim (2005), Toward the assimilation of time-averaged observations, *Geophys. Res. Lett.*, 32(4), doi:10.1029/2004GL021444.
- Donohoe, A., J. Marshall, D. Ferreira, and D. Mcgee (2013), The Relationship between ITCZ Location and Cross-Equatorial Atmospheric Heat Transport: From the Seasonal Cycle to the Last Glacial Maximum, *J. Clim.*, 26(11), 3597–3618, doi:10.1175/JCLI-D-12-00467.1.
- Drake, J., I. Foster, J. Michalakes, B. Toonen, and P. Worley (1995), Design and performance of a scalable parallel community climate model, *Parallel Comput.*, 21(10), 1571–1591, doi:10.1016/0167-8191(96)80001-9.
- Evensen, G. (1994), Sequential Data Assimilation with a Nonlinear Quasi-Geostrophic Model Using Monte-Carlo Methods to Forecast Error Statistics, *J. Geophys. Res.*, 99(C5), 10143–10162.
- Fedorov, A. V., S. Hu, M. Lengaigne, and E. Guilyardi (2015), The impact of westerly wind bursts and ocean initial state on the development, and diversity of El Niño events, *Clim. Dyn.*, 44(5–6), 1381–1401, doi:10.1007/s00382-014-2126-4.
- Frierson, D. M. W., and Y.-T. Hwang (2012), Extratropical Influence on ITCZ Shifts in Slab Ocean Simulations of Global Warming, *J. Clim.*, 25(2), 720–733, doi:10.1175/JCLI-D-11-00116.1.

- Frierson, D. M. W., Y.-T. Hwang, N. S. Fučkar, R. Seager, S. M. Kang, A. Donohoe, E. A. Maroon, X. Liu, and D. S. Battisti (2013), Contribution of ocean overturning circulation to tropical rainfall peak in the Northern Hemisphere, *Nat. Geosci.*, 6(11), 940–944, doi:10.1038/ngeo1987.
- Guilyardi, E. (2005), El Niño–mean state–seasonal cycle interactions in a multi-model ensemble, *Clim. Dyn.*, 26(4), 329–348, doi:10.1007/s00382-005-0084-6.
- Hack, J. J., B. A. Boville, B. P. Briegleb, J. T. Kiehl, P. J. Rasch, and D. Williamson (1993), *Description of the NCAR community climate model (CCM2)*, Climate and Global Dynamics Division, NCAR.
- Hakim, G. J., and R. D. Torn (2008), Ensemble Synoptic Analysis, *Meteorol. Monogr.*, 33(55), 147–162, doi:10.1175/0065-9401-33.55.147.
- Hamill, T. M., and J. S. Whitaker (2005), Accounting for the error due to unresolved scales in ensemble data assimilation: A comparison of different approaches, *Mon. Weather Rev.*, 133(11), 3132–3147.
- Hamill, T. M., J. S. Whitaker, and C. Snyder (2001), Distance-dependent filtering of background error covariance estimates in an ensemble Kalman filter, *Mon. Weather Rev.*, 129(11), 2776–2790.
- Han, G. J., X. R. Wu, S. Zhang, Z. Liu, and W. Li (2013), Error Covariance Estimation for Coupled Data Assimilation Using a Lorenz Atmosphere and a Simple Pycnocline Ocean Model, *J. Clim.*, 26(24), 10218–10231, doi:Doi 10.1175/Jcli-D-13-00236.1.
- Hasselmann, K. (1976), Stochastic climate models Part I. Theory, *Tellus*, 28(6), 473–485, doi:10.1111/j.2153-3490.1976.tb00696.x.
- Hawcroft, M., J. M. Haywood, M. Collins, A. Jones, A. C. Jones, and G. Stephens (2016), Southern Ocean albedo, inter-hemispheric energy transports and the double ITCZ:

- global impacts of biases in a coupled model, *Clim. Dyn.*, 1–17, doi:10.1007/s00382-016-3205-5.
- Houtekamer, P. L., and H. L. Mitchell (1998), Data assimilation using an ensemble Kalman filter technique, *Mon. Weather Rev.*, 126(3), 796–811.
- Hu, S., A. V. Fedorov, M. Lengaigne, and E. Guilyardi (2014), The impact of westerly wind bursts on the diversity and predictability of El Niño events: An ocean energetics perspective, *Geophys. Res. Lett.*, 41(13), 4654–4663, doi:10.1002/2014GL059573.
- Huang, B., V. F. Banzon, E. Freeman, J. Lawrimore, W. Liu, T. C. Peterson, T. M. Smith, P. W. Thorne, S. D. Woodruff, and H. M. Zhang (2015), Extended reconstructed sea surface temperature version 4 (ERSST.v4). Part I: Upgrades and intercomparisons, *J. Clim.*, 28(3), 911–930, doi:10.1175/JCLI-D-14-00006.1.
- Huang, B., P. W. Thorne, T. M. Smith, W. Liu, J. Lawrimore, V. F. Banzon, H.-M. Zhang, T. C. Peterson, and M. Menne (2016), Further Exploring and Quantifying Uncertainties for Extended Reconstructed Sea Surface Temperature (ERSST) Version 4 (v4), *J. Clim.*, 29(9), 3119–3142, doi:10.1175/JCLI-D-15-0430.1.
- Huntley, H. S., and G. J. Hakim (2010), Assimilation of time-averaged observations in a quasi-geostrophic atmospheric jet model, *Clim. Dyn.*, 35(6), 995–1009, doi:10.1007/s00382-009-0714-5.
- Hwang, Y.-T., and D. M. W. Frierson (2013), Link between the double-Intertropical Convergence Zone problem and cloud biases over the Southern Ocean, *Proc. Natl. Acad. Sci. U. S. A.*, 110(13), 4935–4940, doi:Doi 10.1073/Pnas.1213302110.
- Jacob, R. (1997), Low Frequency Variability in a Simulated Atmosphere Ocean System, University of Wisconsin-Madison.
- Jin, F. F. (1997), An equatorial ocean recharge paradigm for ENSO. Part 1: Conceptual

- model, *J. Atmos. Sci.*, 54(7), 811–829, doi:Doi 10.1175/1520-0469(1997)054<0811:Aeorpf>2.0.Co;2.
- Kalnay, E. et al. (1996), The NCEP/NCAR 40-year reanalysis project, *Bull. Am. Meteorol. Soc.*, 77(3), 437–471.
- Kalnay, E., Y. Ota, T. Miyoshi, and J. Liu (2012), A simpler formulation of forecast sensitivity to observations: application to ensemble Kalman filters, *Tellus A*, 64, doi:10.3402/tellusa.v64i0.18462.
- Kang, S. M., I. M. Held, D. M. W. Frierson, and M. Zhao (2008), The Response of the ITCZ to Extratropical Thermal Forcing: Idealized Slab-Ocean Experiments with a GCM, *J. Clim.*, 21(14), 3521–3532, doi:10.1175/2007JCLI2146.1.
- Kang, S. M., D. M. W. Frierson, and I. M. Held (2009), The Tropical Response to Extratropical Thermal Forcing in an Idealized GCM: The Importance of Radiative Feedbacks and Convective Parameterization, *J. Atmos. Sci.*, 66(9), 2812–2827, doi:10.1175/2009JAS2924.1.
- Kao, H.-Y., and J.-Y. Yu (2009), Contrasting Eastern-Pacific and Central-Pacific Types of ENSO, *J. Clim.*, 22(3), 615–632, doi:10.1175/2008JCLI2309.1.
- Karspeck, A. R., S. Yeager, G. Danabasoglu, T. Hoar, N. Collins, K. Raeder, J. L. Anderson, and J. Tribbia (2013), An Ensemble Adjustment Kalman Filter for the CCSM4 Ocean Component, *J. Clim.*, 26(19), 7392–7413, doi:Doi 10.1175/Jcli-D-12-00402.1.
- Kay, J. E., C. Wall, V. Yettella, B. Medeiros, C. Hannay, P. Caldwell, and C. M. Bitz (2016), Global Climate Impacts of Fixing the Southern Ocean Shortwave Radiation Bias in the Community Earth System Model (CESM), *J. Clim.*, 29(12), 4617–4636, doi:10.1175/JCLI-D-15-0358.1.
- Kirtman, B. P. (1997), Oceanic Rossby Wave Dynamics and the ENSO Period in a Coupled

- Model, *J. Clim.*, *10*(7), 1690–1704, doi:10.1175/1520-0442(1997)010<1690:ORWDAT>2.0.CO;2.
- Kirtman, B. P., and J. Shukla (2002), Interactive coupled ensemble: A new coupling strategy for CGCMs, *Geophys. Res. Lett.*, *29*(10), 5-1-5-4, doi:10.1029/2002GL014834.
- Klein, S. A., and D. L. Hartmann (1993), The seasonal cycle of low stratiform clouds, *J. Clim.*, *6*(8), 1587–1606, doi:10.1175/1520-0442(1993)006<1587:TSCOLS>2.0.CO;2.
- Kunii, M., T. Miyoshi, and E. Kalnay (2012), Estimating the Impact of Real Observations in Regional Numerical Weather Prediction Using an Ensemble Kalman Filter, *Mon. Weather Rev.*, *140*(6), 1975–1987, doi:Doi 10.1175/Mwr-D-11-00205.1.
- Kushnir, Y., W. a. Robinson, I. Bladé, N. M. J. Hall, S. Peng, and R. Sutton (2002), Atmospheric GCM response to extratropical SST anomalies: Synthesis and evaluation, *J. Clim.*, *15*, 2233–2256, doi:10.1175/1520-0442(2002)015<2233:AGRTEs>2.0.CO;2.
- Larson, S. M., and B. P. Kirtman (2013), The Pacific Meridional Mode as a trigger for ENSO in a high-resolution coupled model, *Geophys. Res. Lett.*, *40*(12), 3189–3194, doi:10.1002/grl.50571.
- Larson, S. M., and B. P. Kirtman (2014), The Pacific Meridional Mode as an ENSO Precursor and Predictor in the North American Multimodel Ensemble, *J. Clim.*, *27*(18), 7018–7032, doi:10.1175/JCLI-D-14-00055.1.
- Larson, S. M., and B. P. Kirtman (2015), Revisiting ENSO Coupled Instability Theory and SST Error Growth in a Fully Coupled Model, *J. Clim.*, *28*(12), 4724–4742, doi:10.1175/JCLI-D-14-00731.1.
- Lewis, M., M. Carr, G. Feldman, W. Esaias, and C. McClain (1990), Influence of

- penetrating solar radiation on the heat budget of the equatorial Pacific Ocean, *Nature*, *347*, 543–545.
- Li, G., and S.-P. Xie (2014), Tropical Biases in CMIP5 Multimodel Ensemble: The Excessive Equatorial Pacific Cold Tongue and Double ITCZ Problems*, *J. Clim.*, *27*, 1765–1780.
- Liu, H., F. Lu, Z. Liu, Y. Liu, and S. Zhang (2016), Assimilating atmosphere reanalysis in coupled data assimilation, *J. Meteorol. Res.*, *30*(4), 572–583, doi:10.1007/s13351-016-6014-1.
- Liu, J., and E. Kalnay (2008), Estimating observation impact without adjoint model in an ensemble Kalman filter, *Q. J. R. Meteorol. Soc.*, *134*(634), 1327–1335, doi:10.1002/qj.280.
- Liu, W., B. Huang, P. W. Thorne, V. F. Banzon, H.-M. Zhang, E. Freeman, J. Lawrimore, T. C. Peterson, T. M. Smith, and S. D. Woodruff (2015), Extended Reconstructed Sea Surface Temperature Version 4 (ERSST.v4): Part II. Parametric and Structural Uncertainty Estimations, *J. Clim.*, *28*(3), 931–951, doi:10.1175/JCLI-D-14-00007.1.
- Liu, Y., Z. Liu, S. Zhang, X. Rong, R. Jacob, S. Wu, and F. Lu (2014a), Ensemble-based parameter estimation in a coupled GCM using the adaptive spatial average method, *J. Clim.*, *27*(11), 4002–4014, doi:10.1175/JCLI-D-13-00091.1.
- Liu, Y., Z. Liu, S. Zhang, R. Jacob, F. Lu, X. Rong, and S. Wu (2014b), Ensemble-Based Parameter Estimation in a Coupled General Circulation Model, *J. Clim.*, *27*(18), 7151–7162, doi:10.1175/JCLI-D-13-00406.1.
- Liu, Z. (1996), Modeling Equatorial Annual Cycle with a Linear Coupled Model, *J. Clim.*, *9*(10), 2376–2385, doi:10.1175/1520-0442(1996)009<2376:MEACWA>2.0.CO;2.
- Liu, Z., and M. Alexander (2007), Atmospheric bridge, oceanic tunnel, and global climatic

- teleconnections, *Rev. Geophys.*, 45(2), RG2005, doi:10.1029/2005RG000172.
- Liu, Z., and S.-P. Xie (1994), Equatorward Propagation of Coupled Air–Sea Disturbances with Application to the Annual Cycle of the Eastern Tropical Pacific, *J. Atmos. Sci.*, 51(24), 3807–3822, doi:10.1175/1520-0469(1994)051<3807:EPOCAD>2.0.CO;2.
- Liu, Z., and H. Yang (2003), Extratropical control of tropical climate, the atmospheric bridge and oceanic tunnel, *Geophys. Res. Lett.*, 30(5), 1230, doi:10.1029/2002GLO16492.
- Liu, Z., S. G. H. Philander, and R. C. Pacanowski (1994), A GCM Study of Tropical–Subtropical Upper-Ocean Water Exchange, *J. Phys. Oceanogr.*, 24(12), 2606–2623, doi:10.1175/1520-0485(1994)024<2606:AGSOTU>2.0.CO;2.
- Liu, Z., J. Kutzbach, and L. X. Wu (2000), Modeling climate shift of El Nino variability in the Holocene, *Geophys. Res. Lett.*, 27(15), 2265–2268, doi:10.1029/2000gl011452.
- Liu, Z., Q. Zhang, and L. Wu (2004), Remote Impact on Tropical Atlantic Climate Variability: Statistical Assessment and Dynamic Assessment*, *J. Clim.*, 17(7), 1529–1549, doi:10.1175/1520-0442(2004)017<1529:RIOTAC>2.0.CO;2.
- Liu, Z., Y. Liu, L. Wu, and R. Jacob (2007a), Seasonal and Long-Term Atmospheric Responses to Reemerging North Pacific Ocean Variability: A Combined Dynamical and Statistical Assessment*, *J. Clim.*, 20(6), 955, doi:10.1175/JCLI4041.1.
- Liu, Z. et al. (2007b), Simulating the transient evolution and abrupt change of Northern Africa atmosphere–ocean–terrestrial ecosystem in the Holocene, *Quat. Sci. Rev.*, 26(13–14), 1818–1837, doi:10.1016/j.quascirev.2007.03.002.
- Liu, Z., S. Wu, S. Zhang, Y. Liu, and X. Y. Rong (2013), Ensemble data assimilation in a simple coupled climate model: The role of ocean-atmosphere interaction, *Adv.*

- Atmos. Sci.*, 30(5), 1235–1248, doi:Doi 10.1007/S00376-013-2268-Z.
- Liu, Z., Z. Lu, X. Wen, B. L. Otto-Bliesner, A. Timmermann, and K. M. Cobb (2014c), Evolution and forcing mechanisms of El Niño over the past 21,000 years, *Nature*, 515(7528), 550–553, doi:10.1038/nature13963.
- Lu, F., and Z. Liu (2017), Assessing Extratropical Atmospheric Influence on Historical El Niño Events Using Regional Coupled Data Assimilation, *submitted*.
- Lu, F., Z. Liu, S. Zhang, and Y. Liu (2015a), Strongly Coupled Data Assimilation Using Leading Averaged Coupled Covariance (LACC). Part I: Simple Model Study*, *Mon. Weather Rev.*, 143(9), 3823–3837, doi:10.1175/MWR-D-14-00322.1.
- Lu, F., Z. Liu, S. Zhang, Y. Liu, and R. Jacob (2015b), Strongly Coupled Data Assimilation Using Leading Averaged Coupled Covariance (LACC). Part II: CGCM Experiments*, *Mon. Weather Rev.*, 143(11), 4645–4659, doi:10.1175/MWR-D-15-0088.1.
- Lu, F., Z. Liu, S. Zhang, and R. Jacob (2017a), Assessing extratropical impact on the tropical bias in coupled climate model with regional coupled data assimilation, *Geophys. Res. Lett.*, 44(7), 3384–3392, doi:10.1002/2017GL072890.
- Lu, F., Z. Liu, Y. Liu, S. Zhang, and R. Jacob (2017b), Understanding the control of extratropical atmospheric variability on ENSO using a coupled data assimilation approach, *Clim. Dyn.*, 48(9–10), 3139–3160, doi:10.1007/s00382-016-3256-7.
- Maroon, E. A., D. M. W. Frierson, and D. S. Battisti (2015), The Tropical Precipitation Response to Andes Topography and Ocean Heat Fluxes in an Aquaplanet Model, *J. Clim.*, 28(1), 381–398, doi:10.1175/JCLI-D-14-00188.1.
- Matei, D., N. Keenlyside, M. Latif, and J. Jungclaus (2008), Subtropical Forcing of Tropical Pacific Climate and Decadal ENSO Modulation, *J. Clim.*, 21(18), 4691–4709, doi:10.1175/2008JCLI2075.1.

- McPhaden, M. J. (1999), Genesis and Evolution of the 1997-98 El Niño, *Science* (80-.), 283(5404), 950–954, doi:10.1126/science.283.5404.950.
- Mechoso, C. R., T. Losada, S. Koseki, E. Mohino-Harris, N. Keenlyside, A. Castaño-Tierno, T. A. Myers, B. Rodriguez-Fonseca, and T. Toniazzo (2016), Can reducing the incoming energy flux over the Southern Ocean in a CGCM improve its simulation of tropical climate?, *Geophys. Res. Lett.*, 43(20), 11,057-11,063, doi:10.1002/2016GL071150.
- Mitchell, T. P., and J. M. Wallace (1992), The Annual Cycle in Equatorial Convection and Sea Surface Temperature, *J. Clim.*, 5(10), 1140–1156, doi:10.1175/1520-0442(1992)005<1140:TACIEC>2.0.CO;2.
- Murtugudde, R., J. Beauchamp, C. R. McClain, M. Lewis, and A. J. Busalacchi (2002), Effects of Penetrative Radiation on the Upper Tropical Ocean Circulation, *J. Clim.*, 15(5), 470–486, doi:10.1175/1520-0442(2002)015<0470:EOPROT>2.0.CO;2.
- Neelin, J. D., D. S. Battisti, A. C. Hirst, F.-F. Jin, Y. Wakata, T. Yamagata, and S. E. Zebiak (1998), ENSO theory, *J. Geophys. Res.*, 103(C7), 14261, doi:10.1029/97JC03424.
- Newman, M., M. a. Alexander, and J. D. Scott (2011), An empirical model of tropical ocean dynamics, *Clim. Dyn.*, 37(9–10), 1823–1841, doi:10.1007/s00382-011-1034-0.
- Oueslati, B., and G. Bellon (2015), The double ITCZ bias in CMIP5 models: interaction between SST, large-scale circulation and precipitation, *Clim. Dyn.*, 44(3–4), 585–607, doi:10.1007/s00382-015-2468-6.
- Philander, S. G. (1990), *El Niño, La Niña, and the Southern Oscillation*, International Geophysics, Elsevier.
- Philander, S. G., D. Gu, D. Halpern, G. Lambert, N. C. Lau, T. Li, and R. C. Pacanowski (1996), Why the ITCZ is mostly north of the equator, *J. Clim.*, 9(12), 2958–2972,

doi:Doi 10.1175/1520-0442(1996)009<2958:Wtiimn>2.0.Co;2.

Pierce, D. W., T. P. Barnett, and M. Latif (2000), Connections between the Pacific Ocean Tropics and Midlatitudes on Decadal Timescales, *J. Clim.*, *13*(6), 1173–1194,

doi:10.1175/1520-0442(2000)013<1173:CBTPOT>2.0.CO;2.

Raeder, K., J. L. Anderson, N. Collins, T. J. Hoar, J. E. Kay, P. H. Lauritzen, and R. Pincus (2012), DART/CAM: An Ensemble Data Assimilation System for CESM Atmospheric Models, *J. Clim.*, *25*(18), 6304–6317, doi:Doi 10.1175/Jcli-D-11-00395.1.

Saha, S. et al. (2010), The NCEP Climate Forecast System Reanalysis, *Bull. Am. Meteorol. Soc.*, *91*(8), 1015–1057, doi:10.1175/2010BAMS3001.1.

Schneider, E. K., and Z. Zhu (1998), Sensitivity of the Simulated Annual Cycle of Sea Surface Temperature in the Equatorial Pacific to Sunlight Penetration, *J. Clim.*, *11*(8), 1932–1950, doi:10.1175/1520-0442(1998)011<1932:SOTSAC>2.0.CO;2.

Schneider, T., T. Bischoff, and G. H. Haug (2014), Migrations and dynamics of the intertropical convergence zone, *Nature*, *513*(7516), 45–53, doi:10.1038/nature13636.

Schott, F. a, J. P. McCreary, and G. C. Johnson (2004), Shallow Overturning Circulations of the Tropical- Subtropical Oceans, in *Earth's Climate*, pp. 261–304.

Sugiura, N., T. Awaji, S. Masuda, T. Mochizuki, T. Toyoda, T. Miyama, H. Igarashi, and Y. Ishikawa (2008), Development of a four-dimensional variational coupled data assimilation system for enhanced analysis and prediction of seasonal to interannual climate variations, *J. Geophys. Res.*, *113*(C10), C10017, doi:10.1029/2008JC004741.

Takahashi, K., and D. S. Battisti (2007), Processes controlling the mean tropical pacific precipitation pattern. Part I: The Andes and the eastern Pacific ITCZ, *J. Clim.*, *20*(14), 3434–3451, doi:10.1175/JCLI4198.1.

Tardif, R., G. J. Hakim, and C. Snyder (2014a), Coupled atmosphere–ocean data

- assimilation experiments with a low-order climate model, *Clim. Dyn.*, 43(5–6), 1631–1643, doi:10.1007/s00382-013-1989-0.
- Tardif, R., G. J. Hakim, and C. Snyder (2014b), Coupled atmosphere–ocean data assimilation experiments with a low-order model and CMIP5 model data, *Clim. Dyn.*, doi:10.1007/s00382-014-2390-3.
- Torn, R. D., and G. J. Hakim (2008), Ensemble-Based Sensitivity Analysis, *Mon. Weather Rev.*, 136(2), 663–677, doi:10.1175/2007MWR2132.1.
- Vecchi, G. A., D. E. Harrison, G. A. Vecchi, and D. E. Harrison (2000), Tropical Pacific Sea Surface Temperature Anomalies, El Niño, and Equatorial Westerly Wind Events*, *J. Clim.*, 13(11), 1814–1830, doi:10.1175/1520-0442(2000)013<1814:TPSSTA>2.0.CO;2.
- Vimont, D. J. (2010), Transient growth of thermodynamically coupled variations in the tropics under an equatorially symmetric mean state, *J. Clim.*, 23(21), 5771–5789, doi:10.1175/2010JCLI3532.1.
- Vimont, D. J., D. S. Battisti, and A. C. Hirst (2001), Footprinting: A seasonal connection between the tropics and mid-latitudes, *Geophys. Res. Lett.*, 28(20), 3923–3926, doi:10.1029/2001GL013435.
- Vimont, D. J., D. S. Battisti, and A. C. Hirst (2003a), The Seasonal Footprinting Mechanism in the CSIRO General Circulation Models*, *J. Clim.*, 16(16), 2653–2667, doi:10.1175/1520-0442(2003)016<2653:TFSMIT>2.0.CO;2.
- Vimont, D. J., J. M. Wallace, and D. S. Battisti (2003b), The Seasonal Footprinting Mechanism in the Pacific: Implications for ENSO*, *J. Clim.*, 16(16), 2668–2675, doi:10.1175/1520-0442(2003)016<2668:TFSMIT>2.0.CO;2.
- Vimont, D. J., M. a. Alexander, and A. Fontaine (2009), Midlatitude Excitation of Tropical

- Variability in the Pacific: The Role of Thermodynamic Coupling and Seasonality*, *J. Clim.*, 22(3), 518–534, doi:10.1175/2008JCLI2220.1.
- Vimont, D. J., M. a. Alexander, and M. Newman (2014), Optimal growth of Central and East Pacific ENSO events, *Geophys. Res. Lett.*, 41(11), 4027–4034, doi:10.1002/2014GL059997.
- Waliser, D. E., and N. E. Graham (1993), Convective cloud systems and warm-pool sea surface temperatures: Coupled interactions and self-regulation, *J. Geophys. Res. Atmos.*, 98(D7), 12881–12893, doi:10.1029/93JD00872.
- Wu, L., and Z. Liu (2005), North Atlantic Decadal Variability: Air–Sea Coupling, Oceanic Memory, and Potential Northern Hemisphere Resonance*, *J. Clim.*, 18(2), 331–349, doi:10.1175/JCLI-3264.1.
- Wu, L., Z. Liu, R. G. Gallimore, R. Jacob, D. Lee, and Y. Zhong (2003), Pacific decadal variability: The tropical Pacific mode and the North Pacific mode, *J. Clim.*, 16(8), 1101–1120, doi:Doi 10.1175/1520-0442(2003)16<1101:Pdvttp>2.0.Co;2.
- Xie, P. P., and P. A. Arkin (1997), Global precipitation: A 17-year monthly analysis based on gauge observations, satellite estimates, and numerical model outputs, *Bull. Am. Meteorol. Soc.*, 78(11), 2539–2558.
- Xie, S.-P. (2004), The Shape of Continents, Air-Sea Interaction, and the Rising Branch of the Hadley Circulation, in *The Hadley Circulation: Present, Past and Future*, pp. 121–152.
- Xie, S.-P., and S. G. Philander (1994), A Coupled Ocean-Atmosphere Model of Relevance to the ITCZ in the Eastern Pacific, *Tellus Ser. a-Dynamic Meteorol. Oceanogr.*, 46(4), 340–350, doi:Doi 10.1034/J.1600-0870.1994.T01-1-00001.X.
- Yang, H., and Z. Liu (2005), Tropical–extratropical climate interaction as revealed in

- idealized coupled climate model experiments, *Clim. Dyn.*, 24(7–8), 863–879, doi:10.1007/s00382-005-0021-8.
- Yeh, S.-W., X. Wang, C. Wang, and B. Dewitte (2015), On the Relationship between the North Pacific Climate Variability and the Central Pacific El Niño, *J. Clim.*, 28(2), 663–677, doi:10.1175/JCLI-D-14-00137.1.
- Yu, J.-Y., and H.-Y. Kao (2007), Decadal changes of ENSO persistence barrier in SST and ocean heat content indices: 1958–2001, *J. Geophys. Res. Atmos.*, 112(D13), n/a–n/a, doi:10.1029/2006JD007654.
- Yu, J.-Y., H.-Y. Kao, and T. Lee (2010), Subtropics-Related Interannual Sea Surface Temperature Variability in the Central Equatorial Pacific, *J. Clim.*, 23(11), 2869–2884, doi:10.1175/2010JCLI3171.1.
- Zhang, F., C. Snyder, and J. Z. Sun (2004), Impacts of initial estimate and observation availability on convective-scale data assimilation with an ensemble Kalman filter, *Mon. Weather Rev.*, 132(5), 1238–1253.
- Zhang, H., A. Clement, and P. Di Nezio (2014), The South Pacific Meridional Mode: A Mechanism for ENSO-like Variability, *J. Clim.*, 27(2), 769–783, doi:10.1175/JCLI-D-13-00082.1.
- Zhang, L., P. Chang, and L. Ji (2009), Linking the Pacific Meridional Mode to ENSO: Coupled Model Analysis, *J. Clim.*, 22(12), 3488–3505, doi:10.1175/2008JCLI2473.1.
- Zhang, S., M. J. Harrison, A. Rosati, and A. T. Wittenberg (2007), System design and evaluation of coupled ensemble data assimilation for global oceanic climate studies, *Mon. Weather Rev.*, 135(10), 3541–3564, doi:10.1175/MWR3466.1.